Impacts of Dissolved Iron and Dynamic Operation on Nickel-Based Anode Catalysts in Alkaline Water Electrolysis Cells

by

Manasa Rajeev

A dissertation accepted and approved in partial fulfillment of the
requirements for the degree of
Doctor of Philosophy
in Chemistry

Dissertation Committee:

Dr. Paul A. Kempler, Advisor

Dr. Carl Brozek, Chair

Dr. Shannon W. Boettcher, Core Member

Dr. George Nazin, Core Member

Dr. Matthew Polizzotto, Institutional Representative

University of Oregon

Summer 2026

© 2026 Manasa Rajeev

DISSERTATION ABSTRACT

Manasa Rajeev

Doctor of Philosophy in Chemistry

Title: Impacts of Dissolved Iron and Dynamic Operation on Nickel-Based Anode Catalysts in Alkaline Water Electrolysis Cells

Alkaline water electrolysis (AWE) is a robust method for generating hydrogen. Dissolved iron (Fe) species are a pre-requisite for the most active catalyst sites for the oxygen evolution reaction in alkaline electrolytes, but the overall effects of dissolved Fe on energy-efficient advanced alkaline water electrolysis cells remain unclear. Here, we systematically control the concentration of Fe in a model zero-gap alkaline water electrolyzer to understand the interactions between Fe and high surface area catalyst coatings. Cells employing a platinum-group-metal-containing cathode and a high surface area, mixed-metal-oxide anode yielded an optimum voltage efficiency at elevated temperatures and in the presence of 6 ppm Fe, which reduced the cell voltage by ~100 mV compared to rigorously Fe-free electrolytes. Increasing concentrations of Fe led to a systematic increase in anode activity towards the oxygen evolution reaction and a reduction in the electrochemically active surface area at both the anode and cathode. Metallic Fe was not observed to electrodeposit at cathodes which operate at overpotentials >– 120 mV, but dissolved Fe does reduce the apparent number density of sites available for hydride adsorption. These findings suggest that the energy efficiency of advanced alkaline water electrolysis systems can be improved by managing the Fe concentration in recirculating KOH electrolytes.

The stability and efficiency of AWE anodes are impacted by reverse polarization conditions that occur during shutdown or power interruptions. Here we report the effect of reverse polarization on model thin-film Ni(Fe)OOH anodes in conditions that mirror those seen in commercial AWE stacks. Regardless of the extent of the reverse polarization potential, the anodic charge capacity decreases over successive cycles, indicating loss of active Ni^{2+}/Ni^{3+} sites with cycling. Electrodes held for a longer period in the reduced state exhibited an accelerated catalyst loss through dissolution and structural reorganization during reverse polarization. Electrolytes spiked with soluble Fe preserved activity throughout repeated reverse current events, whereas suspended $Ni(OH)_2$ preserved Ni^{2+}/Ni^{3+} sites that exhibited lower activity for the OER. In-situ Raman spectroscopy and post-polarization X-ray photoelectron spectroscopy revealed a significant decrease in the Fe:Ni surface ratio after reverse polarization, which correlates with the loss of active Fe–Ni oxyhydroxide domains and a measurable decline in oxygen evolution reaction (OER) activity. These findings on model thin-film anodes thus illustrate both the mode of typical anode degradation during shutdown/reverse-polarization conditions and how they can be mitigated by managing the dissolved ions in the recirculating KOH.

Stainless steel components were aged both thermally and electrochemically in KOH to produce electrolytes with different extents of corrosion. A thin-film $Ni_xFe_{(1-x)}OOH$ catalyst coated on Pt foil was then subjected to repeated charge–discharge cycling in these electrolytes. The aged electrolytes produced distinct cell-voltage and discharge-capacity responses, demonstrating that catalyst behavior depended on both electrolyte-aging duration and the evolving mixture of dissolved metal species. Detailed analysis of the electrolyte aged during 3 h of OER operation showed that corrosion-derived impurities

altered the Ni^{2+}/Ni^{3+} redox response, consistent with changes in the local electronic environment and Fe incorporation. Surface analysis further showed that Fe, Cr, and Mn incorporated into the anode during operation but were only partially retained following repeated charge–discharge cycling.

This dissertation includes previously published, unpublished, and co-authored material.

ACKNOWLEDGEMENTS

This work was supported by Southern California Gas Company Award #CW63431, NSF Chemical Catalysis program award #2400195, and by Hgen Inc. I want to express my sincere gratitude to the Department of Chemistry and Biochemistry and the University of Oregon for the opportunity to be part of this wonderful program.

I am deeply grateful to Paul Kempler and Shannon Boettcher for their mentorship and guidance. Their scientific knowledge and thoughtful feedback have played a critical role in shaping who I am today. Thank you for your continuous encouragement, constructive feedback, and immense patience throughout this journey. I am also grateful to my present and past graduate committee members, Prof. Carl Brozek, Prof. George Nazin, Prof. Matthew Polizzotto, and Prof. Erin Moore, for their support throughout major milestones of my graduate career.

I acknowledge the support from the Center for Advanced Materials Characterization in Oregon (CAMCOR) for letting me use the shared instruments. I am grateful to Dr. Stephen Golledge, Valerie Brogden, and Phuc Pham for their assistance with data collection and interpretation. This work would not have been possible without the help of Julian McAdams for assistance with the zero-gap cell fabrication.

I want to extend my gratitude to our industrial collaborators, especially Dr. Grace Lindquist, Dr. Ethan Simonoff, Molly Yang, and Collin Ho, for trusting me with the project and for all the insightful electrochemical discussions.

I want to thank all the current and past Kempler and Boettcher lab members for making this journey memorable. Thanks to my dearest friend Dr. Anthony Ekennia for always being the greatest support ever. Thanks to Dr. Meikun Shen, Dr. Fernanda Brito, Dr. Evandi Rahman, Dr. Kasinath Ojha, Dr. Prasad Sharma, Michaela Vacca, Louka Moutarlier, Raj Shekar, Ben Andrews, Yiwen Sun, Nicole Sagui, Olivia Treankle, Lihaokun Chen, Yang Zhao, Minkyoung Kwak, Nick D'Antona, Kira Thurman, Evan Stern, and Andrew Goldman for making these five years beautiful and memorable. I want to express my gratitude to all the wonderful mentees who supported my research, especially Favour Foday, Arya Jerome-Saboori, Christian Emeodi, Joseph Daddona, and Jamin Cato.

I am beyond grateful to my dad, mom, sister, Awwlee, and all my other dear family members and friends for their unwavering love, support, and for always keeping me in their prayers. Lastly, I want to thank my amazing life partner, Karthik, for his unconditional love and comfort, for making even the most difficult days feel lighter, and for always making me feel at home.

TABLE OF CONTENTS

Chapter I 16

Impact of dissolved Iron on Alkaline Water Electrolysis Cells 16
Introduction 16

Results 19

Discussion 30

Influence of Fe on the polarization response of electrolysis cells 30

Influence of dissolved Fe on anode catalyst coatings 31

Influence of dissolved Fe on cathode catalyst coatings 34

Implications for the design of advanced alkaline water electrolysis cells 35

Materials and methods 36

Materials 36

Electrode preparation 37

Two-electrode measurements 37

Three-electrode measurements 38

Material Characterization: 38

In-situ Raman measurements: 38

Chapter II 40

Thin-Film $Ni_xFe_{(1-X)}OOH$ Anode Catalyst Degradation in Alkaline Water Electrolyzers During Reverse Current Conditions 40
Introduction 40

Results 43

Discussion 55

Residence time in the reduced state 55

Reconstruction of $Ni_xFe_{(1-x)}OOH$ catalysts 56

Implications for zero-gap alkaline electrolyzers 59
Materials and methods 64
Materials 64
Preparation of thin-film nickel-iron oxyhydroxide (NixFe(1-x)OOH) and nickel oxyhydroxide (NiOOH) electrodes 64
Charge-discharge analysis 65
Studies on electrolyte composition 65
In-situ Raman spectroscopy 66
X-ray photoelectron spectroscopy (XPS) 66

CHAPTER III 68

Effect of Reverse Polarization on Thin-Film NiFe $_{(1-X)}$OOH in Realistic AWE Electrolytes Containing Dissolved Metals 68
Introduction 68
Results 71
Discussion 78
Effect of dissolved metal impurities 79
Materials and methods: 80
Materials 80
Aging of potassium hydroxide at elevated temperatures 80
Electrochemical aging of KOH 81
Charge-discharge analysis 81
UV-Vis spectroscopy 81
X-ray photoelectron spectroscopy (XPS) 81

APPENDIX I 83
Chapter I: Supporting Information 83
Charge integration: 83
Chapter I: Supporting Figures 85

APPENDIX II 95
Chapter II Supplemental Information 95
Zero-gap cell assembly: 95

Raman analysis of catalyst reconstruction: 95
Chapter II Supporting Figures 100

APPENDIX III 111
Chapter III: Supplemental Information 111
Chapter III: Supporting Figures 112

References 116

LIST OF FIGURES

1.1 Cell assembly and electrode characterization 20

1.2 Total cell voltage as a function of [Fe] 21

1.3 NiCo-PGM electrode durability test 22

1.4 CV comparison of Ni, NiCo and NiO electrodes as a function of [Fe] 23

1.5 XPS and Raman analysis of NiCo electrodes 25

1.6 PGM-cathode potential as a function of [Fe] 27

1.7 CV analysis of PGM-cathode as a function of [Fe] 28

2.1 Characteristic discharge curve of $Ni_xFe_{(1-x)}OOH$ catalyst 43

2.2 Discharge profile of $Ni_xFe_{(1-x)}OOH$ films as a function of E_- and J_- 44

2.3 Discharge profile of $Ni_xFe_{(1-x)}OOH$ films as a function of [Fe] 46

2.4 XPS data for $Ni_xFe_{(1-x)}(OH)_2$, $Ni_xFe_{(1-x)}OOH$, and reoxidized $Ni_xFe_{(1-x)}(OH)_2$ electrodes 49

2.5 Discharge profile of $Ni_xFe_{(1-x)}OOH$ films in Fe-spiked KOH, $Ni(NO_3)_2$-spiked KOH, and $Ni(OH)_2$-spiked KOH in three electrode cell. 50

2.6 Discharge profile of $Ni_xFe_{(1-x)}OOH$ films in Fe-spiked KOH, $Ni(NO_3)_2$-spiked KOH, and $Ni(OH)_2$-spiked KOH in zero-gap cell 53

2.7 Processes affecting anode catalyst stability during repeated charge/discharge cycles. 63

3.1 Change in total cell voltage as a function of electrolyte aging 71

3.2 Comparing the changes in E_{cell}, E_{anode} and $E_{cathode}$ as a function of electrolyte aging .. 73

3.3 Quantification of dissolved Fe in the electrolyte via UV-Vis spectroscopy 75

3.4 Effect of dissolved iron on the OER activity of thin-film $Ni_xFe_{(1-x)}OOH$ as a function of Fe precursor complex. 77

A. 1 XPS analysis of uncoated Ni mesh 85

A. 2 Diagram of the model zero-gap cell 85

A. 3 Diagram of the in situ Raman cell 86

A. 4 SEM-EDX spectra of NiCo anode 87

A. 5 Powder XRD pattern of NiCo electrode annealed at different temperatures.....87

A. 6 Cyclic voltammetry of NiCo anode and PGM cathode in the presence of Cl^- addition 88

A. 7 ICP-MS analysis of anolyte Fe concentration.....89

A. 8 $E_{cell\ vs}$ time behavior for PGM-NiCo AAWE cell at $J = 250$ mA cm^{-2} in 30% w/w KOH at 80 °C. [Fe] = 6 ppm was added to the cell at $t = 0.25$ h. 89

A. 9 Tafel plot of NiCo in KOH containing different amounts of dissolved Fe 90

A. 10 Tafel plot of Ni in KOH containing different amounts of dissolved Fe.....90

A. 11 Tafel plot of NiO in KOH containing different amounts of dissolved Fe. 91

A. 12 High-resolution XPS of NiCo electrode after 24 h test at 250 mA cm^{-2} in KOH containing different amounts of dissolved Fe 92

A. 13 In situ Raman spectra of NiCo electrode in 30% w/w KOH at 60 °C recorded at 0.93 V**,** 1.23 V. 93

A. 14Cyclic voltammetry for a PGM cathode cycled from $0.05 < E < 0.5$ V vs. RHE at 100 mV s^{-1} in 30% w/w KOH at 80 °C 94

A. 15 Comparison of ex situ Raman spectra of NiCo anodes before and after testing in KOH containing Fe 94

B. 1 Voltammetry of anodes with and without catalyst coating.....100

B. 2 XRD of Ni(OH)2. Ni(OH)2 was synthesized by precipitating 3.0 M Ni(NO3)2·6H2O in 1.0 M KOH.....100

B. 3 Image of zero-gap electrolysis cell.....101

B. 4 Image of Ni(OH)2 spiked 30% w/w KOH at 80 °C. A pale green precipitate was assigned to Ni(OH)2 101

B. 5 Charge integration comparison between from CV method and glavanostatic discharge method 102

B. 6 Charge integration from cyclic voltammetry as a function of Fe content.....103

B. 7 Normalized activity of thin-film catalysts as a function of Fe content within the electrolyte.....104

B. 8 Raman spectra of NiOOH as a function of dissolved Fe content.....105

B. 9 Ex-situ Raman spectra of NixFe(1-x)OOH as a function of final resting potential in Fe-containing electrolyte. 106

B. 10 Ex-situ Raman spectra of NixFe(1-x)OOH as a function of final resting potential in Fe-free electrolyte 106

B. 11 Cycle-dependent OER activity in KOH spiked with Fe3+ or Ni(OH)2.....107

B. 12 Influence of cycling on the voltammetry of thin-film catalysts in KOH spiked with dissolved Fe or solid Ni(OH)2. 108

B. 13 Influence of cycling on the voltammetry of thin-film catalysts in KOH spiked with dissolved Fe or a mixture of dissolved Fe and Ni.....108

B. 14 Impact of cycle number on discharge capacity in electrolyte with and without spiked Fe. 109

B. 15 Influence of cycling on the voltammetry of mesh-supported catalysts in KOH spiked with dissolved Fe, a mixture of dissolved Fe and Ni, or solid Ni(OH)2. 110

B. 16 Overpotential versus cycle number for mesh-supported catalysts in various electrolytes 110

C. 1 X-ray photoelectron spectra of thin-film $Ni_xFe_{(1-x)}OOH$ electrode operated in aged-OER 3 h electrolyte 112

C. 2 Cyclic voltammetry of thin-film $Ni_xFe_{(1-x)}OOH$ electrode operated in 6 ppm Fe containing 30% w/w KOH and aged-OER 3 h electrolyte 113

C. 3 UV-vis calibration curve for Fe quantification using the Fe^{2+}-1,10-phenanthroline complex.....114

C. 4 Bright red colored Fe-phenanthroline complex used for UV-Vis analysis 115

LIST OF TABLES

1.1 Electrochemical behavior of electrodes in 30% w/w KOH as a function of dissolved [Fe] 29
2.1 Surface composition (atomic %) of $Ni_xFe_{(1-x)}OOH$ and $Ni_xFe_{(1-x)}(OH)_2$ film 47

3.1 Surface composition (atomic %) of $Ni_xFe_{(1-x)}OOH$ in aged KOH using XPS 76

A. 1 Atom % of uncoated Ni mesh calculated from XPS analysis. 83
A. 2 HER and OER overpotential at $|J| = 50$ mA cm^{-2} for NiCo-PGM cell during the addition of $[Cl^-]$ at similar concentrations to what was formed during $FeCl_2 \cdot 4H_2O$ spiking. 83

A.3 Atom % calculated from XPS analysis 84

A. 4 The peak intensity ratio of Ni-O vibrations at 474–477 cm^{-1} and 549–555 cm^{-1} from in situ Raman spectroscopy of a NiCo electrode. The corresponding peak positions are given in brackets. 84

B.1 Prior literature on reverse current effects in alkaline water electrolysis 96

B.2 Electrode-specific surface composition of thin-film catalysts 99

C.1 Surface atomic composition of thin-film $Ni_xFe_{(1-x)}OOH$ electrode operated in aged-OER 3 h electrolyte before and after 100 charge-discharge cycles. 111

Chapter I

Impact of dissolved Iron on Alkaline Water Electrolysis Cells

Manasa Rajeev, Arya Jerome-Saboori, Raj Shekhar, Shannon W. Boettcher*, Paul A. Kempler*

This chapter contains co-authored work published in ACS Catalysis (*ACS Catal.* **2025**, 15, 4, 2847–2856). This work has been reproduced with permission from ACS Catalysis. The work was designed by Paul A. Kempler, Shannon W. Boettcher, and me. I collected and analyzed all the three-electrode anode data and the zero-gap analysis. Arya Jerome-Saboori conducted the three-electrode cathode studies. Raj Shekhar contributed to the collection and analysis of Raman spectroscopy. The work was written, organized, and edited by me, with editorial assistance from Paul A. Kempler.

Introduction

Alkaline water electrolysis (AWE) is the most mature and scalable approach to electrolytic hydrogen production.[1–3] Electrodes used for alkaline water-splitting reactions can be manufactured from earth-abundant transition metals (e.g., Ni, Fe, Co, and Mn)[4–6] and most often operate at temperatures ~80 °C in highly alkaline conditions (5–7 M KOH) to maximize the ionic conductivity of the electrolyte and minimize activation overpotentials at the anode and cathode.[3,7] Electrocatalysts used in industrial AWE designs have historically been composed of high-surface-area metals (e.g. Raney Ni)[8] or metal oxides that can be coated onto metal meshes at the m^2 scale. These electrodes last for years of continuous operation because they form active oxyhydroxide catalytic layers at their operating potentials that kinetically stabilize the underlying oxide and metal support in the alkaline environment. Although traditional AWE designs operate at current densities (0.2–

0.4 A cm^{-2}) that are below those of membrane electrolysis (~2 A cm^{-2}),[9] modern advanced alkaline water electrolysis (AAWE) designs minimize the ohmic resistance at the electrode-diaphragm junction and can support current densities > 1 A cm^{-2} at 1.6 V over small-cell areas.[10–12]

The electrocatalytic activity of materials used for AWE may be substantially improved through electrolyte design. The concentration and identity of supporting cations influence the reaction environment at electrocatalyst surfaces and thus affect the rate of the hydrogen evolution reaction (HER) and oxygen evolution reaction (OER).[13–17] The rate of the HER at Au(111) and polycrystalline (pc) Au surfaces is highest when weakly solvated alkali-metal hydroxides (e.g., CsOH) serve as the supporting electrolyte, whereas the opposite trend is observed for Pt(111) and pc-Pt.[16,18] The overpotential towards the OER at Ni(Fe)OOH increases by ~100 mV in 0.10 M LiOH electrolytes as compared to 0.10 M CsOH, whereas the addition of 1 mM $Ca(OH)_2$ to 0.10 M KOH leads to a similar 60 mV increase in anode overpotential.[19,20]

Electrodes for the OER are particularly sensitive to Fe at ppm (μM) concentrations: intentional doping of NiO_x anodes with 0.1% Fe resulted in a decrease in the OER overpotential of over 130 mV,[21] and adventitious incorporation of < 36 ppb Fe in 1 M KOH decreased the OER overpotential of thin-film β-NiOOH by 100 mV as compared to a purified KOH electrolyte.[22] Corrigan reported that the addition of ~10% of Fe into thin film NiO electrodes in 25% w/w KOH at 25 °C decreased the Tafel slope by 25 mV dec^{-1} suggesting a synergistic effect of Fe and Ni towards catalyzing the OER.[21] Recently, Ou et al. found that electrodes with surface Fe yield the greatest activity on a per-Fe-basis and that the Tafel slope shifts from ~60 to ~30 mV dec^{-1} for NiOOH cycled in an electrolyte

containing >0.1 ppm [Fe] as Fe accumulates at the electrocatalyst surface.[23] Demnitz reported that dissolved Fe species lowered the OER overpotential at uncoated Ni meshes in 30% w/w unpurified KOH at temperatures 75–90 °C at current densities up to 800 mA cm^{-2}.[24]

The effects of Fe on cathodes used for alkaline water electrolysis are varied. Markovic reported the activation of Pt(111) surfaces towards the HER in 0.10 M KOH via modification with $Ni(OH)_2$ and later Xue et al. showed that Ni-Fe-modified Pt(111) surfaces show enhanced performance for alkaline HER relative to Ni-modified Pt.[25] Likewise, Fe has a beneficial effect on the HER activity of uncoated Ni electrodes in 30% w/w KOH.[24] However, Fe has been reported to deactivate Ni meshes coated with platinum-group metals (PGMs) when operated in chlor-alkali environments (33% w/w NaOH at 90 °C), leading to a 100 mV cathodic shift for the HER overpotential when Fe was present at 1 ppm as compared to commercial NaOH.[26]

The impacts of dissolved Fe are important to understand and control in AWE systems as Fe is present in ppm quantities in commercial KOH, and additional Fe can be spontaneously leached from stainless-steel cell components contacting recirculated electrolytes. Although the beneficial effect of dissolved Fe in concentrated KOH on both OER and HER kinetics for uncoated Ni electrodes has been well explored in low-temperature analytical experiments,[24] the interactions between Fe and catalyst layers used in energy-efficient cells has not been characterized in conditions consistent with industrial electrolyzers. Model AAWE cells are necessary to evaluate these impacts, as the effects of dissolved Fe on high-surface-area electrocatalyst coatings operated at high current densities are likely controlled by the local environment (ionic strength, pH, temperature,

dissolved Fe concentration, electrochemical potential) produced at anode and cathode active sites.

Here, we quantify the effects of dissolved Fe at a model AAWE cell with various transition-metal-oxide anode catalysts and a PGM coated cathode.[27] We find that dissolved Fe impacts electrocatalysts used in AAWE cells in a manner that is distinct from cells composed of pure Ni electrodes or electrocatalysts operated in [KOH] ≤ 1 M, with an optimum dissolved [Fe] concentration existing within the range of [Fe] attainable for recirculated KOH electrolytes. These findings have important implications for the design of systems for hydrogen production with recirculated KOH and the design of alkaline electrocatalyst coatings.

Results

PGM-coated Ni meshes served as high-activity cathodes (**Figure 1.1e**) and were assembled with transition-metal-oxide-coated Ni mesh anodes (**Figure 1.1b**) into diaphragm-electrode packages and compressed to a final thickness of 562 μm (**Figure 1.1a**). A thick $Ni(Co)O_xH_y$ coating was prepared to simulate coatings prepared on commercial AWE anodes.[28,29] SEM images of the annealed $Ni(Co)O_xH_y$ coating showed a layered surface texture, which yielded a powder XRD pattern consistent with a $Ni_zCo_{(1-z)}O_x$ spinel phase (**Figures A.3-A.4**).[28] Anode cross sections were prepared using an Ar-plasma focused-ion beam and imaged via SEM to characterize the coating thickness and interface morphology. The PGM coating was a porous layer that was μm-scale in total thickness (**Figure 1.1e**). The $Ni(Co)O_xH_y$ catalyst coating was uniform with a total film thickness of ~1 μm but had wide cracks with separated domains and nanoscale pores distributed across the coating surface (**Figure 1.1d**).

To study the influence of the dissolved concentration of Fe, [Fe], on the electrochemical behavior of the cell, 1.0 mM $FeCl_2$ was incrementally added to 30% w/w KOH electrolyte preheated to 20 or 80 °C to a final [Fe] = 3.0–24 ppm within the model zero-gap cell. Fe^{2+} was selected as the source of dissolved Fe because of the greater solubility of ferrous species, although Fe oxidizes to Fe^{3+} in the presence of dissolved O_2. Additionally, separate addition of Cl^- as showed no significant impact on the activity of both NiCo and PGM electrodes (**Figure A.5**). Further increases to [Fe] were not investigated because the formation of precipitates was observed for [Fe] > 24 ppm.

We first compared the effect of [Fe] on the cell voltage for a series of electrodes and operating temperatures. The impact of increasing [Fe] on the total cell voltage, E_{cell}, was recorded at J = 250 mA cm^{-2} and was sensitive to both the operating temperature as well as the cathode composition (**Figure 1.2a**). A platinum-group-metal-free cell prepared

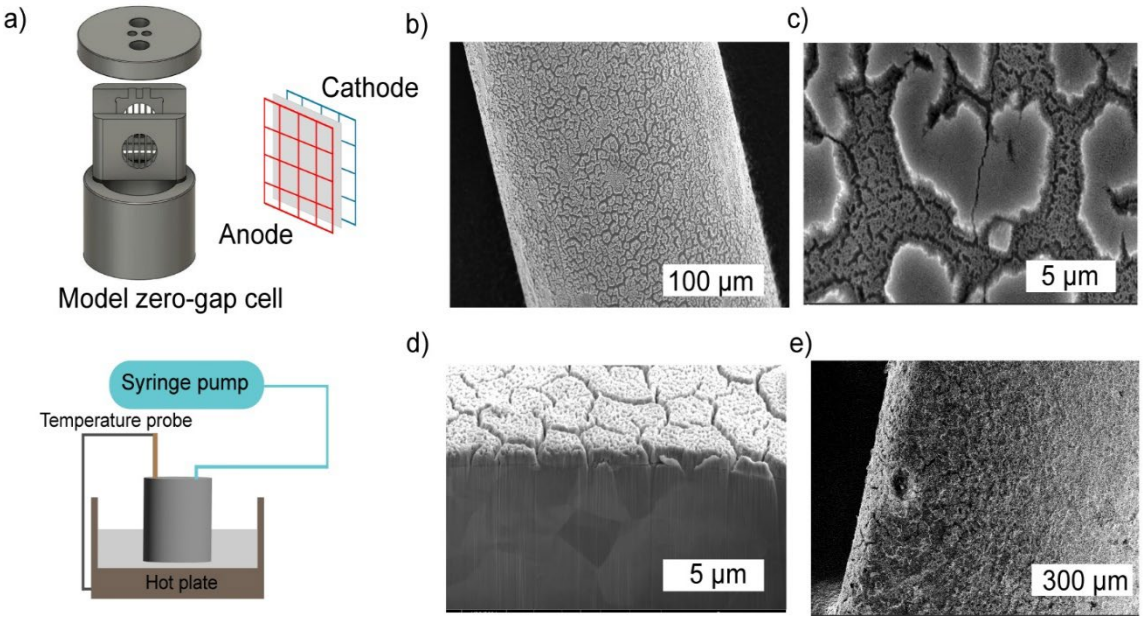


Figure 1.1: Cell set-up and characterization. (a) Schematic diagram of the model zero-gap AAWE cell showing the diaphragm-electrode assembly. **(b, c)** SEM image of the Ni(Co)O_xH_y anode prepared in this work. **(d)** Focused ion beam (FIB) cross-section of Ni(Co)O_xH_y coating on Ni mesh. **(e)** SEM image of a commercial high-

using a Ni cathode and a NiCo anode (Ni-NiCo) produced 2.15 < E_{cell} < 2.45 V at 20 °C with the lowest E_{cell} observed for [Fe] = 17 ppm, whereas the use of a commercial cathode (PGM-NiCo) yielded 1.85 < E_{cell} < 2.05 V at 20 °C, with an optimal [Fe] of 12 ppm. Data was not collected for [Fe] > 24 ppm for cells at 20 °C due to spontaneous precipitation of solid Fe species. The same PGM-NiCo cell operated at 80 °C produced E_{cell} < 1.8 V for all [Fe] < 35 ppm, with the lowest E_{cell} = 1.77(7) V observed at [Fe] = 6 ppm. Thus, rigorous control of the dissolved concentration of Fe afforded an improvement to E_{cell} at all operating temperatures. A 200–250 mV improvement in E_{cell} was observed at 20 °C as compared to a 100 mV improvement to E_{cell} at 80 °C, with the lower [Fe] required for peak cell performance as compared to an unheated cell.

Polarization curves were recorded for the top-performing AAWE configuration to investigate the mechanistic effects of [Fe] on electrolyzer behavior. **Figure 1.2b** shows the change in E_{cell} for PGM-NiCo cells during a series of galvanostatic holds from J = 10–400

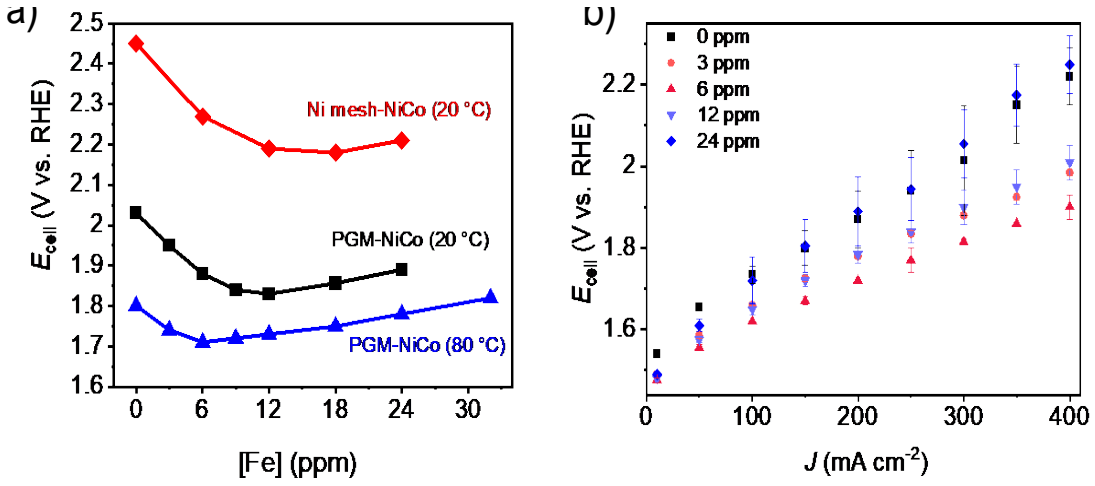


Figure 1.2: (a) Effect of Fe on the total cell voltage at J = 250 mA cm^{-2} as a function of the cell assembly and operating temperature. **(b)** J-E_{cell} behavior of PGM-NiCo AAWE cells at 80 °C for various Fe concentrations. Error bars represent one standard deviation across three independent AAWE cell trials.

mA cm^{-2} at varied [Fe] (0–24 ppm). Each E_{cell} value was recorded after 5 min of applied current. At [Fe] = 6 ppm, E_{cell} = 1.90(7) V was obtained at J = 400 mA cm^{-2}, which was > 80 mV less than the next-most-optimal E_{cell} values recorded for [Fe] = 3 and 12 ppm. E_{cell} decreased with increasing [Fe] from 0 to 6 ppm but then increased for further increases to [Fe]. The maximum impact of modifying [Fe] within a practical range for an industrial AWE cell was a 350 mV difference in E_{cell} at J = 400 mA cm^{-2}.

The long-term effect of dissolved Fe on AAWE cell voltage was studied by recording periodic galvanostatic electrochemical impedance spectra at a PGM-NiCo cell at 80 °C and J = 250 mA cm^{-2} for 150 h (**Figure 1.3**). E_{cell} remained < 1.71 V for 150 h with an average increase of 27 μV h^{-1} and R_Ω was stable at 0.33 ± 0.01 Ω. The positive impact of trace Fe on the overall cell performance was persistent and no evidence of deleterious impacts on the resistance of the separator was observed.

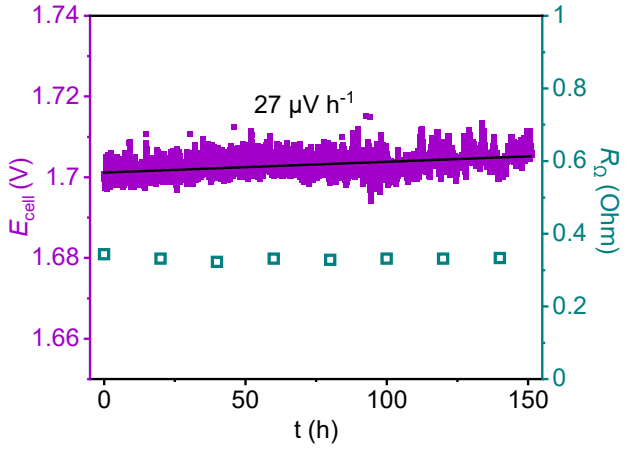


Figure 1.3: E_{cell} vs time behavior for PGM-NiCo AAWE cell at J = 250 mA cm^{-2} with [Fe] = 6 ppm. The ohmic resistance (R_Ω) was measured via GEIS at 200 kHz–100 mHz at J = 250 mA cm^{-2} every 20 h.

To understand the sensitivity of our results to the composition and design of the anode

catalyst coating, we collected a series of cyclic voltammograms for three different anodes in 30% w/w KOH at 80 °C as a function of [Fe] **(Figure 1.4)**. For the NiCo anode in [Fe] = 0 ppm electrolyte, a broad oxidation wave at E_{anode} = 1.25 V was assigned to $Co^{2+/3+}$ redox,[30] with an overlapping wave at E_{anode} = 1.34 V assigned to $Ni^{2+/3+}$ redox.[22] A single oxidation wave at 1.40 V was observed for the Ni and NiO electrodes, assigned to $Ni^{2+/3+}$ states, with an additional irreversible wave at 1.48 V assigned to the oxidation of Ni^{3+} prior to the onset of oxygen evolution. Increasing [Fe] led to a positive shift in the oxidation and reduction waves for the NiCo anode and a substantial reduction in the integrated charge under both peaks, Q_{anode}, which was quantified (**Table 11.**) from the cathodic wave to avoid the onset of the oxygen evolution reaction:

$$Q_{anode} = \frac{1}{\nu}\int_{1.25}^{1.1} J\, dE \qquad \textbf{(1.1)}$$

Similar shifts in peak potential occurred for both the Ni and NiO anodes. With the addition of Fe, the $Ni^{3+/4+}$ oxidation wave was no longer separable from the catalytic current towards the OER. Q_{anode} decreased for the NiO anode, but increased for the bare Ni electrode indicating that Fe has differing impacts on the amount of apparent redox-active

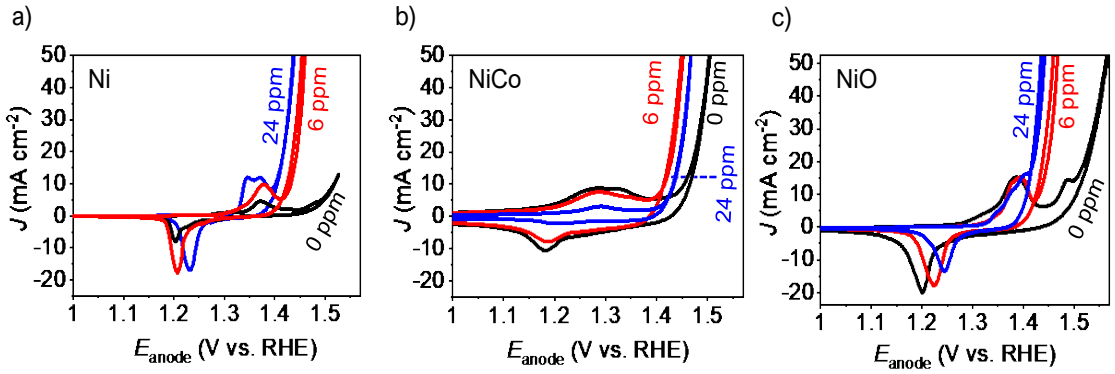


Figure 1.4: Cyclic voltammograms collected with **(a)** Ni anode, **(b)** NiCo anode **(c)** NiO anode after 60 min of conditioning in 30% w/w KOH at 80 °C at 250 mA cm^{-2} and then cycled in three different [Fe] at a scan rate (ν) = 20 mV s^{-1}. Data is shown for the second voltammetry cycle.

Ni/Co which are related to the electrochemically active surface area depending on the initial surface structure and composition of the anode.[31]

The effect of increasing [Fe] had qualitatively distinct effects on the NiCo anode as compared to the Ni and NiO anodes. Electrode activity was benchmarked as η_{50}, the overpotential required to reach $J = 50$ mA cm^{-2} towards the OER. The NiCo anode was the most-active OER electrode in [Fe] = 0 ppm electrolyte, exhibiting η_{50} that was 50 mV less positive than NiO, consistent with the higher intrinsic activity of Co-based oxides over Fe-free Ni-based systems.[32] The activity of all three electrodes increased dramatically with a small increase in [Fe] to 6 ppm. The NiCo anode had the lowest $\eta_{50} = 261$ mV whereas the uncoated Ni was slightly more active than the NiO anode ($\eta_{50} = 273$ and 280 mV, respectively). This can be understood from the lower Tafel slopes for the NiCo anode compared to both the NiO and Ni mesh anodes **(Figures A.5–A.8).** Additional dissolved Fe led to an increase in η_{50} to 280 mV for the NiCo anode whereas the uncoated Ni and NiO anodes continued to improve with increasing [Fe], yielding $\eta_{50} = 246$ and 260 mV, respectively.

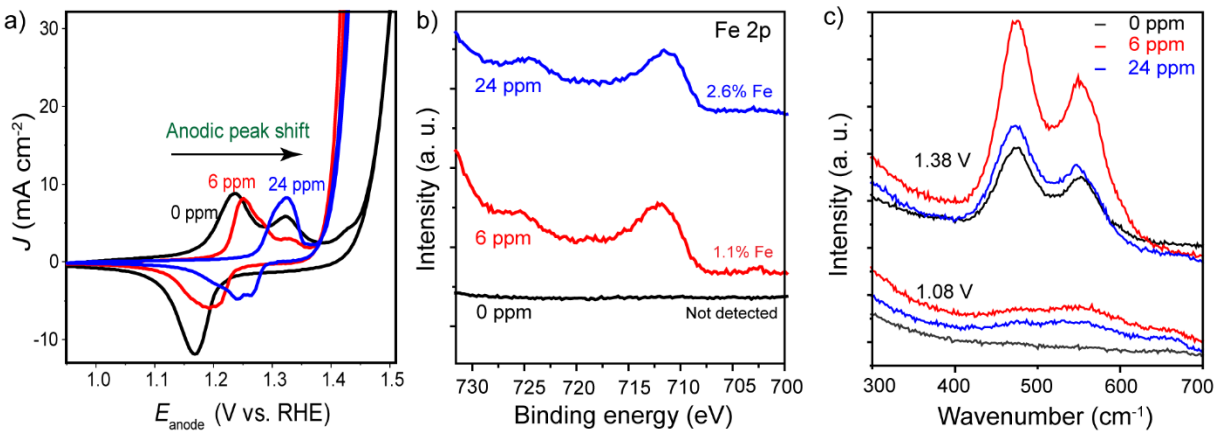


Figure 1.5: (a) Cyclic voltammogram of NiCo anode at 0, 6, and 24 ppm Fe concentration in 30% w/w KOH at 80 °C at ν = 20 mV s^{-1} after 24 h of continuous polarization at 250 mA cm^{-2} **(b)** Background-corrected XPS spectra in the Fe2p region for the NiCo anodes. The elemental composition has been calculated by the ratios of the integrated peak areas **(c)** In-situ Raman spectra of NiCo electrode in 30 wt% KOH at 60 °C recorded at 1.08 V 1.38 V. All the potentials are recorded vs RHE.

We conducted extended constant current testing at $J = 250$ mA cm^{-2} for various [Fe] on three otherwise untested NiCo anodes and quantified the surface-Fe content using X-ray photoelectron spectroscopy (XPS, **Figure 1.5b, Figure A.9)**. The amount of Fe measured on the anode surface increased monotonically with the initial concentration of Fe within the cell. The elemental composition was estimated on a metals basis, normalizing the integrated Fe $2p_{3/2}$ region to the total Ni and Co content within the anode surface. NiCo electrodes exhibited an increasingly Fe-rich surface with increasing [Fe], with a reduction in the apparent Ni content after testing in 24 ppm Fe (**Table A.1**). Cyclic voltammetry of the NiCo anodes after 24 hours of continuous operation showed a qualitative change in peak shape and a reduction in Q_{anode} relative to the as-deposited electrodes (**Figure 1.5a**). The decrease in Q_{anode} was similar for [Fe] = 6 and 24 ppm but only a single anodic wave with a peak at $E_{anode} = 1.35$ V was observed for [Fe] = 24 ppm. To further understand the

effect of dissolved Fe on the composition and structural changes of the NiCo anode, in-situ Raman measurements were conducted at 60 °C at four different potentials 0.93 V, 1.08 V, 1.23 V and 1.38 V (**Figure 1.5c, Figure A.10**). The two prominent Raman features observed at wavenumbers 474-477 cm^{-1} and 549-555 cm^{-1} have been assigned to Ni-O vibrations.[33] At all four potentials, the peak intensity increased as the Fe concentration rose from 0 ppm to 6 ppm and subsequently decreased as the Fe concentration increased from 6 ppm to 24 ppm At an Fe concentration of 6 ppm, increasing the oxidative potential from 1.23 V to 1.38 V led to a prominent increase in the wavenumber from 473 cm^{-1} to 477 cm^{-1}. In contrast, at Fe concentrations of 0 ppm and 24 ppm, the wavenumber shift was minimal, with only a few cm^{-1} observed (**Table A.2**).

The stability of PGM cathodes was evaluated while driving the HER at J = –250 mA cm^{-2} with an uncoated Ni mesh serving as a counter electrode to avoid the influence of dissolution products from anode coatings. Increasing [Fe] led to increasing absolute cathode overpotentials, $\eta_{cathode}$, for all [Fe], with $\eta_{cathode}$ reaching a steady state value within 30 min (**Figure 1.6a**). The average rate of cathode deactivation during the first 20 min at 0, 3, 6, and 24 ppm of Fe were 1.6, 5.1, 6.3, and 8.1 mV h^{-1}, respectively.

Previously, Fe has been observed to accumulate at AWE cathodes, so we tested the response of $\eta_{cathode}$ to a short-term anodic bias at $E_{cathode}$ = 0.500 V vs RHE, which was sufficiently positive to oxidize and strip dissolved Fe^{2+} species.[34] At [Fe] = 6 ppm, $\eta_{cathode}$ shifted positive by < 10 mV for a short time following anodic bias but the effect was not preserved; no shift in $\eta_{cathode}$ was observed following anodic bias for the cathode tested in [Fe] = 24 ppm (**Figure 1.6b**). The influence of [Fe] on $\eta_{cathode}$ for PGM cathodes was also assessed over 50 h of continuous testing at J = –250 mA cm^{-2} in an 80 °C electrolyte with

[Fe] = 24 ppm (**Figure 1.6c**). After the initial negative shift in $\eta_{cathode}$ over 30 mins following the addition of Fe, $\eta_{cathode}$ moved slowly positive to a steady-state value of ~ –100 mV. A 20 min potentiostatic hold at 0.500 V led to a < 10 mV positive shift which was reversed after ~30 min of continued cathodic bias at $J = -250$ mA cm^{-2}.

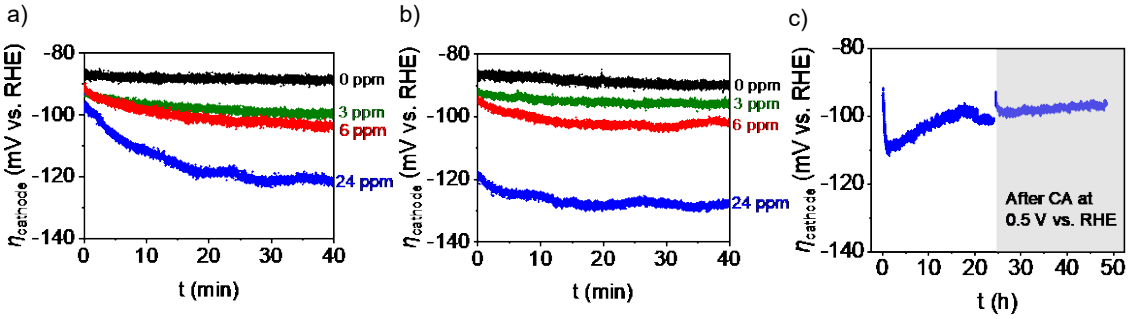


Figure 1.6: **(a)** Galvanostatic measurement of the PGM cathode as working electrode at –250 mA cm^{-2} with a Ni mesh counter electrode and RHE reference at different [Fe]; **(b)** after reverse polarization at 0.500 V vs. RHE for 20 min. **(c)** Cathodic galvanostatic measurement of the PGM cathode as the working electrode at –250 mA cm^{-2} with a Ni mesh counter electrode and RHE reference electrode in 24 ppm Fe. The electrode was polarized at 0.500 V vs. RHE for 20 minutes at $t = 24$ h.

Voltammetry of PGM cathodes showed that the HER onset potential was sensitive to [Fe] (**Figure 1.7b**). Hysteresis was observed in the HER region, with a more positive $\eta_{cathode}$ at $J = 50$ mA cm^{-2} observed during the positive-direction sweep for voltammetry in [Fe] = 0 ppm and 6 ppm. Voltammetry in 30% w/w KOH at 80 °C prior to the production of dissolved H_2 and O_2 was performed to measure the response of the hydrogen underpotential deposition (H_{UPD}) region to the presence of dissolved Fe species (**Figure 1.7a**). The integrated charge from $0.05 < E_{cathode} < 0.2$ V ($Q_{cathode}$) was stable after the third potential sweep and was inversely proportional to [Fe] but relatively stable with continued cycling. The value of $Q_{cathode}$ for the 0 ppm, 6 ppm, and 24 ppm electrolytes was 8.6, 5.2, and 1.9 mC cm^{-2}, respectively, indicating that the capacitance for H_{UPD} is diminished with

increasing [Fe] in the electrolyte and η_{50} shifted negatively by 1.3 mV for every 1 ppm increase in [Fe] **(Figure 1.7c)**. The voltametric response remained stable over 100 cycles, indicating that continued exposure to Fe-containing electrolytes and potential cycling did not lead to further consumption of active sites for H adsorption. In contrast, cycling from $0.050 < E_{cathode} < 0.500$ V led to an irreversible loss in $Q_{cathode}$ (**Figure A.11**). Thus, although $Q_{cathode}$ decreased by >75% from [Fe] = 0 ppm to 24 ppm, the loss in active surface area did not appear to be caused by continued accumulation of Fe species, consistent with the long-term stability of electrodes operating at ηcathode > –120 mV.

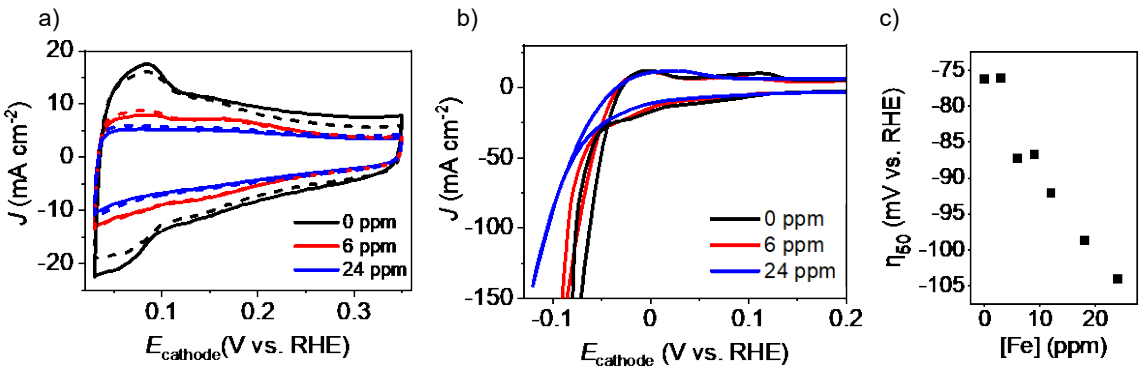


Figure 1.7: (a) Cyclic voltammetry for a PGM cathode collected at 100 mV s^{-1} in 30% w/w KOH at 80 °C as a function of [Fe]. Dashed lines represent the third cycle and solid lines represent the 100th cycle. **(b)** Cyclic voltammetry of the PGM cathode Fe at 20 mV s^{-1} in 30% w/w KOH at 80 °C with uncoated Ni as the counter electrode. **(c)** *IR*-corrected cathodic overpotential at $J = -50$ mA cm^{-2} in different Fe concentrations.

The specific activity of anodes and cathodes were compared for different electrodes and electrolytes by normalizing the current at a fixed electrode potential by the integrated charge measured in a nearby potential window prior to the onset of electrocatalytic hydrogen or oxygen evolution during linear-sweep voltammetry (**Equations 1.2, 1.3**). The

anodic sweep was used to measure the charge of the cathode to avoid the influence of the onset of HER.

$$Q_{cathode} = \frac{1}{\nu}\int_{0.05}^{0.28} J\, dE \quad \textbf{(1.2)}$$

$$J_{\mathrm{ECSA}} = \frac{J}{Q_c} \quad \textbf{(1.3)}$$

Table 1.1: Electrochemical behavior of electrodes in 30% w/w KOH as a function of dissolved [Fe]

	0 ppm Fe			6 ppm Fe			24 ppm Fe		
	$J_{(\eta 250)}$ (OER) (mA cm^{-2})	Q_{anode} (mC cm^{-2})	$J_{Q(a)}$	$J_{(\eta 250)}$ (OER) (mA cm^{-2})	Q_{anode} (mC cm^{-2})	$J_{Q(a)}$	$J_{(\eta 250)}$ (OER) (mA cm^{-2})	Q_{anode} (mC cm^{-2})	$J_{Q(a)}$
NiCo	7.4	22.3	0.3	36.4	11.9	3.1	15.0	3.2	4.7
NiO	1.0	36.4	0.02	22.1	40	0.5	67.2	24.8	2.7
Ni	1.8	9.9	0.2	26.4	17.5	1.5	58.8	19.1	3.1
	$J_{(\eta 70)}$ (HER) (mA cm^{-2})	Q_{cathode} (mC cm^{-2})	$J_{Q(c)}$	$J_{(\eta 70)}$ (HER) (mA cm^{-2})	Q_{cathode} (mC cm^{-2})	$J_{Q(c)}$	$J_{(\eta 70)}$ (HER) (mA cm^{-2})	Q_{cathode} (mC cm^{-2})	$J_{Q(c)}$
PGM	133	8.9	14.9	79.6	5.2	15.3	37.1	1.9	19.5

J at OER overpotential (η) = 250 mV, $J_{(\eta 250)}$; Absolute *J* at HER overpotential (η) = –70 mV, $J_{(\eta 70)}$; integrated charge under reduction wave at 1.18–1.25 V vs. RHE, Q_{anode}.

integrated charge under H_{des} wave at 0.05–0.28 V vs. RHE, $Q_{cathode}$. Current normalized activity for anodes, $J_{Q(a)}$ and for cathodes, $J_{Q(c)}$ (mA mC^{-1}).

For all the anodes, J_Q increased with increasing [Fe] but for the NiCo anode, this increase was offset by a large decrease in Q_{anode} at the highest [Fe] electrolytes. In general, J_{ESCA} increased by more than one order of magnitude from [Fe] = 0 ppm to 24 ppm. The most-active anode, uncoated Ni in [Fe] = 24 ppm electrolyte, was described by a Q_{anode} that was comparable to the capacitance of as-deposited NiCo and NiO coatings, but this surface coating was generated during operation at the metal mesh. Although coated Ni meshes (NiCo, NiO) initially provide a greater density of electrochemically active metal-oxide and metal-(oxy)hydroxide sites for OER catalysis, the diminished Q_{anode} in the presence of high [Fe] suggests that not all sites remain accessible to electronic- and ionic-conducting pathways necessary to support continuous electrocatalysis. For the PGM electrode, both $Q_{cathode}$ and $J_{(h70)}$ were diminished in a proportional fashion, such that we did not observe a consistent change to J_{ESCA} with increasing [Fe].

Discussion

Influence of Fe on the polarization response of electrolysis cells

The AAWE cell potential, E_{cell}, includes the thermodynamic potential for water splitting at the operating temperature and pressure, $E^{o'}(T,P)$, the ohmic voltage loss, equal to the operating J times the area-specific cell resistance R_Ω (Ω cm^2), and the overpotentials at the anode and cathode (**Equation 1.4**).

$$E_{cell}(J) = E^{o'}(T,P) + JR_\Omega + \eta_{anode}(J) - \eta_{cathode}(J) \qquad \textbf{(1.4)}$$

R_Ω is dominated by ionic resistance across the electrolyte and separator and is not expected to vary substantially with [Fe] unless there is an accumulation of Fe-containing precipitates within the microporous separator. A PGM-NiCo cell operated at 80 °C was optimized when the [Fe] = 6 ppm, yielding E_{cell} = 1.77(7) V at J = 250 mA cm^{-2}, which is greater than the [Fe] expected for purified KOH electrolytes but less than the solubility limit of [Fe], indicating that judicious control of dissolved Fe provides a route to optimize cell performance. In general, the effect of Fe on E_{cell} is lesser as cell temperature increases, with 200–250 mV improvements in E_{cell} observed via control of [Fe] at 20 °C as compared to a ~100 mV improvement to E_{cell} at 80 °C. Consistent with previous studies at uncoated Ni electrodes[24,35,36] and studies on thin film $Ni_zFe_{1-z}O_x(OH)_y$ in 1 M $KOH_{(aq)}$[22,37,38] we find that increasing [Fe] leads to a substantial negative shift in η_{anode} at uncoated Ni and NiO electrodes up to the point of Fe precipitation within the electrolyte. Increasing [Fe] also leads to changes to the electrochemically active surface area which can partially or wholly offset improvements in local electrocatalyst activity (**Figure 1.4**).

Influence of dissolved Fe on anode catalyst coatings

Consistent with previous studies on thick NiO_x films tested in 1 M KOH, the effects of Fe on the ECSA and η_{anode} were found to depend on the initial composition and thickness of the catalyst coating.[31] Previous studies on co-deposited nickel-iron (oxy)hydroxide films showed that thin films with Ni:Fe = 3:1 exhibited the maximum OER activity on a per-metal basis.[22] We find that $NiCoO_xH_y$-coated anodes yielded the lowest η_{anode} at low [Fe]—where the deleterious impact of Fe on the cathode is marginal (< 10 mV)—whereas the lowest overall η_{anode} was obtained at a NiO-coated Ni mesh tested in a Fe-rich electrolyte (**Figure 1.4**, **Table 1.1**). These results are consistent with extensive research showing that

NiO_xH_y is a poor OER catalyst in the absence of Fe but that Ni(Fe)OOH is the most effective OER catalyst in alkaline environments.[22,38] The lesser effect of [Fe] on η_{anode} at elevated temperatures is likely related to the expected exponential increase in reaction kinetics with increasing temperature as well as a reduced tendency for more-soluble Fe to partition to the catalyst surface.[6,7,39] Surprisingly, Ni electrodes exhibited comparable electrochemically active surface areas during extended testing in Fe-rich, concentrated KOH despite the initially greater Q_{anode} for NiO anodes.

The effect of [Fe] on transition-metal-oxide anode catalysts is evident in changes in the anodic peak potential, E_p^a, and integrated charge, Q_{anode}, of redox peaks before the OER. As the [Fe] was increased, Q_{anode} decreased for anodes coated with NiO and NiCo but increased for Ni. Previous studies on thin film NiCo oxide reported anodic shifts in E_p^a in the presence of dissolved Fe.[22,30] In contrast, thick NiCo coatings yielded a single, broad anodic peak from E = 1.23–1.35 V which initially did not shift substantially with increasing [Fe] (**Figure 1.4**). Moreover, at high [Fe], Q_{anode} decreases by over 80% relative to Fe-free electrolytes indicating a loss of electroactive material within the anode coating. The intensity of Raman peaks associated with Ni-O vibrations within oxyhydroxide phases decreased when [Fe] was increased from 6 ppm to 24 ppm which is consistent with the decrease in Q_{anode}. At low Fe concentrations [Fe] < 24 ppm, both NiO and Ni electrodes showed changes in both E_p^a and Q_{anode} consistent with structural transformations from NiO_xH_y to NiOOH that directly correlate to the increase in Q_{anode} and increased OER activity. At [Fe] = 24 ppm, the Q_{anode} of NiO electrode shows a decrease (~ 30%) whereas the Ni electrode showed an increasing Q_{anode} with increasing [Fe] to the soluble limit.

The changes to the electrochemical behavior of Ni-based anodes in the presence of dissolved Fe may be understood through at least three possible mechanisms: (i) Fe can induce structural changes leading to loss of catalyst material from the electrode surface (ii) supersaturated [Fe] can precipitate to form ionically insulating phases that block active redox-active sites (iii) Fe incorporation shifts the potential needed to oxidize metal hydroxides into the electrically conducting 3+ state to more positive potentials. Visual evidence of catalyst delamination and changes to Q_{anode} were not apparent within 2 voltammetry cycles, and so we focus our discussion on mechanisms (ii-iii).

Changes in the electrical response of the catalyst layer could be induced by Fe incorporation within the film. NiO_xH_y films are substantially more electrically conductive when oxidized from the 2+ to 3+ oxidation state, as in $Ni(OH)_2$ or NiO, which enables reactivity across the electrocatalytic activity of the molecularly porous surface active oxyhydroxide layer that grows on metal or metal oxide electrodes under alkaline water oxidation conditions. However, upon reduction, Ni^{3+} transforms back to $Ni(OH)_2$ phases which are comparatively more electrically insulating.[40] The potential required to re-oxidize Ni-based catalyst layers into a conducting state shifts positive with increasing Fe content within the film.[22] Likewise, thin films of cobalt oxides cycled in the presence of dissolved Fe show a positive shift in the redox wave associated with $Co^{2+/3+}$ transitions and the through-film conductivity at E_{anode} = 0.4 V vs Hg/HgO in 1 M $KOH_{(aq)}$ is reduced by ~10^3 for CoO_x films containing 54% Fe.[30] We hypothesize that electrodeposited NiO and NiCo catalyst layers undergoing potential cycling in the presence of high [Fe] may form Fe-rich phases which prevent oxidation in the potential range required to catalyze the OER in more active regions of the film. This is consistent with the observed reduction in Q_{anode} for coated

anodes in the presence of high [Fe] despite the monotonic increase in J_Q for all anodes with increasing [Fe].

Ex-situ Raman measurements of the NiCo surface after testing in high [Fe] electrolytes indicate the possible formation of α-Fe_2O_3 on the surface, which could mask the active catalyst layer lower the apparent ECSA.[41–43] α-Fe_2O_3 was observed in the NiCo sample tested in [Fe] = 24 ppm but not for an electrode tested in [Fe] = 6 ppm (**Figure A.12).** Bulk Fe oxide species are precipitated at high [Fe], and the rate of precipitation may be impacted by the local electrode potential, pH, and concentration of dissolved O_2. Establishing the exact phase of Fe (oxy)(hydr)oxide formed during operation requires interrogation of the electrode surface in the operational cell environment.

Influence of dissolved Fe on cathode catalyst coatings

The effect of Fe on AWE cathodes depends sensitively on the operating potential of the HER catalyst. Increasing [Fe] led to consistent loss in Pt active sites for hydrogen evolution, as measured by $Q_{cathode}$ in the H_{UPD} region (**Figure 1.6**) and this change was commensurate with a more negative $\eta_{cathode}$. These results stand in contrast with those observed for lower-activity Ni cathodes where previous studies at uncoated Ni cathodes with $\eta_{cathode}$ more negative than –335 mV at J = 250 mA cm^{-2} found that [Fe] = 14 ppm led to improved overpotentials for the HER. This difference is likely related to the fact that highly active cathodes for AWE operate at $\eta_{cathode}$ more positive than –120 mV vs. RHE, a potential positive of that required for the electrodeposition of metallic Fe. Although increasing [Fe] leads to an increasingly negative shift in $\eta_{cathode}$ for all [Fe], this shift stabilized within 30 min of Fe spiking and does not worsen over continued cathodic bias the ~50 h of the tests here, suggesting that no further effect on HER was observed for

electrode potentials positive of Fe metal deposition. Thus, whereas less-active transition-metal cathodes may facilitate electrodeposition of Fe and Fe-oxide species that can activate the alkaline HER (leading to a lower E_{cell}), platinum-group-metal operate at potentials positive of that required to electrodeposit Fe and are primarily impacted by dissolved or weakly adsorbed Fe species which lead to a modest ($\leq$ 30 mV) increase in E_{cell} that is proportional to [Fe].[26,44]

Implications for the design of advanced alkaline water electrolysis cells

Together, these findings suggest that the composition of catalyst coatings can be modulated for peak performance at varied [Fe], with low [Fe] being potentially desirable for high-activity cathodes, and that anode designs for Fe-rich electrolytes may reach lower overpotentials through judicious control of the metal-mesh precursor and supporting cations rather than through control of coating composition and thickness.

In this work, we have only studied the effect of Fe on the electrodes in a stagnant electrolyte. However, persistent, high levels of [Fe] may lead to precipitation that reduces the porosity of the separator and hence affects increases R_{Ω} and E_{cell}. Industrial AWE cells are operated for 1000s of hours with a recirculated electrolyte which may accumulate dissolved Fe via corrosion of pipes, gas-liquid separators, and other components external to the stack. In addition, a circulating dissolved Fe feed could lead to continuous accumulation at both the anode and cathode leading to durability issues that are not tested and are outside the scope of this manuscript. Future studies should consider circulating KOH systems and the effects of total Fe on all cell components including porous separators and ion exchange membranes.

In summary, the presence of dissolved Fe in AAWE cells consistently improved the overall efficiency for water electrolysis relative to Fe-free cells. The magnitude of this improvement is controlled by the cell operating temperature, with the shifts in E_{cell} as large as 250 mV (>10% of the operating voltage) for cells operated at 20 °C. AWE cells operated at industrially relevant temperatures (80 °C) afford lower values of E_{cell} but these are still improved by as much as 100 mV through judicious control of [Fe] (**Figure 1.2a**). The total improvement to E_{cell} is determined by a balance between Fe incorporation into transition metal oxides to form OER-active oxyhydroxide species, and the loss of HER-active surface sites at PGM-containing cathode coatings. Co-design of anode meshes, OER electrocatalysts formed during operation at low [Fe], and cathodes that are tolerant to increased [Fe] within the electrolyte are expected to lead to further reductions in the total activation overpotential for advanced alkaline water electrolyzer cells. Together, this work shows that controlling Fe impurities in advanced alkaline water electrolyzers is a key tool in designing higher performance systems.

Materials and methods

Materials: Nickel (II) nitrate hexahydrate, $Ni(NO_3)_2 \cdot 6H_2O$ (99.99%), cobalt (II) nitrate hexahydrate, $Co(NO_3)_2 \cdot 6H_2O$ (99.99%), iron (II) chloride tetrahydrate, and $FeCl_2 \cdot 4H_2O$ (> 99%,), were purchased from Sigma Aldrich. Potassium hydroxide, KOH (99.99% trace metals basis) was purchased from Thermo Fischer. ICP-MS-grade HNO_3 (Sigma Aldrich) was used to prepare stock solutions of dissolved Fe for ICP-MS analysis. Ni mesh (99.7% metals basis) was purchased from Fuel Cell Materials. All solutions were prepared from deionized water (H_2O) having a resistivity >18.2 MΩ-cm was obtained from a Millipore

Milli-Q water purification system. Stock solutions of 1 mM $FeCl_2 \cdot 4H_2O$ were prepared in 10 mM HNO_3 to ensure complete dissolution.

Electrode preparation: Ni meshes (2 cm x 2 cm) were acid-cleaned in a 20% v/v $HCl_{(aq)}$ solution for 2 min, before coating. $Ni(Co)O_xH_y$ (NiCo) anodes were deposited from a solution containing 0.50 M $Ni(NO_3)_2$ and 0.50 M $Co(NO_3)_2$ in H_2O at 20 °C via five sequential cathodic depositions at –100 mA cm^{-2} for 1 min each followed by thermal annealing at 400 °C for 15 min each cycle in air. NiO_xH_y coated Ni mesh electrodes (NiO) were prepared via five sequential cathodic electrodepositions with a constant current of –100 mA cm^{-2} for 30 s each from a precursor solution of 0.5 M Ni $(NO_3)_2$ at 20 °C followed by thermal annealing at 400 °C for 15 min each cycle in air. Uncoated Ni mesh (Ni) electrodes were acid-cleaned in 20% v/v $HCl_{(aq)}$ immediately before assembly and testing. A PGM coated cathode was obtained from De Nora Tech LLC.

Two-electrode measurements: All electrochemical measurements were collected using a BioLogic SP-300 instrument. A model AAWE cell was machined out of polyether ether ketone (PEEK), where the anode and cathode meshes (1 cm^2 projected area) were compressed on either side of the separator (Zirfon-220, 1.5 cm^2) to enforce a zero-gap geometry (**Figure A.1**). Prior -to all experiments, electrodes were pre-conditioned in 30% w/w KOH at 80 °C for 1 h at a current density *J,* of 250 mA cm^{-2}. The total cell volume contained 20 mL of electrolyte, and the solution was continuously stirred at 240 rpm using a small magnetic stir bar to help remove the produced gases from the electrolyte. During extended testing, a syringe pump was connected to the AAWE cell to replace evaporated H_2O at a flow rate of 2.7 µL min^{-1} which maintained a stable concentration of KOH.

Three-electrode measurements: Cyclic voltammetry studies were performed on electrodes in the zero-gap assembly (**Figure 1.1a**) with Ni mesh serving as the counter electrode and a reversible hydrogen electrode (RHE, Gaskatel Hydroflex) serving as the reference. For studies on cathode activity, the electrode potential was measured at –250 mA cm^{-2}, with occasional polarizations at 0.500 V vs. RHE used to understand the behavior of adsorbed species during electrolyzer shutdown and galvanostatic electrochemical impedance spectroscopy (GEIS) measurements used to monitor the changes in the ohmic resistance of the cell.

Material Characterization: Surface morphology analysis was performed by scanning electron microscopy (SEM, Thermo Fischer Apreo 2) using an accelerating voltage of 5–15 keV and an in-lens detector. X-ray Photoelectron Spectroscopy measurements (XPS) were conducted using a Thermo-Scientific ESCALAB 250 instrument with a non-monochromatic Mg-Kα source (200W, 40 eV pass energy). Powder X-ray diffraction (PXRD) data were obtained using a Bruker D2 phaser equipped with a Cu Kα source (wavelength = 1.54 Å) over a 2θ range of 20–70° with a step size of 0.2°.

In-situ Raman measurements: Electrodes were tested in a custom *in-situ* Raman cell (Figure SI) with Ni wire serving as the counter electrode and Hg/HgO as the reference electrode. The Raman objective lens was covered with a thin, translucent film of (poly)tetrafluoroethylene and immersed in the electrolyte to improve collection from the working electrode surface. The electrode was preconditioned at J = 250 mA cm^{-2} prior to the measurement. Cyclic voltammetry was collected before and after adding dissolved Fe (as $FeCl_2 \cdot 4H_2O$). Raman spectra were collected under constant potential after a 2 min

stabilization period using a 5 mW red laser (633 nm) and each spectra represents the average of 5 acquisitions (**Figure A.2**).

Chapter II

Thin-Film $Ni_xFe_{(1-X)}OOH$ Anode Catalyst Degradation in Alkaline Water Electrolyzers During Reverse Current Conditions

Manasa Rajeev, Fernanda Brito dos Santos, Shannon W. Boettcher *, Paul A. Kempler*

This chapter contains co-authored work published in *Chem. Catalysis* (*Chem Catal.* **2026**, 101845). This work has been reproduced by abiding by the copyright policies of *Chem. Catalysis*. The work was designed by Paul A. Kempler, Shannon W. Boettcher, and me. I collected and analyzed all the electrochemical data. Fernanda Brito and I contributed to the collection and analysis of XPS spectroscopy. Louka Moutarlier helped with FIB-SEM analysis. The work was written, organized, and edited by me, with editorial assistance from Paul A. Kempler and Shannon W. Boettcher.

Introduction

Alkaline water electrolysis (AWE) is the most widely deployed and economical technology for water electrolysis to produce hydrogen.[3,45,46] Advanced alkaline water electrolysis (AAWE) uses a zero-gap electrode-diaphragm assembly where each cell is connected through bipolar plates.[47,48] The use of bipolar plates and high-surface-area catalyst layers introduces design challenges associated with reverse currents, which are most problematic during interruption of power.[49,50] Positively polarized metal oxides and negatively polarized metal hydrides generate an electromotive force which can self-discharge through manifolds required to recirculate a conductive KOH electrolyte.[51,52] In this way, the electrolyzer acts as a galvanic cell following shutdown resulting in redox reactions at both the anode and cathode catalyst layers. During repeated oxidation-

reduction cycles, both anode and cathode catalysts often experience accelerated performance decay, which could be associated with mechanical stress caused by structural transformations, enhanced dissolution, and/or passivation.[53] The final resting voltage during reverse polarization is determined by the relative charge capacities of the anode and cathode. The electrode with the lowest charge capacity discharges faster, resulting in a greater change in potential relative to its operational state.[52] The magnitude of reverse current in a practical electrolyzer depends on the stack geometry, cell position, electrode capacity, and manifold resistance, with normalized current densities in prior studies ranging from –0.25 to –10 mA cm^{-2}; accelerated stress tests have typically applied reverse currents approximately ~0.2% of the operating current.[49,54] The use of thick, porous catalyst layers where the electrochemical potential varies across the population of catalyst sites can delay the impact of reverse currents, but complicates studies on the degradation mechanism. Hence, studying the dynamic behavior of thin-film Ni-based catalyst layers in industrially relevant conditions may clarify how the electrolyte environment can be modified to produce reverse-current-tolerant electrodes.[52,55]

$Ni(OH)_2$ and $Ni_{1-y}Co_y(OH)_2$ films cycled in unpurified 0.1 M KOH at 20 °C under a simulated reverse current of –5 mA cm^{-2} were previously found to degrade faster than films held under a steady state current.[49] *In-situ* surface-enhanced Raman spectroscopy of these films indicated that the oxyhydroxide phase underwent structural collapse during deep discharge events and that conversion was not fully reversed after re-oxidation.[49] Reduced $Ni_{(1-y)}Co_y(OH)_2$ films exhibited lower electronic conductivity and faster metal ion dissolution compared to the active oxygen evolution reaction (OER) catalyst.[49,54,56] Similarly, Ni-alloy (Ni-201) anodes exposed to repeated oxidation and shutdown events

showed a significant mass loss that scaled with the number and the duration of the shutdown cycle.[57] Ni-Fe alloy electrodes studied in 1.0 M KOH at room temperature showed that potential cycling to reduced conditions led to surface restructuring and enhanced OER activity.[58] The kinetics of NiOOH self-discharge in 1.0 M KOH were recently characterized by *in-situ* Raman and UV-Vis spectroscopy, revealing that the number density of Ni^{3+} sites decays linearly with time after the polarization is removed and is governed by multiple factors, including structural re-organization and hydroxide transport.[59] However, the dynamics of Ni and Fe loss during reverse currents has rarely been studied in concentrated (>1.0 M KOH with rigorous control of the concentration of dissolved transition metals).

Here we systematically investigated the factors controlling the rate of anode catalyst degradation at model thin $Ni_xFe_{(1-x)}OOH$ films in industrially relevant electrolyte conditions (30% w/w KOH, 80 °C) to understand the fundamental effects of AAWE shutdown on common Ni-Fe catalyst materials. To prepare the model electrodes, $Ni_xFe_{(1-x)}OOH$ was coated on an oxidatively stable and OER-inactive platinum foil substrate (**Figure B.1**). This allowed us to isolate the intrinsic (in)stability of both Ni and Fe in the oxyhydroxide as a function of the electrochemical potential. The loss of active material was quantified across cycle number, residence time in the reduced state, and discharge rate, and supported a model for reverse-current degradation in the absence of mechanical effects experienced at typically studied thick catalyst layers. The data also support a framework to mitigate the performance decay of Ni-based catalysts in AAWE systems powered by intermittent energy resources and may lead to the design of stable catalyst coatings that do not compromise the energy efficiency of hydrogen production.

Results

After holding the potential at J = 1 A cm^{-2} for 2.0 min, characteristic discharge curves obtained for $Ni_xFe_{(1-x)}OOH$ electrodes exhibited an extended potential plateau at

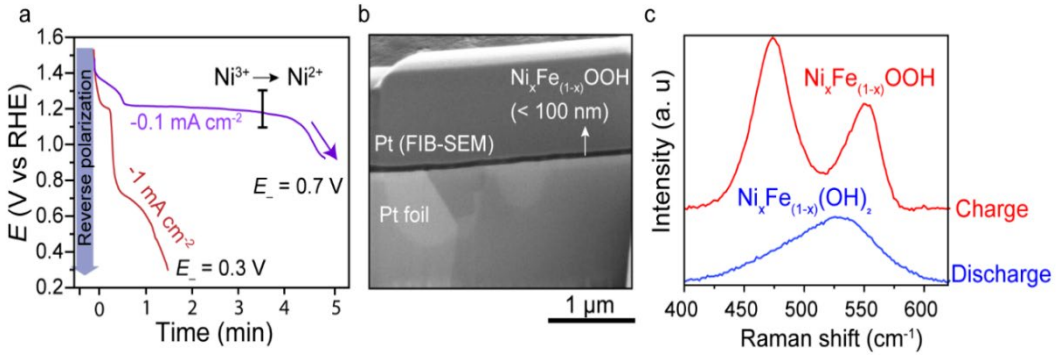


Figure 2.1: **a)** Characteristic discharge curve of $Ni_xFe_{(1-x)}OOH$ during reverse polarization showing Ni^{3+} to Ni^{2+} transition **b)** Platinum overlayer deposited cross-section SEM image of $Ni_xFe_{(1-x)}OOH$ coated on Pt foil **c)** Ex-situ Raman spectra of $Ni_xFe_{(1-x)}OOH$ and $Ni_xFe_{(1-x)}(OH)_2$ polarized in 30 % w/w KOH at 80 °C.

~1.2 vs RHE, assigned to the reduction of Ni^{3+} to Ni^{2+}, followed by a sloped region at E < 1.0 V assigned to Pt/PtO_x redox (**Figure 2.1a**). Films discharged at –0.1 mA cm^{-2} showed a small-capacity plateau at E > 1.2 V vs. RHE, positive of the oxygen reduction potential, which could be associated with higher valence states within the $Ni_xFe_{(1-x)}OOH$ film.[59] The time spent at the $Ni^{2+/3+}$ plateau was inversely proportional to the applied current, consistent with a nearly complete reduction of available Ni^{3+} sites independent of J_-. The two values of E_- investigated in this work occurred at a more negative E than the $Ni^{2+/3+}$ plateau, such that the catalyst layer was fully discharged. This is representative of a system where E_- is controlled by the redox properties of the cathode catalyst layer (i.e. where during reverse polarization discharge the cathode has more capacity than the anode causing the anode potential to fully discharge).

A focused-ion beam SEM (FIB- SEM) cross section of the $Ni_xFe_{(1-x)}OOH$ film supported on Pt showed that the films were uniform in coverage and < 100 nm in thickness **(Figure 2.1b)**. This thin-film catalyst layer was designed to avoid convoluting effects from changes in the electrical conductivity during the reoxidation of the $Ni_xFe_{(1-x)}(OH)_2$ during subsequent charging cycles. *Ex-situ* Raman spectra were collected after potentiostatic holds at E = 1.600 V (charge) and 0.700 V (discharge) for 1.0 min in Fe-spiked KOH (6 ppm) at 80 °C. A single pair of peaks corresponding to Ni-O stretching (A_{1g}) and Ni-O bending modes (E_g) were observed for the oxidized film, assigned to the $Ni_xFe_{(1-x)}OOH$ phase **(Figure 2.1c)**. The discharged film yielded a broad peak at a position characteristic of $Ni(OH)_2$, indicating a complete conversion of the Ni-O coordination environment and a film that lacked long-range order.[60,61]

The transition of NiOOH to $Ni(OH)_2$ involves multiple polymorphs whose stability depends on the applied potential and time spent in KOH.[62] The electrochemical oxidation

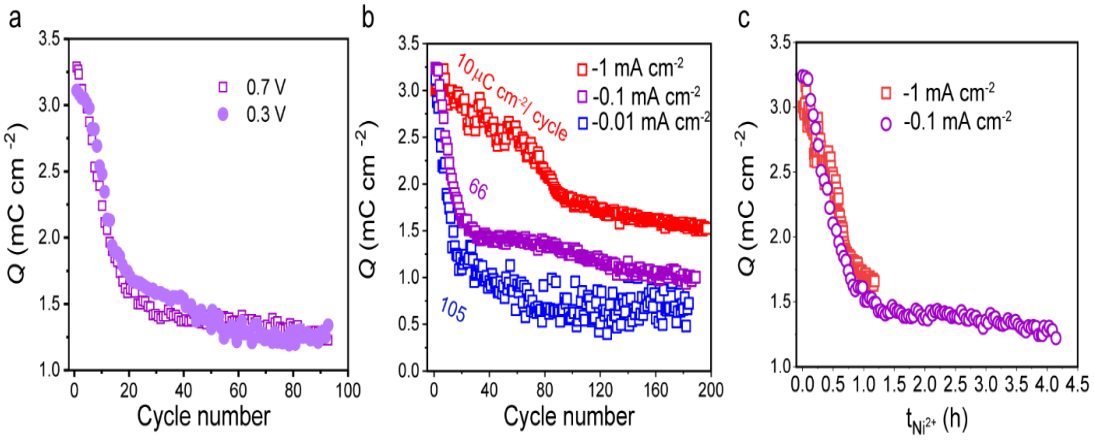


Figure 2.2: a) Discharge profile of $Ni_xFe_{(1-x)}OOH$ coated on Pt foil in 6 ppm Fe containing 30 % w/w KOH at 80 °C, where the electrode was charged at 1.0 A cm^{-2} and discharged at a constant current of -0.10 mA cm^{-2} to 0.700 V and 0.300 V vs RHE. **b)** Discharge profile of $Ni_xFe_{(1-x)}OOH$ coated on Pt foil in 6 ppm Fe containing 30 % w/w KOH at 80 °C, where the electrode was charged at 1.0 A cm^{-2} and discharged at three different rates to 0.700 V vs RHE **c)** Discharge profile as a function of the total time the electrode spent in the Ni^{2+} state.

of nickel hydroxides to nickel oxyhydroxides (nominally β and γ phases) and the subsequent reduction to the hydroxides involves two phases, α and β.[63,64] To investigate the reversibility of the nickel-iron hydroxide phase formed during discharging, two different discharge potentials were compared, corresponding to the stability window of the α (0.3 V) and β (0.7 V) phases.[63] The surface density of electrochemically active Ni sites was calculated during each charge-discharge cycle from the integrated charge density, Q, passed over a potential window of 1.100 to 1.300 V vs RHE.[65] This potential window corresponds to the Ni^{3+} to Ni^{2+} transition and is useful for monitoring Ni-redox coverage and redox reversibility; it should not be interpreted as a direct measure of the OER active sites.[65] In this way, the coverage of the $Ni_xFe_{(1-x)}OOH$ was monitored as a function of cycle number, time, and E_-. Cycling at E_- = 0.700 V and E_- = 0.300 V led to an initial steep decrease in Q followed by a gradual stabilization at ~1 mC cm^{-2} **(Figure 2.2a)**. In the first 20 cycles, >60 % of the total electrochemically accessible Ni sites were lost, whereas an additional 8% of the total sites were lost across the next 80 cycles. Initial results suggested that the loss of Ni sites was correlated to the magnitude of the applied reverse current, with the slope of the decay profile increasing from 10 μC cm^{-2}/cycle to 105 μC cm^{-2}/cycle following a two order of magnitude increase in J_- **(Figure 2.2b).** However, when the first 100 cycles were normalized to the total time the electrode spent in the reduced state, t_{Ni}^{2+}, the decay profiles collapsed into a single curve **(Figure 2.2c)**. The electrode with the

highest discharge rate (J_- = –1.0 mA cm^{-2}) spent four times less time in the reduced state as compared to the electrode discharged at J_- = –0.10 mA cm^{-2}.

For $Ni_xFe_{(1-x)}OOH$ electrodes, the dissolved Fe concentration, [Fe], in the electrolyte is a crucial factor determining the OER activity during a steady-state operation.[66] [Fe] exhibited a similarly impactful association with the retention of electrochemically active Ni sites over 100 charge-discharge cycles **(Figure 2.3a)**. Although all films lost Ni sites during the initial 10 cycles, Fe-containing electrolytes retained a substantially greater fraction of electrochemically accessible Ni. At [Fe] = 0 ppm, over 70% of the total active Ni sites were lost in the first 20 cycles, whereas > 85% sites were

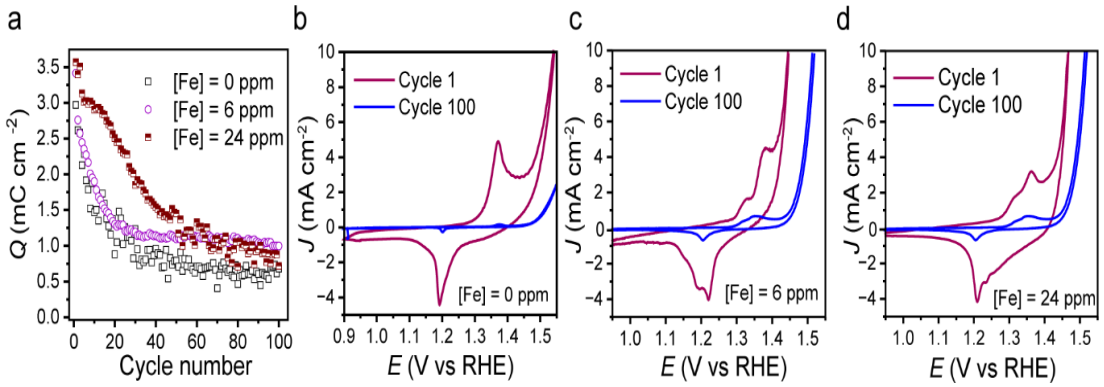


Figure 2.3: **a)** Discharge profile of NiOOH coated on Pt foil in intentionally Fe spiked ([Fe] = 0, 6, and 24 ppm) 30% w/w KOH at 80 °C, where the electrode was charged at 1 A cm^{-2} and discharged at a constant current of -0.1 mA cm^{-2} to 0.7 V vs RHE. Cyclic voltammograms of NiOOH at **b)** ~0, **c)** 6, and **d)** 24 ppm Fe concentrations collected after the first and the 100th discharge curve (v = 50 mV s^{-1}).

retained when [Fe] = 24 ppm. Both galvanostatic discharge and CV integration techniques showed a comparable initial Ni redox charge of ~ 3.2 to 3.4 mC cm^{-2} for the Fe-free and 24 ppm Fe conditions, followed by a more rapid loss in the absence of Fe **(Figure B.5)**. Although the absolute charge differed between the two methods, both techniques indicated a greater retention of electrochemically accessible Ni sites in the presence of Fe **(Figure B.6).** We approximated the intrinsic activity of catalyst films, the rate of oxygen generation

per electrochemically accessible catalyst site, by normalizing the OER activity at 1.55 V vs RHE to the cathodic charge during reduction of NiOOH to $Ni(OH)_2$, *J/Q*. *J/Q* for electrodes operated in [Fe] = 6 or 24 ppm, showed an initial decline that plateaued after the first ~ 30 cycles. [Fe] = 0 ppm showed a prominent increase in *J/Q* from 0.25 to ~1 mA mC^{-1} during the first 50 cycles **(Figure B.7)**. This apparent increase is due to the loss of catalytically inactive Ni sites, given that the initial OER activity is low in the Fe-free system. Cyclic voltammograms collected after each cycle reflected changes to OER activity during continuous restructuring of the catalyst layer. In the Fe-free system, a sharp $Ni^{2+/3+}$ oxidation peak was observed at E = 1.35 V vs RHE, which shifted anodically to 1.38 V upon Fe spiking, accompanied by the appearance of a second peak at 1.32 V vs RHE **(Figure 2.3b-c)**.

Table 2.1. Surface composition (atomic %) of $Ni_xFe_{(1-x)}OOH$ and $Ni_xFe_{(1-x)}(OH)_2$ films

Element	**Atomic %**		
	$Ni_xFe_{(1-x)}OOH$	$Ni_xFe_{(1-x)}(OH)_2$	Reoxidized $Ni_xFe_{(1-x)}OOH$
Fe	1.9(0.6)	0.4(0.2)	1.1(0.4)
Ni	29(5)	35(5)	30(6)
O	68(6)	64(5)	69(7)
Apparent Fe content (1–*x*)	0.06(1)	0.0093(5)	0.033(5)

The OER overpotential at J = 10 mA cm^{-2}, measured at the first cycle, was decreased by >100 mV when the [Fe] was increased from 0 to 24 ppm. The well-defined $Ni^{2+/3+}$ redox feature observed in the first cycle of Fe-free KOH was fully diminished by the 100^{th} cycle, but electrodes cycled in Fe-spiked electrolytes retained most redox features and a greater fraction of the initial OER activity at E = 1.50 V.

Changes in the chemical composition of catalyst films during the reverse polarization were quantified by XPS and visualized by plotting the count rate normalized to the maximum count rate from the $Ni_xFe_{(1-x)}OOH$ sample for each element. Fe content was assumed to vary continuously throughout the film and the apparent Fe content, $(1–x)$, was calculated based on the integrated Fe2p region for three independently analyzed samples for each condition, and decreased from 6% in $Ni_xFe_{(1-x)}OOH$ to <1% after reduction to $Ni_xFe_{(1-x)}(OH)$, before partially recovering to >3% upon subsequent re-oxidation. Due to uncertainty in the position and intensity of satellite peaks, the Fe2p region was not fit to individual peaks. For the $Ni_xFe_{(1-x)}OOH$ electrode, the area of the peaks in the Fe2p region diminished by over 77% following reduction to form $Ni_xFe_{(1-x)}(OH)_2$ **(Figure 2.4a-c, Table 2.1)**.[67] The decrease in the Fe2p signal in the reduced phase and the incomplete recovery of Fe content in the reoxidized phase **(Figure 2.4a)** are associated with the loss of Fe from the anode catalyst film during reverse polarization events. The changes in the Ni2p and O1s regions further indicated that the reconstructed $Ni_xFe_{(1-x)}OOH$ layer differed from the initial structure.[68] We did not attempt to fit the multiplet of peaks comprising the primary $Ni2p_{3/2}$ peak at 857 eV,[69] but note that the intensity relative to the $Ni2p_{3/2}$ satellite at 861 eV increased for the reconstructed catalyst layer, and this was accompanied by a change in the relative intensity observed for the O1s region (534–529 cm^{-1}).

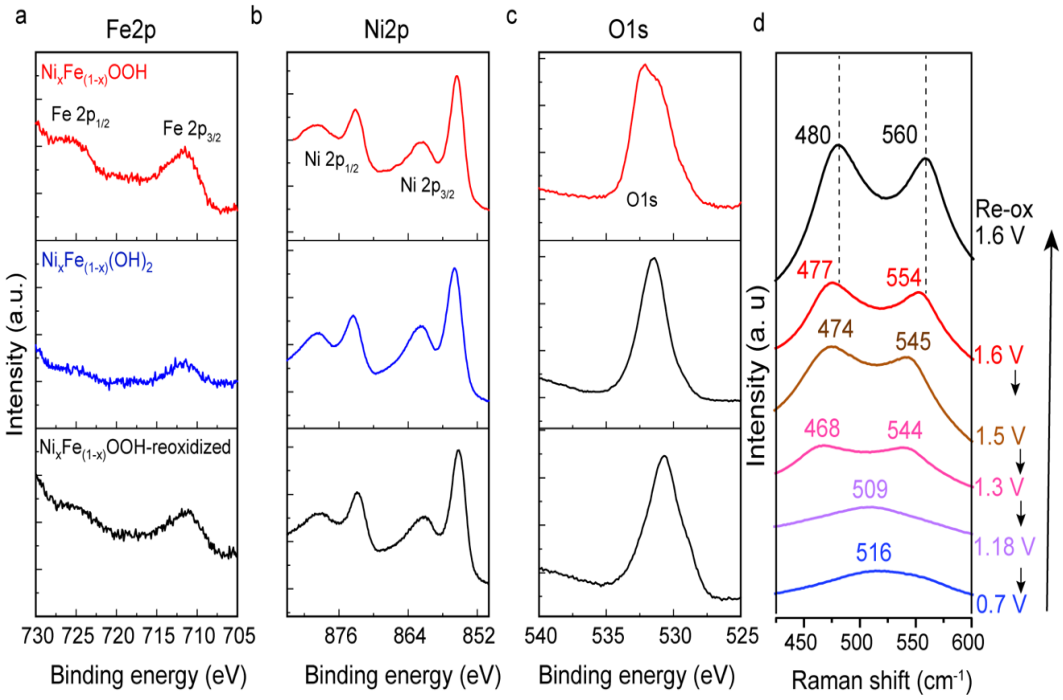


Figure 2.4:XPS data for $Ni_xFe_{(1-x)}(OH)_2$, $Ni_xFe_{(1-x)}OOH$, and reoxidized $Ni_xFe_{(1-x)}(OH)_2$ electrodes from the **a)** Fe2p region, **b)** Ni2p region, **c)** and O1s region. **d)** *In-situ* Raman spectra of NiFeOOH films in 30% w/w KOH at 60 °C, recorded at five potentials along the discharge curve.

Raman spectroscopy of NiOOH films after testing in 30% w/w KOH containing 24 ppm Fe showed red-shifts to the A_{1g} and E_g peaks to 471 cm^{-1} and 560 cm^{-1} (**Figure B.8**). Raman spectra collected at a controlled potential of 1.60 V showed two peaks at 477 cm^{-1} and 560 cm^{-1}, which were assigned to the $Ni_xFe_{(1-x)}(OOH)$ phase. At more negative *E*, the two well-defined peaks broadened, and at E = 1.30 V, the lower wavenumber A_{1g} peak shifted to ~468 cm^{-1}, which is attributed to a change in the out-of-plane vibration associated with the onset of $Ni_xFe_{(1-x)}(OH)_2$ formation. At E < 1.30 V, a single broad peak was observed, indicating a complete change in the predominant phase of the catalyst layer. Following reoxidation to 1.60 V, the peaks associated with Ni-O stretching and bending modes were blue-shifted. A comparable blue shift of ~2 cm^{-1} was also observed in ex-situ

Raman spectra at [Fe] = 6 ppm, whereas no measurable shift in the peaks resulted from reduction and oxidation in a Fe-free electrolyte **(Figure B.9-10)**. Overall, these results show that $Ni_xFe_{(1-x)}(OOH)$ catalyst undergoes a structurally reversible phase transformation along with a progressive change in the surface Fe content during discharge, which is followed by a partial recovery of Fe sites upon further charging.

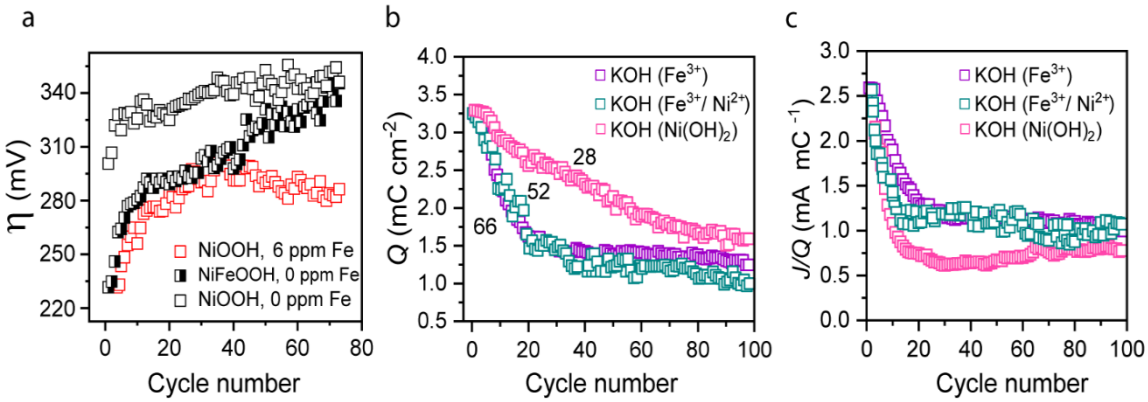


Figure 2.5: **a)** The OER overpotential at 2 mA cm^{-2} for the thin-film catalyst charged at 1.0 A cm^{-2} and discharged at –0.1 mA cm^{-2} to 0.700 V vs RHE. **b)** The discharge capacity decay for NiFeOOH coated on Pt foils in Fe-spiked KOH, $Ni(NO_3)_2$-spiked KOH, and $Ni(OH)_2$-spiked KOH. **c)** Intrinsic OER activity of thin film $Ni_xFe_{(1-x)}OOH$ measured at 1.55 V vs RHE normalized to the charge measured in **b)**.

Changes in the catalyst composition and OER activity during repeated reverse-current discharges were dependent on the Fe content of the film and trace metal impurities within the electrolyte. OER overpotentials, η, were monitored at a current density where the activity was primarily controlled by kinetics and the production of gas bubbles was minimal (2 mA cm^{-2}). NiOOH films in [Fe] = 0 ppm electrolyte yielded initial η values that were >100 mV greater than η for catalyst films operated in Fe-containing electrolytes **(Figure 2.5a)**. The OER activity continued to decrease in the absence of dissolved Fe, indicated by a further increase in η by ~ 80 mV over 100 charge-discharge cycles. NiOOH catalyst layers characterized in KOH with [Fe] = 6 ppm and $Ni_xFe_{(1-x)}OOH$ characterized

in [Fe] = 0 ppm exhibited similar initial OER activities, but η in [Fe] = 0 ppm increased rapidly over the first 50 cycles and ultimately approached the same activity as the Fe-free NiOOH electrode by cycle 60. Repeated reconstruction of $Ni_xFe_{(1-x)}OOH$ through charge-discharge cylces led to a film that behaved similarly to NiOOH in Fe-free electrolytes.

The rate of dissolution of the reduced film formed after discharge was studied by controlling the chemical potential of Ni and Fe species in the electrolyte. The corrosion reaction for $Ni_xFe_{(1-x)}OOH$ can be represented by independent **(Equations 2.1–2.2)** or coupled (**Equation 2.3**) reactions

$$Ni_xFe_{1-x}(OH)_{2\,(s)} \rightleftharpoons Fe_{1-x}(OH)_{2(1-x)} + xNi^{2+} + 2xOH^- \quad \textbf{(2.1)}$$

$$Ni_xFe_{1-x}(OH)_{2\,(s)} \rightleftharpoons Ni_x(OH)_{2x} + (1-x)Fe^{2+} + 2(1-x)OH^- \quad \textbf{(2.2)}$$

$$Ni_xFe_{1-x}(OH)_{2\,(s)} \rightleftharpoons xNi^{2+} + (1-x)Fe^{2+} + 2OH^- \quad \textbf{(2.3)}$$

Catalysts cycled in KOH spiked with 6 ppm Fe and an excess of insoluble $Ni(OH)_2$ ($Ni(OH)_2$-spiked) led to a suppression of the loss of Ni, with an average decay rate of 28 μC cm^{-2}/cycle as compared to an electrolyte with no intentional Ni addition, which decayed at 66 μC cm^{-2}/cycle **(Figure 2.5b)**. In contrast, a $Ni(NO_3)_2$-spiked electrolyte showed a nearly identical discharge profile compared to the system with only 6 ppm Fe, with an average decay rate of 52 μC cm^{-2}/cycle, indicating no meaningful suppression of Ni dissolution. Regardless of the source of Ni added to the electrolyte, loss of $Ni^{2+/3+}$ species from the catalyst film continued to occur when held in the reduced state.

The partial stabilization of the $Ni_xFe_{(1-x)}OOH$ catalyst film in $Ni(OH)_2$-spiked electrolytes was not accompanied by a commensurate stabilization of η **(Figure B.11).** $Ni_xFe_{(1-x)}OOH$ films cycled in $Ni(OH)_2$-spiked electrolytes exhibited a continuously

increasing η, whereas films tested in an electrolyte without intentional Ni^{2+} additions lost Q but maintained a steady η. The OER activity of the films (measured at 1.55 V) was normalized to the charge density of electrochemically active Ni^{3+} sites, J/Q, and indicated that Ni^{2+} spiking led to an immediate loss in specific activity such that a stable charge did not result in stabilization of catalyst performance **(Figure 2.5c)**, consistent with the loss of more active Fe sites. For both Fe-spiked and $Ni(NO_3)_2$-spiked KOH, the J/Q value decreased by ~60% in the first 20 cycles, followed by a stable activity in the rest of the testing, whereas the $Ni(OH)_2$-spiked system showed a steady J/Q value throughout the testing.

The voltammetry of thin film $Ni_xFe_{(1-x)}OOH$ in $Ni(OH)_2$-spiked electrolyte was analyzed to quantify the evolution of the redox environment and number density of Ni sites in the thin-film limit. Due to shifts in the cathodic peak, a wider voltage window (1.04–1.30 V) was used when measuring Q_c. Films cycled in $Ni(OH)_2$-spiked electrolyte initially showed a cathodic peak potential, $E_p^{c,}$ that was similar to those tested without added Ni^{2+} (~1.22 V vs RHE), but after 50 cycles, E_p^c shifted negatively to 1.19 V (**Figure B.11-12**). A shoulder feature from E = 1.06–1.16 V vs RHE was evident in the first cycle and was the dominant source of cathodic charge in the film after 100 cycles. The $Ni(OH)_2$-spiked electrolyte led to a greater separation in the anodic/cathodic charge capacity of $Ni_xFe_{(1-x)}OOH$ thin films correlated with an increase in the η and J/Q values for the OER. (**Figure B.13**)

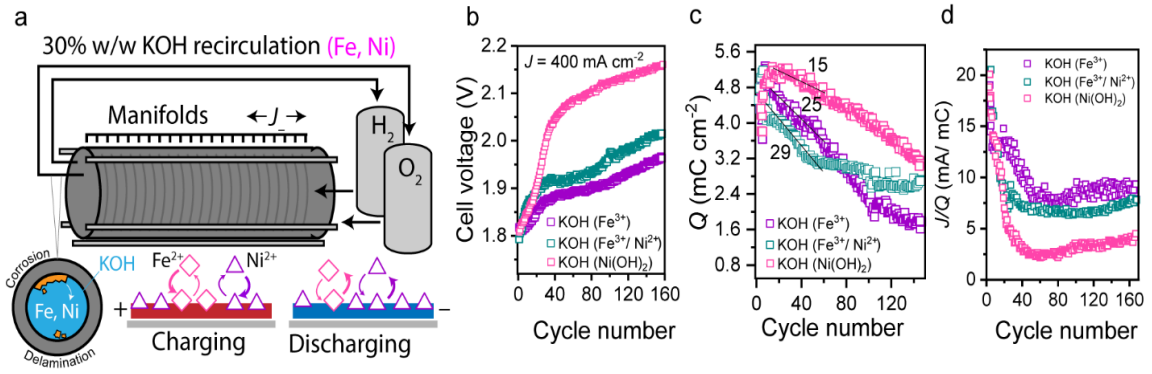


Figure 2.6: a) Scheme of zero-gap cell and components operated in 30% w/w KOH with insoluble $Ni(OH)_2$ and 6 ppm dissolved iron, showing the dynamic behavior of anode catalyst during reverse polarization. **b)** Effect of electrolyte composition on total cell voltage at $J = 400$ mA cm^{-2} for thin film $Ni_xFe_{(1-x)}OOH$ coated on Pt-Ti mesh anode and PGM cathode assembled in a zero-gap cell operated at 80 °C **c)** Discharge capacity decay for thin film $Ni_xFe_{(1-x)}OOH$ coated on Pt-Ti mesh in a zero-gap cell with 30% w/w KOH containing 6 ppm Fe in the absence of additional Ni, Fe with 6 ppm Ni, and Fe with insoluble $Ni(OH)_2$ The electrode was charged at 400 mA cm^{-2} and discharged at a constant current of -0.1 mA cm^{-2} to 0.7 V vs RHE **d)** Intrinsic OER activity of thin film $Ni_xFe_{(1-x)}OOH$ coated on Pt-Ti mesh calculated at 1.55 V vs RHE in a zero-gap cell with 30% w/w KOH containing 6 ppm Fe in the absence of additional Ni, Fe with 6 ppm Ni, and Fe with insoluble $Ni(OH)_2$.

Finally, we characterized the performance of an electrodeposited Ni catalyst layer supported on an OER-inert conductor in a zero-gap AAWE environment coupled to a high surface-area PGM-catalyst serving as the cathode. Additions of Fe^{2+} and Ni^{2+} simulated the unavoidable presence of dissolved transition metals resulting from recirculating KOH solutions through stainless steel or Ni-plated tubing, heat exchangers, and gas-liquid separators (**Figure 2.6a**), whereas addition of insoluble $Ni(OH)_2$ simulates the presence of delaminated catalyst from the electrodes during prior reverse current events. Electrodes were repeatedly charged at 400 mA cm^{-2} and discharged at $J_- = -0.1$ mA cm^{-2} to 0.700 V vs RHE. The impact of metal ion concentration in the electrolyte was monitored at $J = 400$ mA cm^{-2} as a function of cycle number.

The total cell voltage showed distinct trends depending on the presence of Fe, Ni, or $Ni(OH)_2$. While a Fe-spiked electrolyte led to an increase in cell voltage of ~140 mV after 160 cycles, the $Ni(OH)_2$-spiked electrolyte showed an increase of over 350 mV over the same number of cycles. The cell voltage increased rapidly during the first 40 cycles of the $Ni(OH)_2$-spiked electrolyte, and the rate of degradation is significantly slower in systems containing only dissolved Fe and Ni species. This trend is consistent with the zero-gap results, where the system with dissolved Fe showed a stable and lower cell voltage despite a faster decrease in the discharge capacity **(Figure B.14)**. Intentional additions of Fe and Ni led to changes in the electrochemical properties of the anode catalyst that were qualitatively consistent with thin film studies. The $Ni(OH)_2$-spiked electrolyte led to improved retention of electrochemically active Ni sites that were less active towards the OER, in comparison to electrolytes with only controlled Fe (**Figure 6c-d**). For $Ni(OH)_2$-spiked KOH, the cyclic voltammograms showed a cathodic shift of the $Ni^{3+/2+}$ reduction peak from 1.24 V to 1.20 V by cycle 160. By cycle 50, the $Ni^{3+/2+}$ reduction peak progressively broadened and shifted cathodically, suggesting gradual modification of the local Ni-Fe coordination environment leading to a Ni-rich surface **(Figure B.15)**. Electrodes in the $Ni(OH)_2$-spiked electrolyte showed a ~70% reduction in specific activity for OER compared to electrolytes spiked only with Fe, corresponding to a 100 mV increase in η (at 5.0 mA cm^{-2}) relative to the first cycle after 160 charge-discharge cycles **(Figure 6c, Figure B.16)**.

Discussion

$Ni_xFe_{(1-x)}OOH$ model thin films were characterized during repeated charge-discharge cycles that mimicked the flow of charge and dissolved metal species during intermittent operation of an AAWE system. During the charging process, the electrode is fully oxidized to the oxyhydroxide phase and during the discharging process, the spontaneous flow of reverse currents leads to reductive conversion of the catalyst layer into the hydroxide phase.[56] Monitoring the characteristic discharge profile $Ni_xFe_{(1-x)}OOH$, coupled with surface-sensitive photoelectron and Raman spectroscopies, reported on the electrochemically accessible Ni^{3+} sites throughout a variety of cycling programs and in the presence of dissolved transition metal impurities **(Figure 2.1a).**[59]

Residence time in the reduced state

The nearly overlapping *Q*-decay profiles over 100 cycles measured during polarization to 0.7 and 0.3 V vs RHE **(Figure 2.1a)** indicate that the degradation of $Ni_xFe_{(1-x)}OOH$ films is insensitive to the final discharge potential after complete conversion to $Ni_xFe_{(1-x)}(OH)_2$ (**Figure 2.1c**). This is inconsistent with a failure mode that is sensitive to the specific $Ni(OH)_2$ phases (α, β, or γ), instead indicating that these phases exhibit similar corrosion kinetics or else that β-$Ni(OH)_2$ remained as the dominant phase throughout the discharge cycle. Although the charge retention for $Ni^{2+/3+}$ was correlated with J_-, this relationship was absent after normalizing for the total time spent at $E < 1.0$ V (**Figure 2.2c**).

The total residence time of the anode in the reduced state primarily determines the degradation of the anode catalyst during reverse polarization, and this result suggests that Ni^{2+} and Fe^{3+} corrosion kinetics are not dependent on applied electrochemical potential after conversion. Thus, minimizing the time that anode catalysts in the hydroxide phase are

exposed to recirculating electrolyte and/or stabilizing the corrosion kinetics of Fe and Ni species from the hydroxide phase are strategies to stabilize this class of catalyst towards intermittent operation evident from this study.

Reconstruction of $Ni_xFe_{(1-x)}OOH$ catalysts

Surface-sensitive Raman and X-ray photoelectron spectroscopy characterized the composition and structure of (oxy)hydroxide catalysts during cycling. The reconstruction process to form $Ni(OH)_2$ and $Ni_xFe_{(1-x)}(OH)_2$ could be monitored by Raman spectroscopy, where the peaks present at 477 and 560 cm^{-1} were replaced by a single broad peak at 509 cm^{-1}, consistent with a complete conversion of the thin-film catalyst **(Figure 2.4d)**. In KOH electrolytes with [Fe] = 0 ppm, two Raman peaks remained after discharge to 0.700 V, with a lower wavenumber peak that was unchanged from the original A_{1g} mode observed for NiOOH and a higher wavenumber peak similar in energy to the peak observed for $Ni_xFe_{(1-x)}(OH)_2$. This is direct evidence of Fe^{3+} cations affecting the reconstruction pathway and modifying the environment of the reduced catalyst layer.

Surface Fe^{3+} is evidently less stable in $Ni_xFe_{(1-x)}(OH)_2$ layers than the oxidized catalyst, and the potential dependence of x was measured directly by XPS and indirectly by shifts in the in-situ Raman spectra **(Figure 2.4a-d)**. This change is partially reversible, as the A_{1g}/E_g ratio increased from 1.01 to 1.68 when the catalyst was re-oxidized after a complete reduction to $Ni_xFe_{(1-x)}(OH)_2$. The average surface Fe content of the film $(1-x)$, increased from 0.4% ± 0.2% to 1.1% ± 0.4% during re-oxidation, which was less than the "as-conditioned" value of 1.9% ± 0.6%, and this shows that reverse current events reduce the Fe content of the catalyst layer in a manner that is not kinetically reversible **(Table 2.1)**. Although charging effects during XPS could lead to systematic errors in the reported Fe

content of the film, the result that reduced $Ni(OH)_2$ catalyst layers consistently contained less Fe than the same catalyst layers after re-oxidation in Fe-containing electrolytes was robust. Reconstructed catalyst layers may lack Ni-Fe sites associated with the initially high OER activity, as indicated by the immediate increase in overpotential and declining J/Q over the initial cycles (**Figure 2.5a**).[49]

Degradation is not described exclusively by the loss of electrochemically active sites (Q) but also changes in the intrinsic catalytic activity of the film. This observation is consistent with the view that OER activity is governed primarily by dynamically evolving surface Fe sites, which can form through continuous dissolution and redeposition under operating conditions.[23] This behavior may differ substantially from that of bulk NiFeOOH, where Fe is incorporated throughout the catalyst structure during synthesis.[70] Ni-based electrodes used for intermittent AWE have been previously reported to exhibit repeated uptake and loss of Fe from the electrolyte, which was implicated as a reversible mode of degradation.[71] Poli et al. further showed that periodic regeneration can restore the Fe sites lost during OER and maintain extended stability for Ni anodes.[72] However, in our study, $Ni_xFe_{(1-x)}(OH)_2$ thin films on an inert Pt substrate appeared to be more prone to dissolution in the reduced states compared to the high valent Ni states.

The rate of Ni and Fe dissolution is influenced by the chemical potential of these species within the KOH electrolyte. The number of cycles required to reach a charge capacity, Q, of 2.0 mC cm^{-2} increased from ~5 to 30 as [Fe] was increased from 0 to 24 ppm (**Figure 2.3a**). Films cycled in electrolytes with [Fe] = 0 showed no clear redox peaks after 100 cycles, but when [Fe] was increased to 24 ppm, the anodic peak potential, $E_{\mathrm{p}}^{\mathrm{a}}$ shifted negatively by ~20 mV accompanied by a reduction of peak intensity by ~60 %

(Figure 2.3b, d). Thus, both the rate of Fe and Ni loss is suppressed by the presence of dissolved Fe, which suppresses the net dissolution rate in the discharged state and/or accelerated recovery of $Ni_xFe_{(1-x)}OOH$ upon reoxidation. This is more consistent with a collective corrosion mechanism (**Equation 2.3**), in which the kinetic stability of both metals is affected by the corrosion products of the solid phase. However, the nearly identical decay of electrochemically active Ni sites for electrolytes spiked with both Fe and Ni indicates that at industrially relevant dissolved Ni^{2+} concentrations, Ni does not meaningfully suppress metal dissolution. The $Ni(OH)_2$-spiked electrolyte further extended the cycle life of similarly prepared catalyst layers to >55 cycles to 2.0 mC cm^{-2}. However, measurements of total integrated charge do not directly correlate with the OER activity since they do not account for the adsorbed Fe content or the retention of Fe-associated active sites.[73]

Whereas $Ni_xFe_{(1-x)}OOH$ films cycled in electrolytes spiked with only Fe showed a stable E_p^c, the presence of dissolved Ni^{2+} led to a negative shift in E_p^c and an increasing charge capacity at more negative potentials. This suggests the presence of redox-active, but OER-inactive, NiOOH sites rather than $Ni_xFe_{(1-x)}OOH$ and once again suggests that the charge capacity of $Ni^{2+/3+}$ alone is not a meaningful predictor of the stability of the original $Ni_xFe_{(1-x)}OOH$ catalyst. Fe^{3+} dissolution is relatively reversible following discharge events, but the irreversible dissolution of Ni^{2+} sites has more long-lasting consequences for catalyst activity. The continual replenishment of surface Fe from soluble Fe species creates a dynamic surface equilibrium that may protect the Ni sites from deleterious degradation processes.

Implications for zero-gap alkaline electrolyzers

The overall performance of the zero-gap cell is significantly affected by the identity and concentration of metal species in the electrolyte. Thissen *et al*. showed that the stability of a Ni-Fe anode and Ni cathode during cycling between oxidation and shutdown conditions is influenced by the Fe dissolution-intercalation mechanism, where the cathode becomes more active due to active Fe deposition and the anode becomes less active due to incomplete Fe insertion.[71] Here, the use of a low-overpotential platinum-group-metal cathode minimized the impact of iron metal deposition at the cathode. We find that the intentional addition of insoluble $Ni(OH)_2$, which could be a product of catalyst delamination, slowed the rate of Ni dissolution during reverse polarization in both the three-electrode and zero-gap configurations (**Figure 2.5b, 6c**). The thin-film $Ni_xFe_{(1-x)}OOH$ in the presence of 6 ppm Fe exhibited a ~70% loss of active Ni sites, which was suppressed in the $Ni(OH)_2$-spiked electrolyte to ~48% over a similar number of cycles. However, insoluble $Ni(OH)_2$ also led to an increased total cell voltage, possibly due to interactions with the concentration of free $Fe^{2+/3+}$, compared to low concentrations of dissolved Fe^{3+} and Ni^{2+} in the electrolyte (**Figure 2.6b**).

Suspended $Ni(OH)_2$ and $Ni_xFe_{(1-x)}(OH)_2$ impacted the specific activity of thin film catalysts during intermittent operation. Although electrodes and electrolyzers cycled in the presence of suspended $Ni(OH)_2$ exhibited greater charge retention, the primary effect was a loss in specific catalyst activity, which occurred over < 20 cycles (**Figure 2.5c**, **2.6d**). This could be caused by a lower activity of dissolved Fe, caused by scavenging of free Fe species by $Ni(OH)_2$. The broadening of the anodic wave at $E > 1.3$ V concurrent with a +0.040 V shift in E_p^a **(Figure B.8)**, along with a negative shift in the E_p^c, is mostly

consistent with $Ni(OH)_2/Ni_xFe_{(1-x)}OOH$ particles that are resistive or in poor contact with the conducting substrate, rather than indicating a change in the Fe content of the film which leads to a positive shift in both the anodic and cathodic waves. This is consistent with the preservation of *Q* along with declining OER activity in the presence of $Ni(OH)_2$. These results suggest that the removal of these suspended catalyst particles is important for the stability of the remaining catalyst layer.

The impacts of Fe^{2+}, Ni^{2+}, and $Ni(OH)_2$ on the electrochemical behavior of the $Ni_xFe_{(1-x)}OOH$ films are related to the Fe content of the solid phase **(Figure 2.7)**. $Ni_xFe_{(1-x)}OOH$ is well known to adsorb soluble Fe from KOH electrolytes, impacting the catalyst water-oxidation activity (**Figure 2.7a**). The dominant effect of dissolved Fe on the OER properties of Ni-based layered oxyhydroxides is also reflected in the stability of these catalysts during repeated charge/discharge cycles. Here we report that 70% of the Fe cations are released during a 30 min hold in the reduced $Ni_xFe_{(1-x)}(OH)_2$ state, and that the addition of soluble Fe leads to improved retention of Ni sites (as measured via charge capacity). These soluble transition metals most likely stabilize the solid by reducing the *net* rate of dissolution for the mixed-metal oxyhydroxide during conversion. When the catalyst is in the reduced state (**Figure 2.7b**), the impact of dissolved Fe on the net corrosion rate of Ni suggests that the dissolution processes for both Ni and Fe are coupled (**Equation 2.3**), or that the high chemical potential of Fe in the electrolyte supports a higher surface Fe concentration, which kinetically slows the Ni^{2+} dissolution. Dissolved Ni^{2+} had a comparatively minor impact on the preservation of redox-active Ni sites, which suggests that dynamic exchange of Fe with the electrolyte is the primary driver of catalyst dissolution in Ni-based alkaline electrolyzers.

Multiple dissolved transition metal species are expected in a realistic AAWE environment due to the use of stainless steel and Ni alloys in piping and gas-liquid separators (**Figure 2.6a**). Bulk Ni electrodes serve as a Ni reservoir for the active catalyst layer, and this maintains a continuous supply of Ni sites that can interact with catalyst sites lost to dissolution during the discharged state. Separating and understanding catalyst degradation from the substrate is key in designing reverse current-tolerant, highly active catalyst-coated porous, practical anodes. A critical distinction of our study from many previous Ni electrode-based studies is the use of an inert and non-passivating Pt substrate which isolates the *intrinsic* catalyst-layer changes from corrosion and passivation reactions at the substrate. Interactions with Ni^{2+} and $Ni(OH)_2$ are not always favorable to the total catalyst activity, and these studies quantified the chemical effects of reverse polarization at $Ni_xFe_{(1-x)}OOH$ alone. Studies involving Ni substrates are representative of typical cell constructions but may overestimate the intrinsic durability of the solid and underestimate the intrinsic OER activity because the chemical potential of Ni and Fe is poorly defined. Other transition metals, such as Co, may impact the ultimate fate of Fe. This study employed simplified shutdown transients, a thin-film catalyst layer model, and was limited to <50 h of testing. Dissolution and delamination could be distributed in a complex manner throughout a porous electrode, making the macroscopic effect of repeated shutdowns difficult to predict solely from studies at thin films. The proposed degradation mechanisms explored in this work are expected to be relevant to catalyst layers supported on Ni or stainless steels but these supports could influence the local concentration of dissolved transition metals in a manner that is difficult to predict from this study alone. Future studies

should examine how dissolution and delamination occur in porous anodes under longer-term stack operations and with more realistic shutdown conditions.

$Ni_xFe_{(1-x)}OOH$ films produced from Ni coated on Pt-Ti mesh showed initial activation over the first 20 cycles, likely associated with continued formation of the layered oxyhydroxide film *in-situ* at the Ni metal surface. The mitigated decay rate (15 μC/cycle) at the zero-gap mesh, as compared to 27 μC/cycle at the thin film $Ni_xFe_{(1-x)}OOH$, could be a balance between continued oxidation of the metallic Ni and dissolution/passivation of the catalyst layer. This configuration is representative of stability observed at Ni meshes and Ni-plated steels used as anodes in AWE cells and suggests that electrolyte engineering can benefit the system even in the presence of a large excess of solid Ni. For both thin films and zero-gap mesh electrodes, stabilization of redox active $Ni^{2+/3+}$ comes with the expense of a reduction in the charge-normalized activity of the catalyst layer and generally reduces the performance of the anode (**Figure 2.5c-d, Figure 2.6c**).

Here, we find that coupled interactions with dissolved Ni^{2+} have a minor impact on charge retention and that electrolytes containing $Ni(OH)_2$ preserve surface charge but lower the activity of the catalyst layer. Catalyst layers have been stabilized via dynamic exchange with electrolyte impurities during the OER in neutral and acidic environments.[74,75] Future studies on dynamically stable $Ni_xFe_{(1-x)}OOH$ films should seek to identify dissolved species that suppress the corrosion of Ni^{2+} while also maintaining a high content of Fe^{3+} sites within the catalyst layer. Recent online inductively coupled plasma mass spectrometry results from Marquez et al. show that potassium phosphate could assist in this role.[49] Intentional control of the composition of recirculating electrolytes may lead to catalyst layers that maintain robust activity within an AAWE system during repeated start-up and shut-down events.

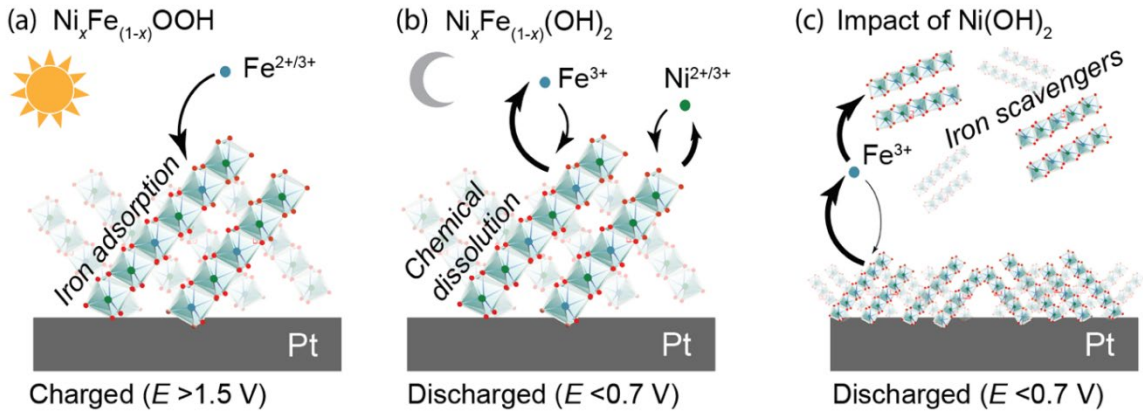


Figure 2.7: Processes affecting anode catalyst stability during repeated charge/discharge cycles. **a)** $Ni_xFe_{(1-x)}OOH$ formation leads to Fe uptake and forms an active O_2 evolving catalyst **b)** electrochemical reduction to $Ni_xFe_{(1-x)}(OH)_2$ is followed by chemical dissolution of Ni and Fe, leading to loss of Q and catalyst activity. **c)** Recirculating $Ni(OH)_2$ lowers the activity of soluble Fe, increasing the effective rate

Materials and methods

Materials: Nickel(II) nitrate hexahydrate, $Ni(NO_3)_2 \cdot 6H_2O$ (99.99%), and iron(III) nitrate nonahydrate, $Fe(NO_3)_3 \cdot 9H_2O$ (> 99.95%, trace metals basis) were purchased from Sigma Aldrich. Potassium hydroxide pellets, KOH (>99.98 %, metals basis), were purchased from Thermo Fisher Scientific. Deionized water, H_2O, with a resistivity of >18.2 MΩ-cm was obtained from a Millipore Milli-Q purification system. Nickel hydroxide, $Ni(OH)_2$, was prepared by precipitating 3 M $Ni(NO)_3 \cdot 6H_2O$ in 1.0 M KOH. The precipitate was washed three times with H_2O and dried in an oven at 50 °C. The precipitate purity was confirmed using powder x-ray diffraction **(Figure B.2)**.

Preparation of thin-film nickel-iron oxyhydroxide (NixFe(1-x)OOH) and nickel oxyhydroxide (NiOOH) electrodes: Platinum foil (0.8 cm^2) was cleaned using aqua regia (3:1 v/v HCl: HNO_3) and H_2O. An aqueous solution of 0.50 M $Ni(NO_3)_2 \cdot 6H_2O$ was spin-coated onto the Pt foil (3000 rpm, 15 s) and then dried on a hot plate set to 60 °C for 5 min. The thin film was then electrochemically cycled at a constant scan rate of 50 mV s^{-1} in 30% w/w KOH at 80 °C until a stable voltammogram was obtained. Electrodes conditioned in Fe-free KOH are referred to as NiOOH, whereas those conditioned in KOH containing 6 ppm Fe are referred to as $Ni_xFe_{(1-x)}OOH$.

For studies in the zero-gap AAWE environments, Pt was e-beam evaporated onto a Ti mesh (Pt-Ti), and this mesh served as a substrate instead of Pt foil. A controlled amount of Ni metal was electrodeposited onto Pt-Ti mesh from a bath containing 0.50 M $NiCl_2$ and 0.50 M $NiSO_4$ at a geometric current density, $J = -50$ mA cm^{-2} for 30 s. The electrode was then oxidized at 1.6 V for 30 min in 30% w/w KOH containing 6 ppm Fe at 80 °C. The cell

was assembled with a commercial PGM-based electrode as the cathode, which we previously found to be stable against Fe plating,[66] and Zirfon-220 as the separator. Both electrodes had a geometric area of 1 cm², while the separator had an active area of 1.5 cm². Additional details on the cell construction can be found in the supplementary information.

Charge-discharge analysis: All electrodes were "charged" at 1.0 A cm^{-2} towards the OER for 2.0 min in 30% w/w KOH at 80 °C in a three-electrode arrangement with Ni wire serving as the counter electrode and a reversible hydrogen electrode (RHE, Gaskatel Hydroflex) as the reference electrode. Electrodes were galvanostatically "discharged" at a constant rate, J_- (–1 mA cm^{-2}, –0.1 mA $cm^{-2,}$ and –0.01 mA cm^{-2}), to either 0.700 or 0.300 V vs RHE. Together, these charging and discharging steps constitute a single "cycle". We chose to use a single discharge current during electrode cycling to explicitly study how the rate and duration of the anode discharge reaction impacts catalyst lifetime.[52,76] The discharge current-potential profile at a bipolar plate is better defined by a constant resistance, which is typically defined by the electrolyte manifold resistance and the position of the cell within the stack,[55,77] but this leads to varied rates of discharge across the stack and even across an individual, large-area electrode. The charge-discharge studies were performed in a 1 cm^2 zero-gap assembly **(Figure B.3)**, with a commercial cathode containing a PGM mixture serving as the cathode. The electrode was charged at 400 mA cm^{-2} and discharged at $J_- = –0.1$ mA cm^{-2} to 0.700 V vs RHE.

Studies on electrolyte composition: To study the impact of dissolved metal ions on the reversible charging behavior of Ni electrodes, three different electrolyte compositions were used. Fe-spiked electrolytes were prepared by adding Fe^{3+} to 30 % w/w KOH from a standard solution containing 3.0 mM iron(III) nitrate nonahydrate solution, adjusted to pH

= 2.0 using nitric acid. A $Ni(NO_3)_2$-spiked electrolyte was prepared using a 0.10 M $Ni(NO)_3 \cdot 6H_2O$ solution, which was added to 30 % w/w KOH containing 6 ppm Fe at 80 °C to a total Ni content of 6 ppm. A $Ni(OH)_2$-spiked electrolyte was prepared by adding ~0.025 g of $Ni(OH)_2$ to 6 ppm Fe containing 30 % w/w KOH at 80 °C until a solid $Ni(OH)_2$ precipitate was visible, and this precipitate was present in the cell during electrolysis **(Figure B.4)**.

In-situ Raman spectroscopy: A custom cell machined out of polytetrafluoroethylene (PTFE) was used for spectroscopy of $Ni_xFe_{1-x}OOH$ films on Pt foil under controlled electrochemical potential. A Ni wire served as the counter electrode and the reference electrode was Hg/HgO. The optical objective was protected with a thin, translucent PTFE film and immersed in KOH electrolytes heated to 60 °C. A 633.78 nm red laser (5 mW) was used to acquire the spectra, and the final spectrum was averaged over 10 acquisitions of 20 s each.

X-ray photoelectron spectroscopy (XPS): XPS measurements were conducted using a Thermo-Scientific ESCALAB 250 instrument calibrated with Au 4f7/2, Ag 3d5/2, and Cu 2p3/2. A Mg–Kα X-ray source was powered at 200 W, with 50 eV pass energy, and an energy resolution of approximately 0.1 eV. A low-energy electron flood source was used for charge neutralization during all high-resolution measurements. The analysis chamber pressure was maintained below 1.0×10^{-7} mbar, and the analyzer pressure was below 1.0×10^{-8} mbar. XPS spectra were collected from a $Ni_xFe_{1-x}OOH$ sample first held at 1.600 V vs RHE for 30 min in [Fe] = 6 ppm KOH. Then, the same sample was held at 0.700 V vs RHE for 30 min to form nickel–iron hydroxide ($Ni_xFe_{1-x}(OH)_2$), and a second spectrum was collected. Finally, $Ni_xFe_{1-x}(OH)_2$ was again held at 1.600 V for 30 min to form

reoxidized $Ni_xFe_{1-x}OOH$, and a third spectrum was acquired. Atomic percents of Ni, Fe, and O were calculated from the total integrated peak intensity in the Ni2p, Fe2p, and O1s regions using a Shirley background.

Chapter III

Effect of Reverse Polarization on Thin-Film NiFe $_{(1-X)}$OOH in Realistic AWE Electrolytes Containing Dissolved Metals

Manasa Rajeev, Joseph Daddon, Fernanda Brito dos Santos, Shannon W. Boettcher *, Paul A. Kempler*

The work was designed by Paul A. Kempler, Shannon W. Boettcher, and me. I collected and analyzed all the electrochemical data. Joseph Daddona contributed to the collection and analysis of Fe precursor solution studies. Fernanda Brito contributed in collection ahnd analysis of XPS. The work was written, organized, and edited by me.

Introduction

Industrial AWE systems consist of several separator-electrode assemblies, where the hydrogen and oxygen evolution half-reactions occur, coupled to a balance-of-plant (BoP) comprising piping that recirculates the electrolyte, pumps, heat exchangers, gas-liquid separators, etc.[78,79] The BoP surfaces are constantly exposed to concentrated caustic (30–40% w/w KOH) solutions at elevated temperatures (70–90 °C) and pressure up to 30 bar; the commonly used materials for fabricating them are austenitic stainless steels (grade 304 L and 316 L).[78,79] The stress corrosion cracking (SCC) studies on Ni-based alloys and austenitic stainless steel components under realistic AWE operating conditions show a direct correlation with the dissolved gas environment under realistic AWE operating conditions, material composition, and position in the system.[80,81] Such composition- and environment-dependent corrosion behavior is relevant to which alloying metals (e.g., Ni, Fe, Cr, Mn, Mo) are dissolved and subsequently affect the overall performance of the

electrolyzer over long-term operationaffect the overall performance of the electrolyzer over long-term operation.[79,82]

Iron dissolution-redeposition equilibrium during reverse polarization in KOH with dissolved iron has been studied previously. Under dynamic operation conditions, Fe in $Ni_xFe_{(1-x)}OOH$ catalysts undergoes potential-dependent dissolution and surface restructuring.[49,83] In contrast, studies on mixed nickel–iron (MNF) catalystsIn contrast, studies on mixed nickel–iron (MNF) catalysts by Kuai et al. showed that during OER, surface Fe segregates into iron oxyhydroxide phase (FeOOH), which reverts to the active NixFe(1-x)OOH phase during the oxidation step, regenerating active sites.[84,85] However, the effect of reverse polarization on long-term structural stability and OER activity for $Ni_xFe_{(1-x)}OOH$ catalysts in industrially relevant electrolyte compositions containing dissolved metals such as Fe, Cr, Ni, and Mn released from BoP corrosion has scarcely been studiedreleased from BoP corrosion has scarcely been studied.[86]

The effect of dissolved Cr and Mn on AWE anodes shows varied results. Jiao et al. showed that sputtered NiFeCr alloy thin films form Cr-doped $NixFe_{(1-x)}OOH$ electrodes and enhance OER activity by lowering the d-band centersJiao et al. showed that sputtered NiFeCr alloy thin films form Cr-doped $NixFe_{(1-x)}OOH$ electrodes and enhance OER activity.[82] Studies on $Ni_{0.7}Fe_{0.16}Cr_{0.12}OOH$ in 1 M KOH resulted in stable OER activity at 600 mA cm^{-2} for over 100 h $NixFe_{(1-x)}OOH$ catalyst with a specific activity 38 times higher than that of the undoped.[87] Vendrame et al. studied the role of Cr and Mn in NiFe mixed-metal spinel oxides, $NiFe_{2-x}M_xO_4$ (M = Cr, Mn), in 0.1 M KOH at room temperature. Unlike the substantial promotional effect of Cr^{3+} on the OER kinetics, the Mn-doped sample showed only an apparent increase in OER activity with an increased surface area

rather than any improvement in the OER kinetics.[88] These results together show that dissolved metal impurities like Cr and Mn in the recirculating electrolyte may actively participate in enhancing the OER activity of $Ni_xFe_{(1-x)}OOH$, but it remains unclear whether this effect is persistent under dynamic operation conditions.

In this study, we investigate the reversibility of thin-film $Ni_xFe_{(1-x)}OOH$ composition and activity under reverse polarization when cycled in a multi-metal electrolyte that closely resembles those used in industrial electrolyzer stacks. Stainless steel components were aged both thermally and electrochemically in KOH to produce electrolytes with different extents of corrosion. A thin-film $Ni_xFe_{(1-x)}OOH$ catalyst coated on Pt foil was then subjected to repeated charge–discharge cycling in these electrolytes. Electrode activity was analyzed by quantifying the Ni charge lost and by monitoring the total cell voltage over cycling, while the changes in the surface composition were analyzed via XPS.

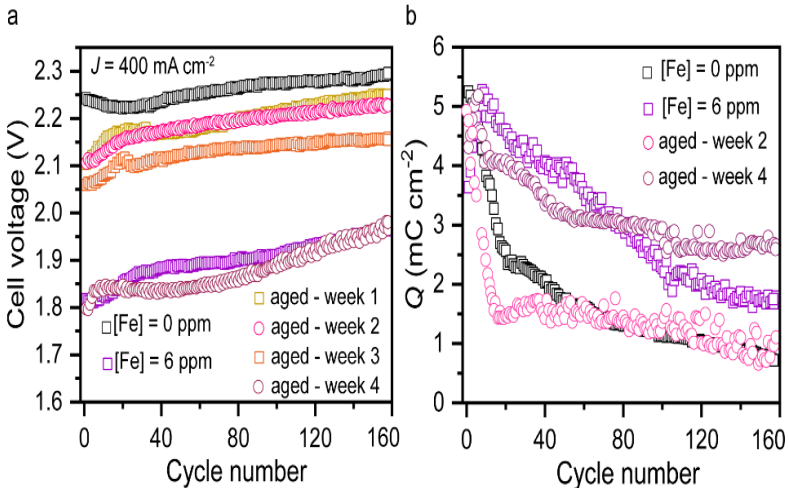


Fig 3.1: **a)** Comparing the effect of electrolyte aging with stainless steel 316 in 30% w/w KOH (thermally aged at 80 °C before analysis) to intentionally Fe-spiked 30% w/w KOH ([Fe] = 0, 6 ppm) on total cell voltage at $J = 400$ mA cm^{-2} for thin film $Ni_xFe_{(1-x)}OOH$ coated on Pt-Ti mesh anode and PGM cathode assembled in a zero-gap cell operated at 80 °C. **b)** Comparing the discharge capacity decay for thin film $Ni_xFe_{(1-x)}OOH$ coated on Pt-Ti mesh in a zero-gap cell with 30% w/w KOH (thermally aged with stainless-steel 316 for week 2 and week 4) to intentionally Fe-spiked 30% w/w KOH ([Fe] = 0, 6 ppm). The electrode was charged at 400 mA cm^{-2} and discharged at a constant current of –0.1 mA cm^{-2} to 0.7 V vs RHE

Figure 3.1a compares the electrochemical behavior of thin-film NixFe(1-x)OOH coated on Pt-Ti mesh when operated in KOH with intentionally controlled Fe concentration to electrolyte thermally aged with stainless steel 316. The total cell voltage at 400 mA cm^{-2} showed a strong dependence on the extent of electrolyte aging. The unspiked electrolyte ([Fe] = 0 ppm) exhibited the maximum voltage, with a gradual increase of ~60 mV after 160 charge-discharge cycles. The addition of 6 ppm dissolved Fe substantially decreased the cell voltage by ~280 mV, consistent with prior studies showing that Fe incorporation into NiOOH lowers the OER overpotential.[66] The electrolytes aged with stainless steel showed differences in cell voltage as a function of aging time. At cycle 1, the week-1 and

week-2 electrolytes showed an initial cell voltage of 2.1 V, which rapidly increased to 2.18 V in the next 20 cycles, followed by a gradual increase of ~20 mV in the next 140 cycles. In contrast, the electrode cycled in the week-4 aged electrolyte showed an identical cell voltage to KOH with [Fe] = 6 ppm at cycle 1, but the cell voltage increased more rapidly over the next 40 cycles (~2.5 mV/cycle).

The discharge capacity is a measure of the number of active Ni sites on the electrode surface. For all electrolyte compositions, the discharge capacity decayed over cycling, but with differences in the rate of decay (Figure 3.1b). We compare the decay profiles of the week-2 and week-4 aged KOH samples, as they showed the maximum differences among the samples cycled in aged KOH. The week-2 aged sample showed an initial charge density of ~4 mC cm^{-2}, which rapidly declined in the first 20 cycles by ~62%. After cycle 50, both the week-2 aged sample and the electrode cycled in Fe-free KOH exhibited an identical decay profile. The 6-ppm Fe-spiked sample showed better charge retention compared to the Fe-free system with a lower decay rate of 25 μC/cycle. The week-4 aged sample showed a similar decay rate to the [Fe] = 6 ppm sample in the first 50 cycles but subsequently plateaued near 2.5 mC cm^{-2}, resulting in the best charge retention among all electrolytes tested.

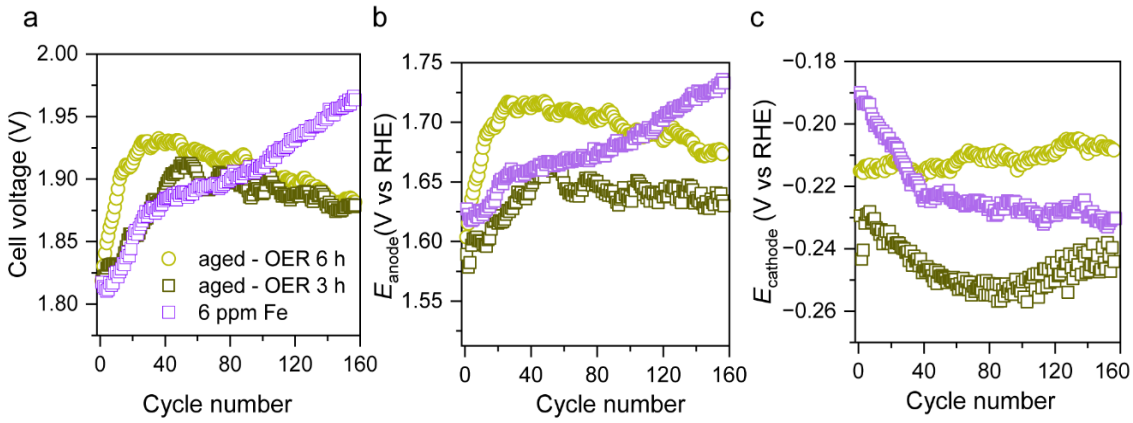


Figure 3.2: **a)** Comparing the effect of electrolyte aging with stainless steel 316 in 30% w/w KOH (aged by applying a J = 250 mA cm^{-2} for at 80 °C before analysis) to intentionally Fe-spiked 30% w/w KOH ([Fe] = 0, 6 ppm) on total cell voltage at J = 400 mA cm^{-2} for thin film $Ni_xFe_{(1-x)}OOH$ coated on Pt-Ti mesh anode and PGM cathode assembled in a zero-gap cell operated at 80 °C. **b)** Anode potential vs RHE as a function of cycle number for electrodes cycled in aged KOH and 30% w/w KOH containing [Fe]= 6 ppm at 80 °C.**)** Cathode potential vs RHE as a function of cycle number for electrodes cycled in aged KOH and 30% w/w KOH containing [Fe]= 6 ppm at 80 °C.

To accelerate the aging process, stainless steel 316 was oxidized in 30% w/w KOH at 80 °C for 3 h and 6 h by applying a current density of J = 250 mA cm^{-2}, and the samples cycled are referred to as aged-OER 3 h and aged-OER 6 h. The detailed procedure for the aging process is included in the methods section. The total cell voltage behavior showed significant differences for $Ni_xFe_{(1-x)}OOH$ samples operated in aged-OER electrolytes compared to the intentionally Fe-spiked electrolyte (Figure 3.2a). All systems showed a similar low voltage between 1.82–1.84 V at cycle 1, followed by a sudden increase of ~100 mV in the first 40 cycles. The aged-OER 6 h sample showed a more rapid increase within the first 30–40 cycles, followed by a gradual decrease over the next 150 cycles at a rate of –0.5 mV/cycle. In contrast, the system with 6 ppm dissolved Fe showed a consistent increase in the cell voltage throughout the experiment despite its lower initial activity.

The trends in the total cell voltage are substantially influenced by the anode. In the 3 h aged KOH, the anode potential increased from approximately 1.59 to 1.65 V during the first 40 cycles and subsequently remained relatively stable at approximately 1.63–1.65 V (Figure 3.2b). The anode potential in the 6 h aged KOH increased more rapidly, reaching approximately 1.71–1.72 V before gradually decreasing to approximately 1.67 V by the end of cycling. By comparison, the anode potential in the [Fe] = 6 ppm electrolyte increased continuously from approximately 1.62 to 1.74 V.

In general, the cathode potential showed minimal fluctuation (~60 mV) in comparison to the changes in the anodic potential. For the aged-OER 3 h sample, the cathode potential shifted from –0.23 to –0.25 V vs. RHE in the initial 60 cycles and then gradually stabilized around -0.24 V vs. RHE. The system containing 6 ppm dissolved Fe showed a continuous rise in the cathodic potential (~40 mV) over 160 cycles. In contrast, the aged-OER 6 h sample maintained a constant cathodic potential near -0.21 V vs. RHE.

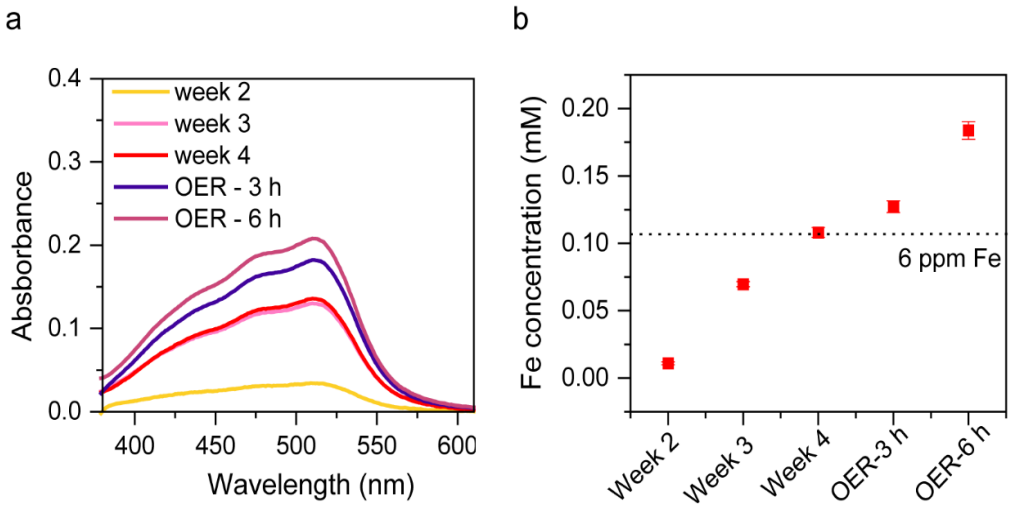


Figure 3.3: a) Quantification of dissolved Fe in the electrolyte via UV-Vis spectroscopy for 30% w/w KOH thermally aged at 80C with stainless steel-316 for 2,3,4 weeks and 30% w/wKOH aged electrochemically by oxidizing stainless steel-316 at $J = 250$ mA cm^{-2} for 3 h and 6 h. **b)** Dissolved Fe concentration in Mm from UV-Vis quantification for different aged KOH samples. The error bars are collected from three independent measurements.

The extent of corrosion was tracked by quantifying the amount of dissolved Fe in the electrolyte for different aging techniques. Dissolved Fe in the electrolyte was reduced to Fe^{2+} species using hydroxylamine hydrochloride solution as the reducing agent. The free Fe^{2+} species were then complexed with an excess of phenanthroline, and the complex was detected using UV-Visible spectroscopy (Figures C.3–C.4). The UV-Visible spectra showed a broad absorbance peak in the visible region near 510 to 520 nm. From **Figure 3.3a**, week-2 aged KOH showed the weakest absorbance, whereas a substantially higher absorbance was observed after aging for 3 and 4 weeks. Electrochemical aging showed the strongest absorbance, indicating the highest amount of dissolved Fe being present in the system.

Quantification of the UV-vis measurements showed that the dissolved Fe concentration increased from approximately 0.01 mM after 2 weeks of thermal aging to approximately 0.07 mM after 3 weeks and 0.11 mM after 4 weeks (Figure 3.3b). The week-4 electrolyte therefore contained a Fe concentration comparable to the intentionally added 6 ppm Fe, corresponding to approximately 0.11 mM. Electrochemical aging resulted in higher dissolved Fe concentrations, reaching approximately 0.13 mM after 3 h and 0.18 mM after 6 h of operation. Together, these results confirm that stainless steel 316 in contact with 30% w/w KOH can act as a source for dissolved Fe, and the amount of dissolved Fe strongly depends on factors like electrolyte temperature, time of contact, and the presence of dissolved gases.

Table 3.1 Surface composition (atomic %) of $Ni_xFe_{(1-x)}OOH$ in aged KOH using XPS.

Electrode	Thin film $Ni_xFe_{(1-x)}OOH$ on Pt foil				
	6 ppm Fe	Aged week 2	Aged week 4	Aged week 5	3 h OER at 250 mA cm^{-2}
Fe	1.9	0.13	2.43	2.93	3.30
Ni	29	41.10	28.77	27.59	26.08
O	68	58.77	67.77	66.15	66.29
Cr	-	-	0.51	0.53	0.69
Mn	-	-	1.15	2.80	3.64

To study the changes in the surface composition of $Ni_xFe_{(1-x)}OOH$, a thin layer catalyst was coated on Pt foil. The electrode was oxidized by holding at 1.55 V vs RHE for 15 min in aged (both thermally and electrochemically oxidized) 30% w/w KOH at 80 °C

and also 6 ppm Fe-spiked 30% w/w KOH at 80 °C. **Table 3.1** shows that changes in the surface composition are strongly related to the electrolyte aging conditions. The electrode oxidized in 6-ppm Fe-containing electrolyte exhibited a surface Fe content of 1.9 atomic %. Week-2 aged KOH has a lower surface Fe content; however, the Fe at% was increased substantially with further aging. The highest surface Fe content (3.3 at %) was measured when the electrode was oxidized in electrolyte after electrochemical oxidation of stainless steel-316 at J = 250 mA cm^{-2} for 3 h. Along with an increase in the surface Fe content, there is a progressive increase in the values of Cr and Mn on the catalyst surface from week 4-

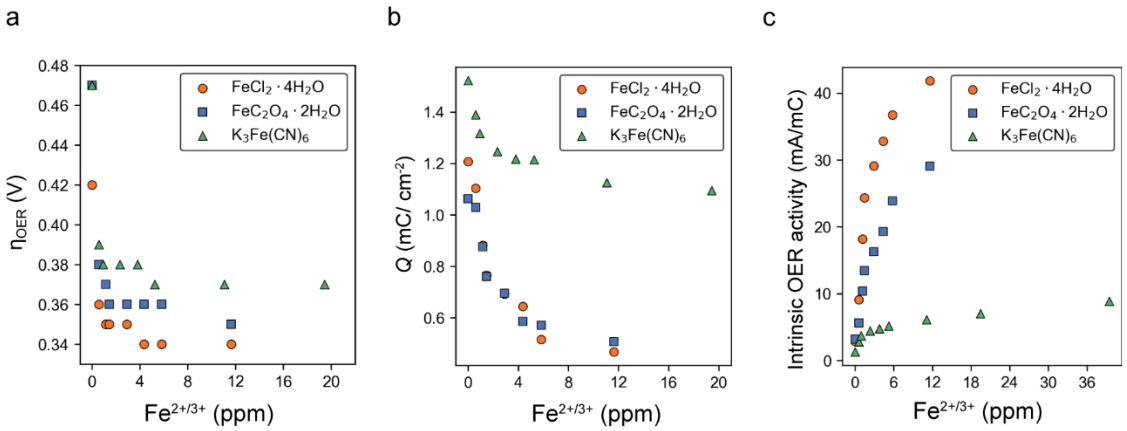


Figure 3.4: Effect of dissolved iron on the OER activity of thin-film $Ni_xFe_{(1-x)}OOH$ as a function of Fe precursor complex. Fe was introduced into 30% w/w KOH from 1 mM precursor solutions of $FeCl_2$. $4H_2O$, FeC_2O_4. $2H_2O$ and $K_3Fe(CN)_6$. **a)** The OER overpotential measured at $J = 10$ mA cm^{-2} at different Fe concentrations **b)** Ni2+/3+ redox charge integrated from cyclic voltammetry collected at 50 mV s^{-1} in 30% w/w KOH at 80 °C as a function of [Fe]. **c)** Intrinsic OER activity calculated by normalizing the OER current at 1.55 V vs RHE to the charge passed by integrating the Ni^{3+} reduction peak from 1.1 to 1.3 V vs RHE

aged samples onwards. The surface Mn composition has increased from 1.15 to 3.64 going from the week 4-aged sample to the aged-OER 3 h sample.

Thin-film $Ni_xFe_{(1-x)}OOH$ operated in aged electrolyte solution with stainless steel showed variable electrochemical response even with comparable dissolved Fe content. To determine whether these differences in activity could arise from the differences in chemical structure of the precursor solution or to understand the availability of dissolved Fe as a function of precursor solution, we studied the OER activity of thin-film $Ni_xFe_{(1-x)}OOH$ using three precursor solutions: $FeCl_2.\ 4H_2O$, $FeC_2O_4.\ 2H_2O$ and $K_3Fe(CN)_6$. The OER overpotential measured at 10 mA cm^{-2} decreased with increasing Fe concentration from 0 to 20 ppm for all three precursor solutions **(Figure 3.4 a)**. $FeCl_2.\ 4H_2O$ showed the maximum activity, achieving an OER overpotential approximately 340 mV lower compared to the other two solutions. The $Ni^{2+/3+}$redox charge decreased with increasing Fe concentration for the chloride- and oxalate-based precursors. For both precursors, Qdecreased from approximately 1.1 mC cm^{-2} at low Fe concentrations to approximately 0.5 mC cm^{-2} at 12 ppm Fe. **(Figure 3.4 b)**

Correspondingly, the intrinsic OER activity increased most strongly for $FeCl_2.\ 4H_2O$, reaching approximately 42 mA mC^{-1}, followed by $FeC_2O_4.\ 2H_2O$ at approximately 29 mA mC^{-1}. $K_3Fe(CN)_6$ produced only a modest increase, with intrinsic activity remaining below approximately 10 mA mC^{-1}**(Figure 3.4 c).** These results show that both OER activity and Ni redox-charge retention varied with the Fe precursor used, even at comparable nominal Fe concentrations.

Discussion

Aging 30% w/w KOH in stainless steel 316 progressively altered the electrolyte composition by introducing dissolved metal species such as Fe, Cr, and Mn, which

eventually changed the surface composition of the thin-film $Ni_xFe_{(1-x)}OOH$ catalyst **(Table 3.1).**

Effect of dissolved metal impurities

As the aging proceeds, dissolved Fe becomes increasingly available, as quantified by UV-Vis spectroscopy **(Figure 3.3)**, while Cr and Mn also emerge as corrosion-derived metallic impurities. This shows that catalyst evolution in a realistic electrolyte system cannot be fully studied by changing the Fe concentration alone; instead, a combination of mixed metal impurities needs to be considered. The overall increase in total OER activity from week-2-aged to week-4-aged KOH strongly indicates the role of Fe incorporation into the catalyst, forming $Ni_xFe_{(1-x)}OOH$. However, the differences in the cell voltage decay trend could be related to interactions of the catalyst layer with the dissolved metals in the electrolyte.

We further investigated the aged-OER 3 h sample as it provides a useful example of this more complex multi-metal ion interaction with the NiOOH catalyst layer. For the aged-OER 3 h sample, during charge-discharge analysis, the anode potential increased from 1.58 to 1.65 V over the first 40 cycles; however, the electrode maintained a relatively stable OER activity at ~1.65 to 1.68 V during the remaining 100+ cycles **(Figure 3.2)**. Comparing the cyclic voltammograms after cycle 50 to cycle 1 (Figure C.2), the shift in the Ni^{3+}/Ni^{2+} reduction peak indicates that the local electronic environment of the Ni sites changes between the 6-ppm Fe and aged-electrolyte conditions, consistent with differences in Fe incorporation. Fe^{3+} in the lattice withdraws electron density from Ni, making the Ni^{2+} to Ni^{3+} oxidation less favorable and shifting it in the anodic direction.[40] However, this modification was not accompanied by a loss in OER activity. This suggests that the change

in the electrochemically observable $Ni^{2+/3+}$ transition reflects the population and environment of redox-active Ni sites, whereas the OER activity depends on a smaller subset of catalytically active sites. The shift in the cyclic voltammograms could be correlated to the incorporation of Cr into the $Ni_xFe_{(1-x)}OOH$ lattice, where it perturbed the Ni oxidation energetics without blocking the active Ni-Fe synergistic sites responsible for improved OER activity. The compositional changes following charge–discharge cycling further suggest that the incorporated Fe, Cr, and Mn species are not permanently fixed within the catalyst. Their partial removal during cycling indicates that the anode surface remains dynamic and responds to changes in potential. This reversibility may help explain why substantial changes in surface composition and Ni redox behavior can occur without an immediate deterioration in OER performance. These hypotheses should be further evaluated using controlled single-impurity experiments with spectroscopic evidence to distinguish the effects of individual metal ions on catalyst activity.

Materials and methods:

Materials: Nickel(II) nitrate hexahydrate, $Ni(NO_3)_2{\cdot}6H_2O$ (99.99%), iron (II) chloride tetrahydrate, FeCl2 · 4H2O (> 99%), iron(II) oxalate dihydrate, FeC_2O_4. $2H_2O$ (> 99%) and Potassium hexacyanoferrate (III), $K_3[Fe(CN)_6]$ (> 99%) were purchased from Sigma Aldrich. The stainless steel-316 shim stock was purchased from McMaster Carr, and Ni-mesh (99.7% metal basis) was purchased from Fuel Cell Materials.

Aging of potassium hydroxide at elevated temperatures: A 5 × 5 cm^2 stainless steel 316 mesh was immersed in 100 mL of 30% w/w KOH at 80°C in air. For all aging studies, the

surface area-to-volume ratio was kept at 0.25 cm^2/mL. The electrolyte is denoted as "*aged KOH- X*", where X represents the duration of the aging process.

Electrochemical aging of KOH: A 5× 5 cm^2 stainless steel-316 was galvanostatically biased at 250 mA cm^{-2} in a two-electrode cell containing 100 mL of 30% w/w KOH at 80°C. A 30 cm^{-2} Ni mesh was used as the counter electrode. After the cell was operated for 3 h and 6 h, the electrolyte was cooled and used for electrochemical testing.

Charge-discharge analysis: All electrodes were "charged" at 400 mA cm^{-2} towards the OER for 1.0 min in the aged electrolyte in a zero-gap arrangement with a PGM-containing cathode serving as the counter electrode and a reversible hydrogen electrode (RHE, Gaskatel Hydroflex) as the reference electrode. Electrodes were galvanostatically "discharged" at a constant rate, J– (–0.1 mA cm^{-2}), to 0.700 vs RHE. Together, these charging and discharging steps constitute a single "cycle".

UV-Vis spectroscopy: A 1.00 mL aliquot of Fe-containing solution in 30% w/w KOH was diluted and acidified to pH 3-4 using 3 M hydrochloric acid. Three drops of 10% hydroxylamine hydrochloride were added to reduce Fe^{3+} to Fe^{2+}. 600 µL of 70 mM 1,10-phenanthroline was added as the complexing agent. The solution was diluted to a final volume of 5.00 mL using deionized water, giving a final phenanthroline concentration of 8.4 mM. The solution was kept aside for 2 minutes to fully develop the bright red color, indicating the completion of the Fe-phenanthroline complex.

X-ray photoelectron spectroscopy (XPS): XPS measurements were conducted using a Thermo-Scientific ESCALAB 250 instrument calibrated with Au 4f7/2, Ag 3d5/2, and Cu 2p3/2. A Mg–Kα X-ray source was powered at 200 W, with 50 eV pass energy, and an

energy resolution of approximately 0.1 eV. A low-energy electron flood source was used for charge neutralization during all high-resolution measurements. The analysis chamber pressure was maintained below 1.0×10^{-7} mbar, and the analyzer pressure was below 1.0×10^{-8} mbar. The sample was oxidized by holding at 1.6 V vs RHE for 15 minutes and recorded the “before” XPS spectra. The “after” spectra were recorded after finishing 100 charge-discharge cycles.

APPENDIX I

Chapter I: Supporting Information

Charge integration:

The charge integration from cyclic voltammograms was performed using the Bio-logic EC-lab software (V 11.50). The baseline was fitted using a linear model by selecting the regions of the voltammogram outside the faradaic peak to represent the background current. Anode peaks were integrated over a potential range of 1.1–1.25 V vs RHE, which is associated with Ni^{2+} to Ni^{3+} transitions in the $Ni(OH)_2$/NiOOH coating. The integrated charge at the cathode was measured over a potential range of 0.28–0.05 V vs RHE, which is associated with the adsorption of hydrogen on the surface of platinum-group metals

Table A.1: Atom % of uncoated Ni mesh calculated from XPS analysis.

Name	Peak binding energy (eV)	Atom %
Ni 2p	855.0	98.98
Cl 2p	199.8	0.74
Si 2p	102.2	0.28

Table A.2**:** HER and OER overpotential at $|J|$ = 50 mA cm^{-2} for NiCo-PGM cell during the addition of $[Cl^-]$ at similar concentrations to what was formed during $FeCl_2 \cdot 4H_2O$ spiking.

	$\lvert\eta_{50\ mA}\rvert$ (mV)		
Electrode	0 mM Cl^-	0.2 mM Cl^-	0.8 mM Cl^-
NiCo	330	329	340
PGM	60	61	59

Table A.3: Atom % calculated from XPS analysis.

	Atomic %			
Elements	Pristine	[Fe] = 0 ppm	6 ppm	24 ppm
Co2p	15.1	17.1	9.5	17.5
$Fe2p_{3/2}$	NA	NA	1.1	2.6
$Ni2p_{3/2}$	15.2	16.5	19.4	4.6
O1s	69.7	66.3	70.0	75.3

Table A.4: The peak intensity ratio of Ni-O vibrations at 474–477 cm^{-1} and 549–555 cm^{-1} from in situ Raman spectroscopy of a NiCo electrode. The corresponding peak positions are given in brackets.

Potential (V vs RHE)	[Fe] ppm	Peak intensity 1 (P1)	Peak intensity 2 (P2)	P1/P2
1.23	0	420 (474 cm^{-1})	285 (555 cm^{-1})	1.47
	6	4453 (473.7 cm^{-1})	3938 (551cm^{-1})	1.13
	24	1609 (475 cm^{-1})	1148 (549 cm^{-1})	1.42
1.38	0	3245 (475.7 cm^{-1})	2233 (554 cm^{-1})	1.45
	6	8218 (477cm^{-1})	6217 (551 cm^{-1})	1.32
	24	4368 (476.5cm^{-1})	3145 (552 cm^{-1})	1.38

Chapter I: Supporting Figures

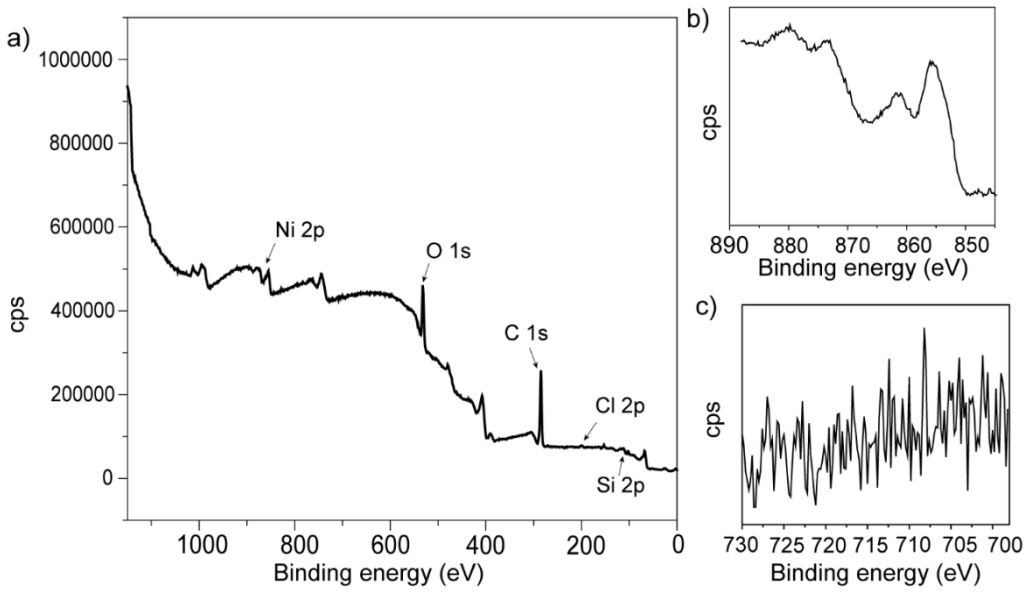


Figure A.1: (a) XPS survey spectrum of uncoated Ni mesh (b) High-resolution XPS of Ni 2p region **(c)** Fe 2p region.

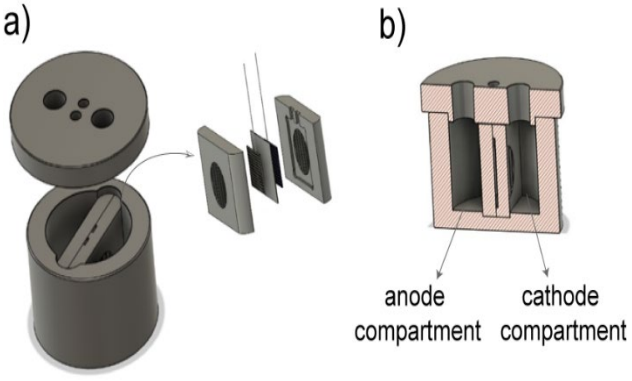


Figure A.2: (a) Diagram of the model zero-gap cell showing the electrode-separator assembly (b) cross-section image of the zero-gap cell showing the anode and cathode compartments.

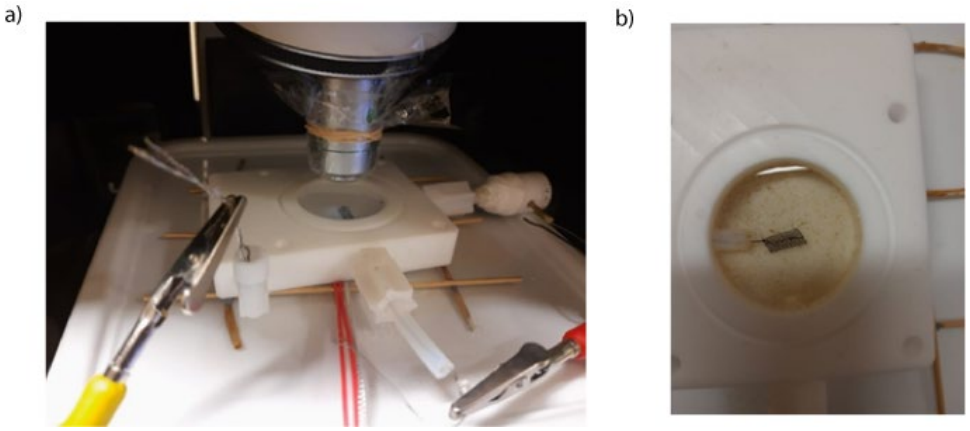


Figure A.3: (a) Digital photograph of the cell used for in situ Raman spectroscopy. (b) Digital photograph of the electrolyte after testing revealing visible precipitation of presumed Fe (III) oxide particles when 30% w/w KOH was spiked with $FeCl_2 \cdot 4H_2O$ solution at [Fe] = 24 ppm.

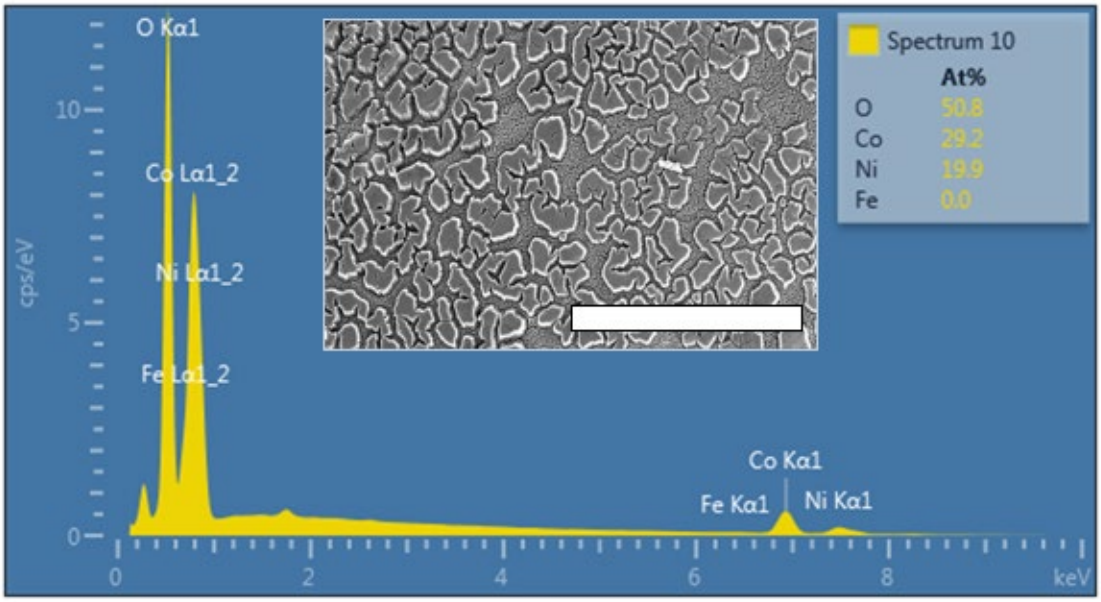


Figure A.4: EDX spectrum of a NiCo anode formed via five sequential cathodic depositions at –100 mA cm^{-2} for 1 min each followed by thermal annealing at 400 °C for 15 min each cycle in air. Inset SEM image shows the sampled region. The scale bar represents 30 μm.

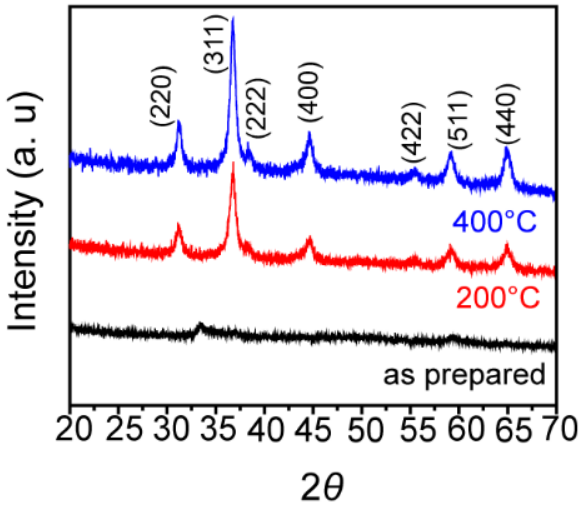


Figure A.5: Powder XRD pattern of NiCo electrode annealed at different temperatures (T= 200–400 °C) consistent with a $Ni_zCo_{(1-z)}O_x$ spinel structure.

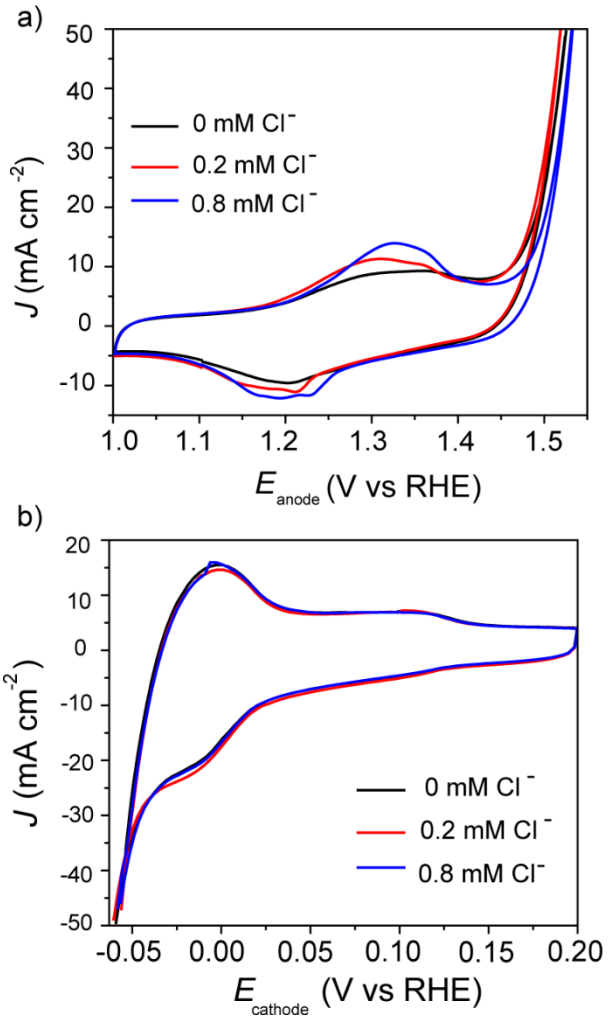


Figure A.6: Cyclic voltammograms collected with a (a) NiCo anode, a (b) PGM anode after 60 min of conditioning in 30% w/w KOH at 80 °C at 250 mA cm^{-2} in a zero-gap cell and then cycled in three different [Cl^-] (as KCl) at v = 20 mV s^{-1}. Data is presented for the second voltammetry cycle.

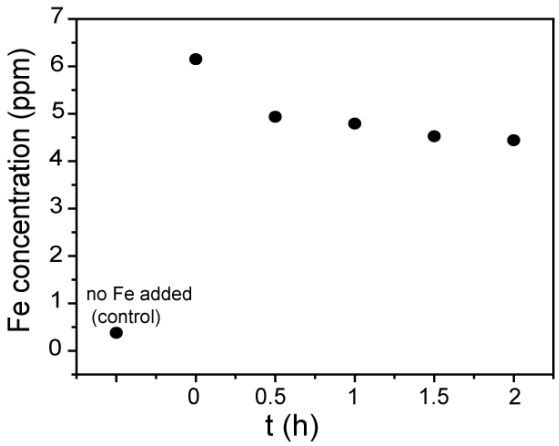


Figure A.7: ICP-MS analysis of anolyte Fe concentration measured at 30 min intervals under constant polarization at $J = 250$ mA/cm², using a NiCo-PGM electrode in a 6 ppm Fe-containing 30% w/w KOH solution at 80 °C. The electrodes were preconditioned in non-Fe containing KOH prior to the analysis.

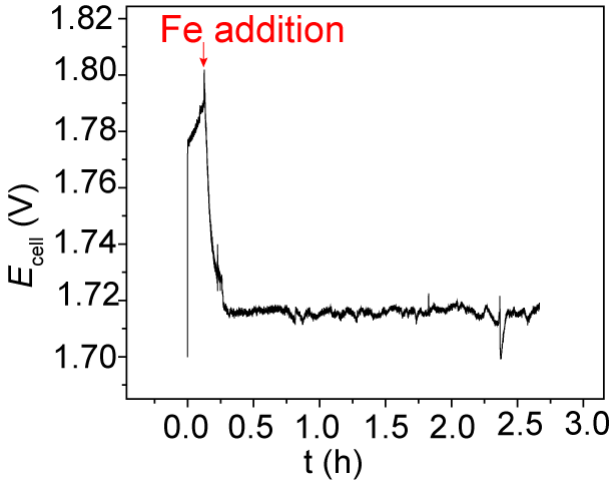


Figure A.8: $E_{cell\ vs}$ time behavior for PGM-NiCo AAWE cell at $J = 250$ mAcm^{-2} in 30% w/w KOH at 80 °C. [Fe] = 6 ppm was added to the cell at $t = 0.25$ h.

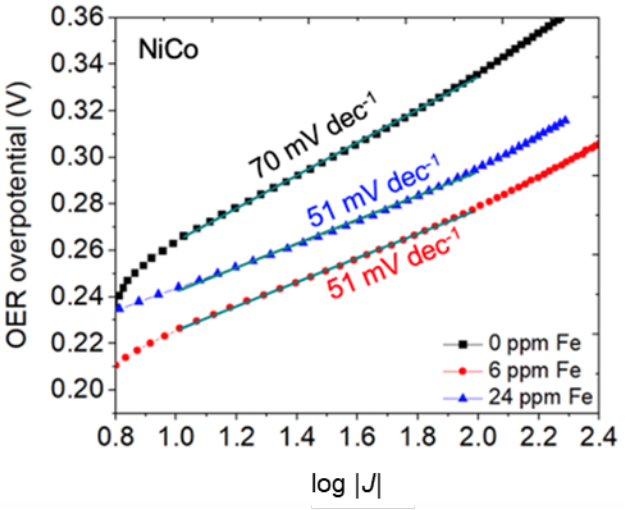


Figure A.9: OER overpotential vs $\log_{10}|J|$, ($\log_{10}|$mA cm$^{-2}|$), of NiCo anodes after 60 min of conditioning at 250 mA cm^{-2} in 30% w/w KOH at 80 °C containing [Fe] = 0 ppm, and then tested in 30% w/w KOH at 80 °C containing [Fe] = 0, 6, or 24 ppm.

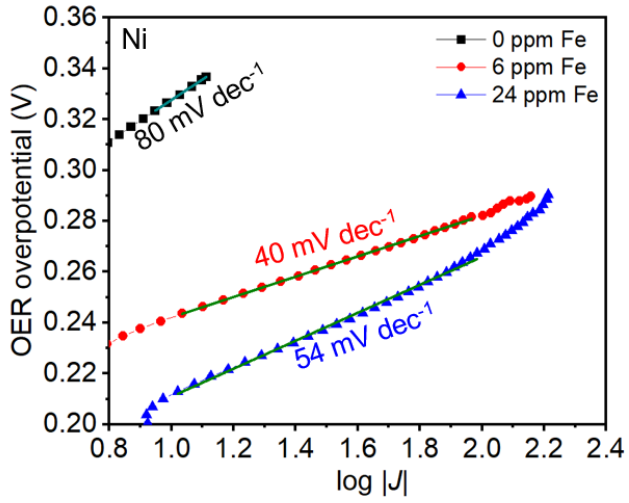


Figure A.10: OER overpotential vs $\log_{10}|J|$, ($\log_{10}|$mA cm$^{-2}|$), of Ni anode after 60 min of conditioning at 250 mA cm^{-2} in 30% w/w KOH at 80 °C containing [Fe] = 0 ppm, and then tested in 30% w/w KOH at 80 °C containing [Fe] = 0, 6, or 24 ppm.

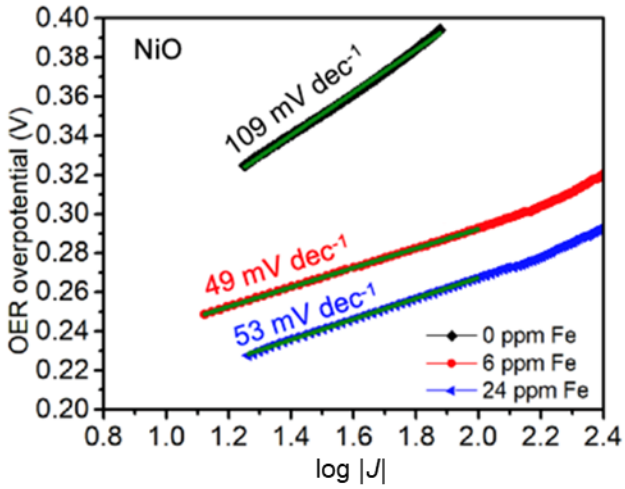


Figure A.11: OER overpotential vs $\log_{10}|J|$, ($\log_{10}|$mA cm$^{-2}|$), of NiO anode after 60 min of conditioning at 250 mA cm^{-2} in 30% w/w KOH at 80 °C containing [Fe] = 0 ppm, and then tested in 30% w/w KOH at 80 °C containing [Fe] = 0, 6, or 24 ppm.

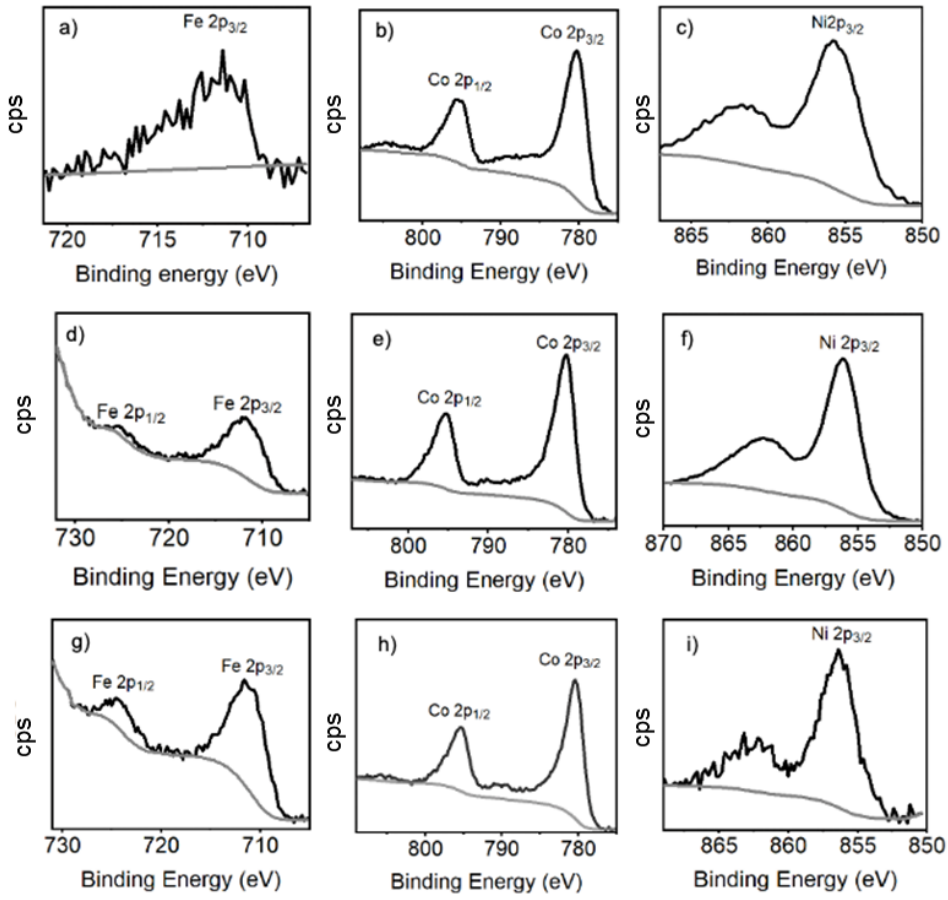


Figure A.12: High-resolution XPS of the Fe $2p_{3/2}$ (a,d,g), Co $2p_{3/2}$ (b,e,h), and Ni $2p_{3/2}$ (c,f,i) regions of a NiCo anode tested in 30% w/w KOH at 80 °C containing [Fe] = 0 (a-c), 6 (d-f), and 24 ppm (g-i).

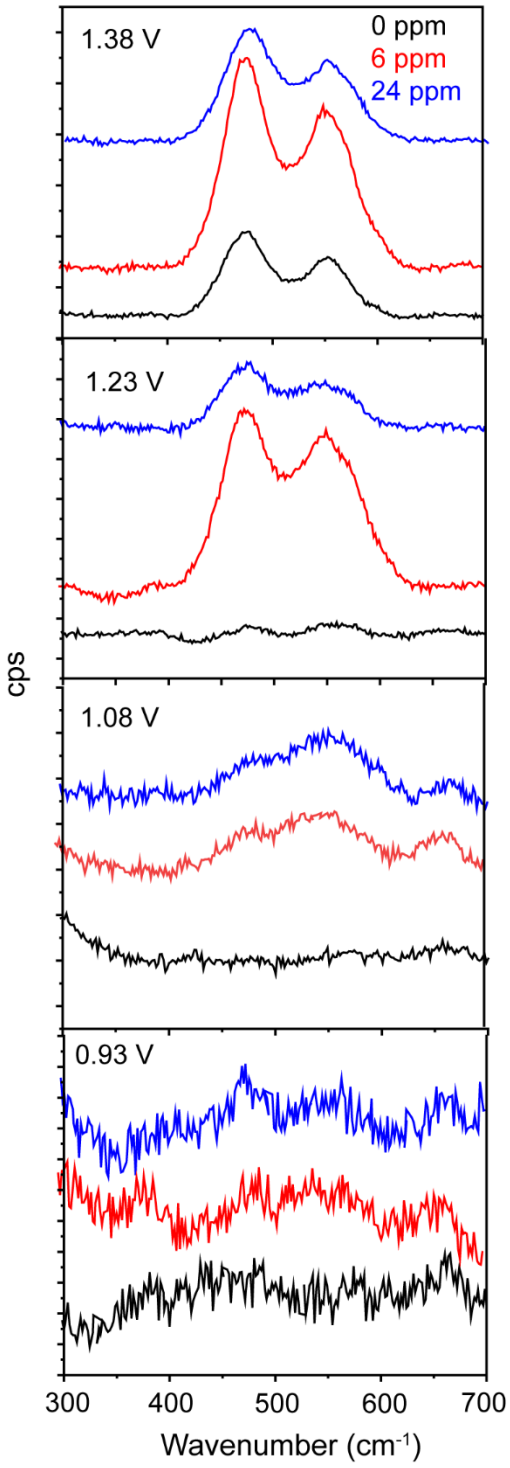


Figure A.13: In situ Raman spectra of NiCo electrode in 30% w/w KOH at 60 °C recorded at 0.93 V, 1.08 V 1.23 V, and 1.38 V vs RHE.

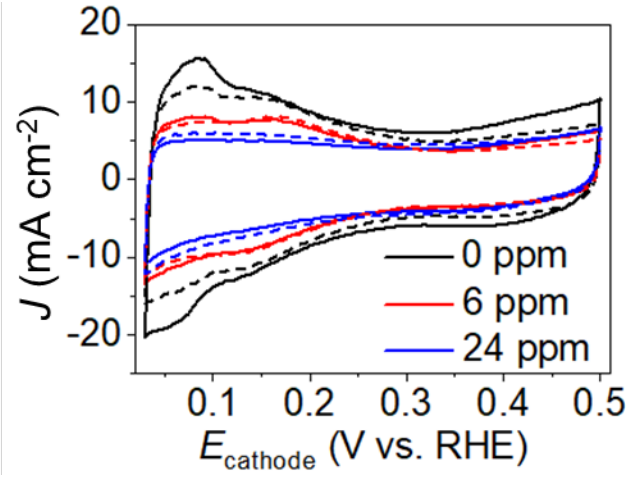


Figure A.14: Cyclic voltammetry for a PGM cathode cycled from $0.05 < E_{cathode} < 0.5$ V vs. RHE at 100 mV s^{-1} in 30% w/w KOH at 80 °C with [Fe] = 0 ppm (black), 6 ppm (red), 24 ppm (blue). Solid lines represent the third cycle and dashed lines represent the 100^{th} cycle.

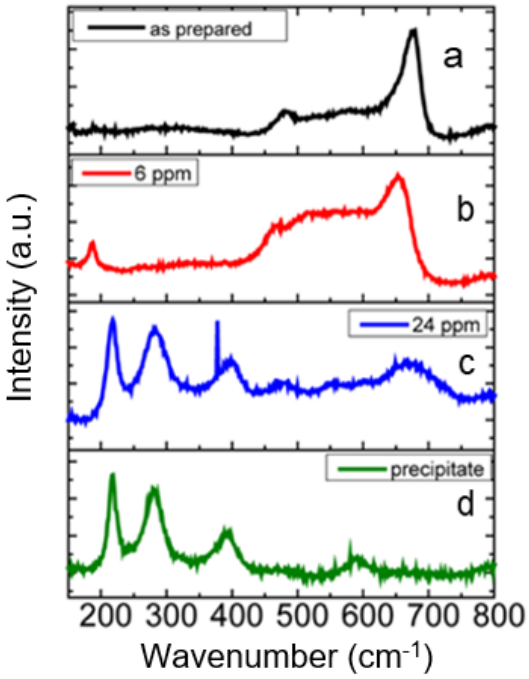


Figure A.15: Comparison of ex situ Raman spectra of NiCo anodes before (a) and after testing in KOH containing [Fe] = 6 (b) and 24 ppm (c). Fe precipitate was collected from electrolyte at [Fe] > 24 ppm (d) Ex situ Raman spectrum of pristine NiCo anode at different [Fe] compared to precipitate from the electrolyte.

APPENDIX II

Chapter II Supplemental Information

Zero-gap cell assembly:

A single-cell zero-gap study was conducted in a Teflon coin cell where the electrodes and separator were assembled between two polyether ether ketone (PEEK) plates **(Figure B.2)**. The cell contained 20 mL of 30 w/w % KOH at 80 °C. A reversible hydrogen electrode was inserted into the anode compartment to collect 3-electrode measurements of the anode potential. The temperature was monitored with a probe inserted into the electrolyte compartment. A syringe pump replaced water lost to electrolysis and evaporation at an empirically determined rate of 46 μL h^{-1}. The electrolyte in both anode and cathode compartments was stirred to maintain a constant KOH concentration throughout the experiment.

Raman analysis of catalyst reconstruction:

Changes in the lattice vibrations led to variable Raman spectra which were ascribed to structural changes in the lattice occurring during conversion **(Figure 2.4d and Figure B.7)**. During discharge, the ordered oxyhydroxide layers are believed to contract, and the collapse of the layered framework to yield a single disordered $Ni_xFe_{(1-x)}(OH)_2$ phase was evident in the *in-situ* Raman spectra collected in the presence of Fe **(Figure B.7)**.[63] Layered oxyhydroxides exhibit higher resistance towards chemical dissolution compared to the associated hydroxide phase, primarily due to stronger M^{3+}-O bonds and lattice stabilization via interlayer H-bonds and the presence of octahedrally coordinated Fe in the lattice structure.[71] Based on the XPS results **(Figure 2.4a–c)** and Raman analysis **(Figure B.5b)** changes in the ratio of the Ni(III)-O bending (A_{1g}) to stretching (E_g) peak areas were correlated with changes in the catalyst Fe content **(Figure B.5b)**.[72,89] In this way, changes to the catalyst were monitored without removal of the electrode from the operational environment.

Table B.1: Prior literature on reverse current effects in alkaline water electrolysis

Electrode/material, KOH concentration, and temperature	Reverse-current simulation	$Ni(OH)_2$/NiOOH -related findings	Fe-related findings	Ref.
Anode: $NiCo_2O_4$- or Co_3O_4-coated Ni plate; cathode: Pt plate; electrolyte: 1 M KOH; temperature: 25 °C; cell configuration: three-electrode electrochemical cell with Hg/HgO reference electrode.	Charging at 0.5 mA mg^{-1} and discharging at -0.5 mA mg^{-1} to a cut off potential of 0.5 V	Ni-containing oxides showed larger discharge capacity; $NiCo_2O_4$ capacity increased due to dissolution/recrystallization into metal hydroxide species.	KOH with <5 ppm Fe. Fe was not detected by SEM–EDX before or after electrochemical testing. Fe dissolution was not quantified.	[52]
Anode: Ni mesh coated with $NiCoO_x$ or $LiNiO_x$ catalyst layer; cathode: Ni mesh coated with Ru-Ln oxides electrolyte: 7 M KOH; temperature: 30–80 °C; cell configuration: four-cell bipolar-type stack. Electrode area 27.8 cm^2.	Charging at 0.4–0.6 A cm^{-2} Stack shutdown with and without recirculation and purging. Initial reverse currents up to 24 mA.	Redox reactions in catalyst layers, rather than oxygen reduction, are the dominant source of reverse currents. The magnitude of the reverse current increases with operating temperature.	Dissolved Fe concentration was not controlled	[29]
Anode: $NiCoO_x$-coated Ni mesh; cathode: spiral Ni wire enclosed in a Zirfon separator; electrolyte: 7 M KOH;	Charging at 0.6 A cm^{-2} Discharging with a potential sweep to cutoff potential (0.3, 0.5 and 0.7 V vs	$NiCoO_x$/Ni degraded during discharging steps, higher E_{min} and longer discharging steps increased degradation.	Dissolved Fe concentration was not controlled	[90]

temperature: 25 °C during accelerated durability testing and 80 °C during electrochemical pretreatment; cell configuration: two-electrode alkaline water electrolysis cell.	RHE) followed by potential hold			
Anode: hybrid cobalt-hydroxide nanosheets on Ni wire; cathode: Ni wire; electrolyte: 1.0 M KOH containing dispersed cobalt hydroxide; temperature: not specified; cell configuration: three-electrode cell.	CV cycling between 0.5-1.8 V vs RHE at 500 mV s^{-1}	Uncoated Ni degraded under 0.5-1.8 V cycling. Co nanosheets formed a self-repairing protective OER layer on Ni	Dissolved Fe concentration was not controlled	[91]
<u>Film studies</u> Anode: $Ni(OH)_2$, $Co(OH)_2$, $NiCo(OH)_2$, or $NiFe(OH)_2$ films on Ti foil or Au screen-printed electrodes; cathode: Pt wire; electrolyte: 0.1 M KOH; temperature: 20 °C; cell configuration: three-electrode cell with Ag/AgCl reference electrode. <u>Zero-gap studies</u> Anode: Ni gauze or Fe-doped Ni mesh; cathode: Ni gauze;	Reverse current simulation via open circuit potential (OCP) decay	Reverse-current cycling caused incomplete NiOOH re-formation, loss of Ni^{2+}/Ni^{3+} redox features, film thinning/dissolution, and increased charge-transfer resistance.	<10 ppb Fe in 0.1 M KOH for film studies and ~550 ppb Fe impurity in 7 M KOH for zero-gap cell testing; Fe-doped Ni mesh was prepared using 1 mM Fe-spiked KOH. Online ICP-MS showed substantial Fe dissolution from NiFe films, particularly during reoxidation, and ex situ ICP-MS confirmed Fe crossover into the catholyte.	[49]

electrolyte: 7 M KOH; temperature: 50 °C; cell configuration: zero-gap				
Anode: Ni (99.99% w/w), Ni (99.2%), Ni-Fe (90%/10%), Ni-Fe (80%/20%), or Ni-Fe (70%/30%) alloy electrodes; cathode: glassy carbon; electrolyte: 1 M KOH; temperature: room temperature; cell configuration: three-electrode cell.	Electrochemical conditioning by CV between 0.5–1.6 V or –0.35–1.6 V vs RHE at various scan rates and over a varied number of cycles.	Cycling through the Ni redox region promoted activation, and the response depended on the lower potential limit and the number of Ni redox cycles.	1 M KOH containing 10, 120, and 1120 ppb Fe. *In-situ* ICP-OES showed measurable Fe dissolution from $Ni_{70}Fe_{30}$ during conditioning, with Fe concentration increasing from ~116 to ~121 ppb when electrodes were cycled to –0.35 V vs RHE.	[92]

Table B.2. Electrode-specific surface composition of thin-film catalysts. Three separate electrodes were conditioned at 1.600 V vs RHE in 30% w/w KOH containing 6 ppm Fe, reduced at 0.700 V, and reoxidized at 1.600 V. Each potential hold was 30 min to allow complete conversion. XPS spectra were collected after each potential hold, with electrodes rinsed under DI H_2O and dried in an oven set to 60 °C.

	$Ni_xFe_{(1-x)}OOH$			**$Ni_xFe_{(1-x)}(OH)_2$**			**Re-ox $Ni_xFe_{(1-x)}OOH$**		
Sample ID	*1*	*2*	*3*	*1*	*2*	*3*	*1*	*2*	*3*
Element	Atomic %								
Fe	2.8	1.4	1.5	0.7	0.3	0.3	1.7	0.8	0.8
Ni	36.4	29.1	24.1	41.8	32.2	32.5	38.9	24.9	26.2
O	60.8	69.5	74.4	57.5	67.5	67.2	59.4	74.4	73.0
Apparent Fe content (1–*x*)	0.07	0.05	0.06	0.01	0.009	0.009	0.04	0.03	0.03
Average (1–*x*)	0.06 ± 0.01			0.0093 ± 0.0006			0.033 ± 0.006		

Chapter II Supporting Figures

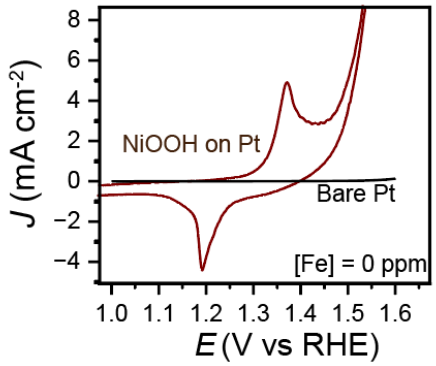


Figure B.1: Voltammetry of anodes with and without catalyst coating. Comparing the cyclic voltammogram of the Pt substrate to NiOOH coated on Pt. The CV was collected in 30 % w/w KOH at 80°C with no added Fe in the medium.

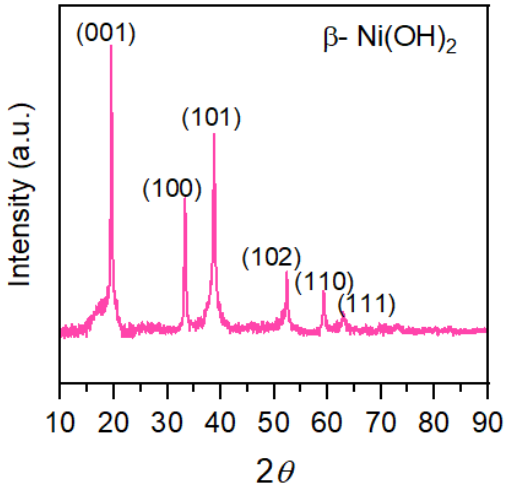


Figure B.2: XRD of $Ni(OH)_2$. $Ni(OH)_2$ was synthesized by precipitating 3.0 M $Ni(NO_3)_2 \cdot 6H_2O$ in 1.0 M KOH.

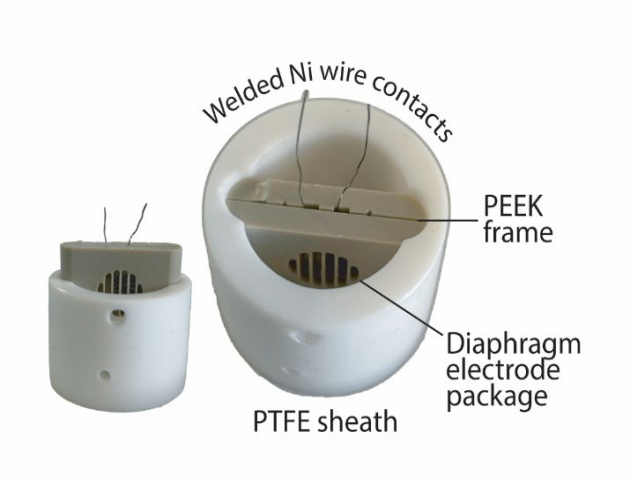


Figure B.3: Image of zero-gap electrolysis cell.



Figure B.4: Image of $Ni(OH)_2$ spiked 30% w/w KOH at 80 °C. A pale green precipitate was assigned to $Ni(OH)_2$.

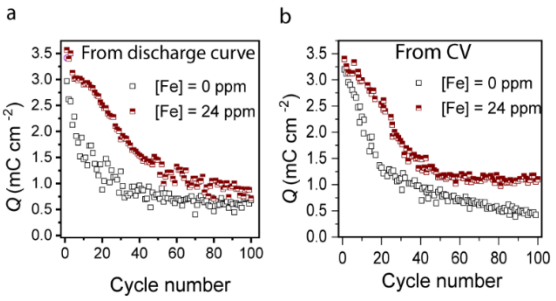


Figure B.5. Discharge capacity versus cycle number for NiOOH coated on Pt foil in 30% w/w KOH with [Fe] = 0 and 24 ppm. The electrodes were charged at 1 A cm^{-2} at 80 °C and discharged at a constant current of –0.1 mA cm^{-2} to a cutoff potential of 0.7 V vs RHE a) cycle dependent charge integrated from the galvanostatic discharge curve in the potential window 1.1 to 1.3 V vs RHE. b) cycle-dependent charge as measured from integrating the $Ni^{2+/3+}$ reduction peak from E = 1.1–1.3 V vs RHE without background subtraction.

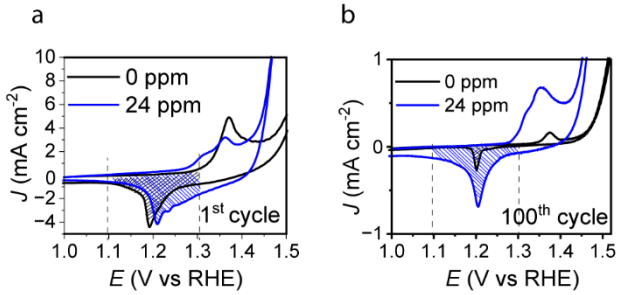


Figure B.6. Cyclic voltammogram of thin-film NiFeOOH on Pt foil cycled in 30 % w/w KOH with [Fe] = 0, 24 ppm after a) one cycle b) one hundred cycles. The CVs were collected after the electrode was charged at 1 A cm^{-2} and discharged at a constant current of –0.1 mA cm^{-2} to 0.7 V vs RHE.

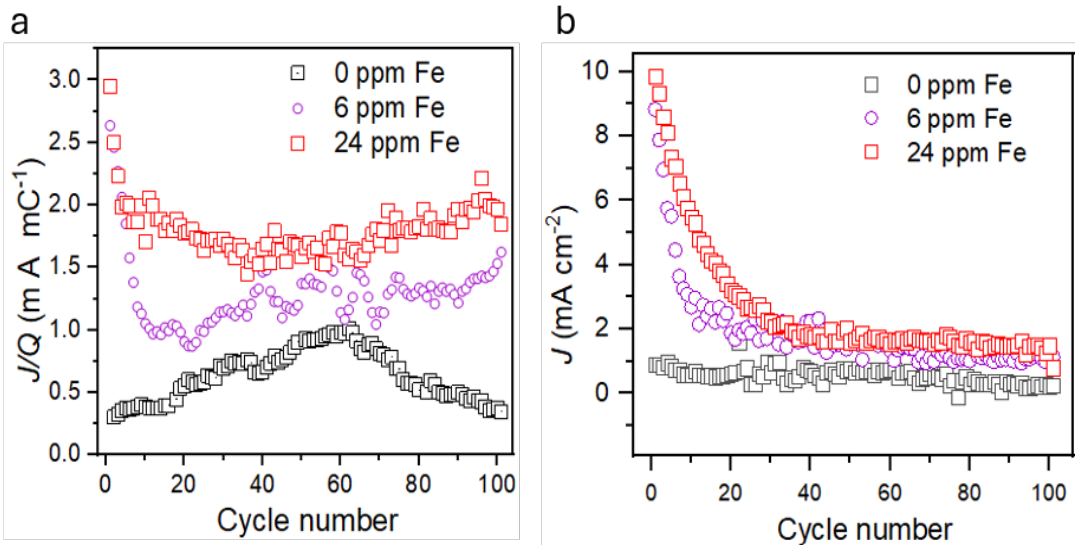


Figure B.7: Normalized activity of thin-film catalysts as a function of Fe content within the electrolyte. a) Intrinsic OER activity at 1.55 V vs RHE for thin film $Ni_xFe_{(1-x)}OOH$ cycled in intentionally Fe spiked ([Fe] = 0, 6, and 24 ppm) 30% w/w KOH at 80 °C, where the electrode was charged at 1.0 A cm^{-2} and discharged at a constant current of –0.1 mA cm^{-2} to 0.700 V b) Current density at E = 1.55V vs RHE for thin film $Ni_xFe_{(1-x)}OOH$ cycled in intentionally Fe spiked ([Fe] = 0, 6, and 24 ppm) 30% w/w KOH at 80 °C, where the electrode was charged at 1.0 A cm^{-2} and discharged at a constant current of –0.1 mA cm^{-2} to 0.700 V

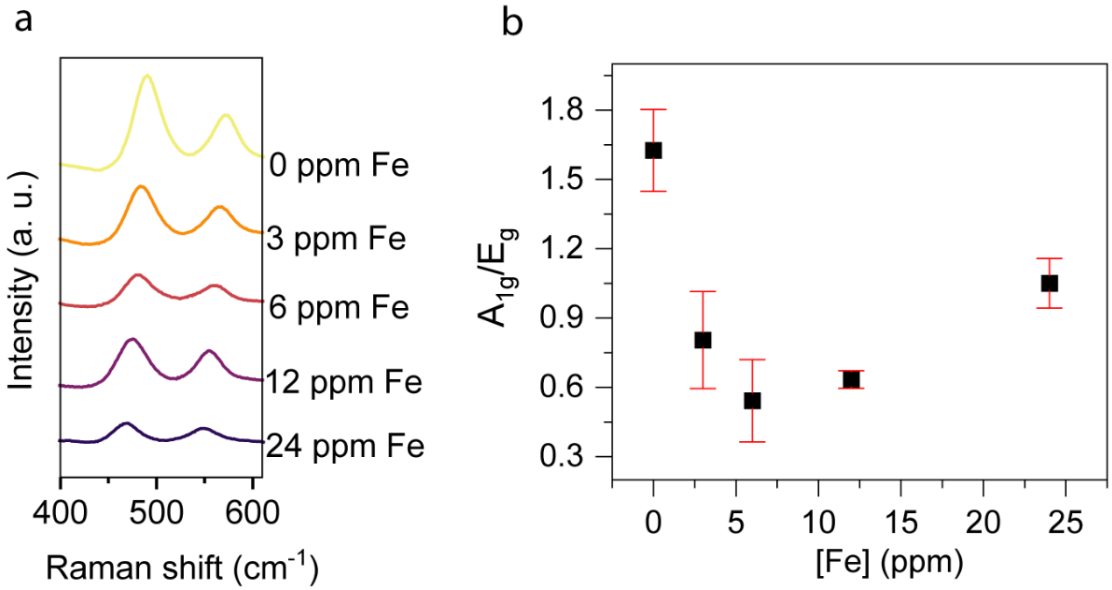


Figure B.8: Raman spectra of NiOOH as a function of dissolved Fe content. a) Ex-situ Raman spectra of NiOOH in 30% w/w KOH at 80 °C at different dissolved Fe concentrations. b) Ratio of the Ni(III)-O bending to stretching peak intensity as a function of dissolved Fe in 30% w/w KOH at 80 °C. The error bars represent one standard deviation from three independent measurements at each Fe concentration.

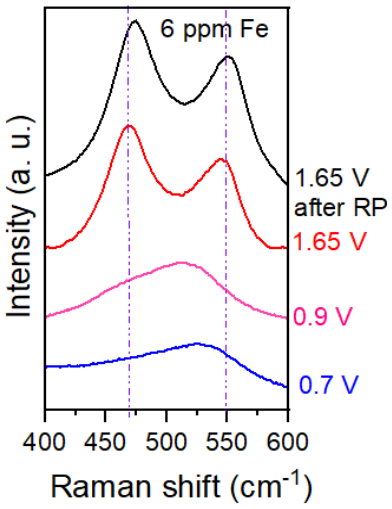


Figure B.9: Ex-situ Raman spectra of NixFe(1-x)OOH as a function of final resting potential in Fe-containing electrolyte. Ex-situ Raman spectra of $Ni_xFe_{(1-x)}OOH$ in 30% w/w KOH, [Fe] = 6 ppm, at 80 °C, recorded at five potentials along the discharge curve.

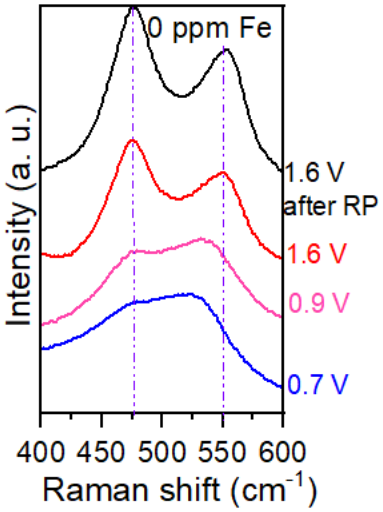


Figure B.10: Ex-situ Raman spectra of NixFe(1-x)OOH as a function of final resting potential in Fe-free electrolyte. Ex-situ Raman spectra of NiOOH in 30% w/w KOH, [Fe] = 0 ppm, at 80 °C, recorded at five potentials along the discharge curve.

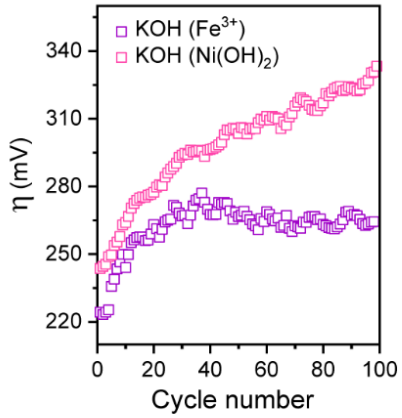


Figure B.11: Cycle-dependent OER activity in KOH spiked with Fe^{3+} or $Ni(OH)_2$. The OER overpotential was measured at 2 mA cm^{-2} for the thin-film $Ni_xFe_{(1-x)}OOH$ charged at 1 A cm^{-2} and discharged at a constant current of –0.1 mA cm^{-2} to 0.700 V vs RHE in 6 ppm Fe containing 30% w/w KOH with insoluble $Ni(OH)_2$.

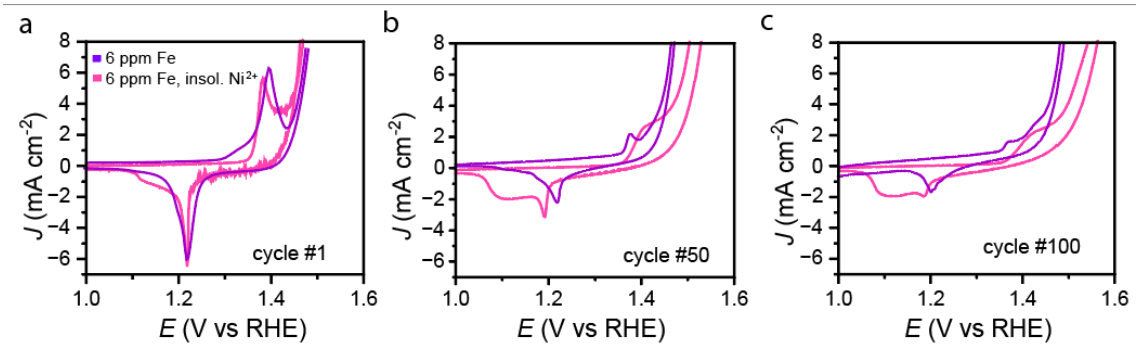


Figure B.12: Influence of cycling on the voltammetry of thin-film catalysts in KOH spiked with dissolved Fe or solid $Ni(OH)_2$. Cyclic voltammograms of thin film $Ni_xFe_{(1-x)}OOH$ coated on Pt foil after a) 1, b) 50, and c) 100 cycles, where the electrode was charged at 1.0 A cm^{-2} and discharged at a constant current of –0.1 mA cm^{-2} to 0.700 V vs RHE in a three-electrode cell with 6 ppm Fe containing 30% w/w KOH with insoluble $Ni(OH)_2$ (ν = 50 mV s^{-1}).

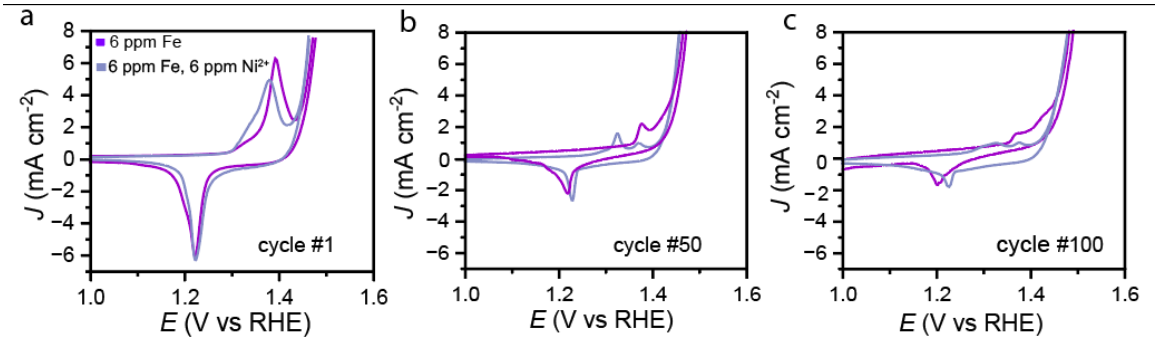


Figure B.13: Influence of cycling on the voltammetry of thin-film catalysts in KOH spiked with dissolved Fe or a mixture of dissolved Fe and Ni. Cyclic voltammograms of thin film $Ni_xFe_{(1-x)}OOH$ coated on Pt foil, after a) 1, b) 50, and c) 100 cycles, where the electrode was charged at 1 A cm^{-2} and discharged at a constant current of –0.1 mA cm^{-2} to 0.700 V vs RHE in a 3-electrode cell with 6 ppm Fe containing 30% w/w KOH with 6 ppm Ni^{2+}. (ν = 50 mV s^{-1}).

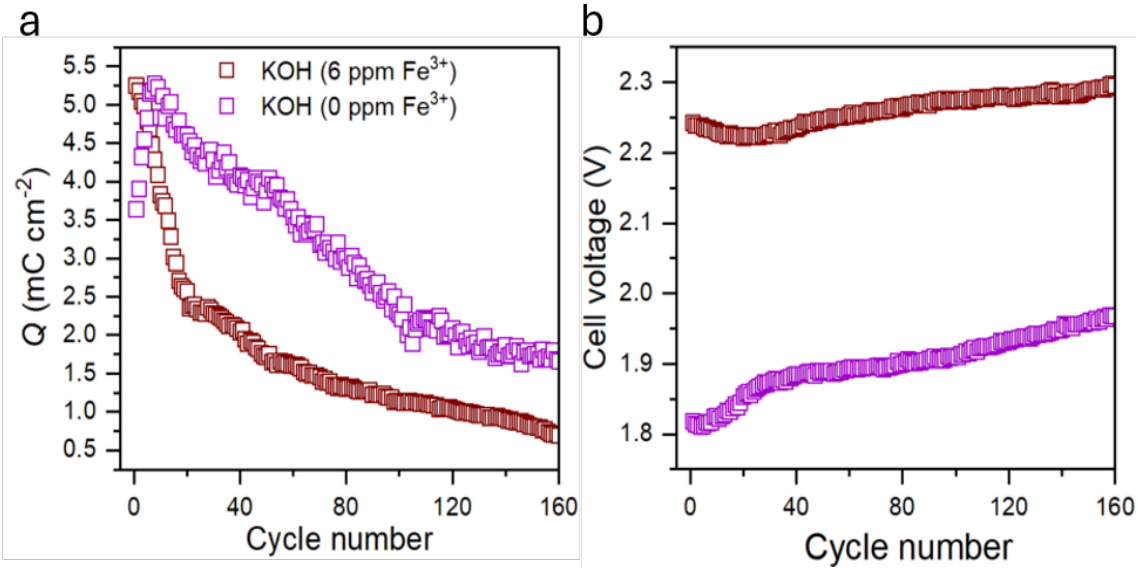


Figure B.14: Impact of cycle number on discharge capacity of thin-film catalysts in electrolyte with and without spiked Fe. a) Discharge capacity decay for thin film NiOOH coated on Pt-Ti mesh in a zero-gap cell with 30% w/w KOH containing 0 and 6 ppm Fe. The electrode was charged at 400 mA cm^{-2} and discharged at a constant current of -0.1 mA cm^{-2} to 0.7 V vs RHE. b) Cell voltage for thin film NiOOH coated on Pt-Ti mesh in a zero-gap cell with 30% w/w KOH containing 0 and 6 ppm Fe. The electrode was charged at 400 mA cm^{-2} and discharged at a constant current of -0.1 mA cm^{-2} to 0.7 V vs RHE.

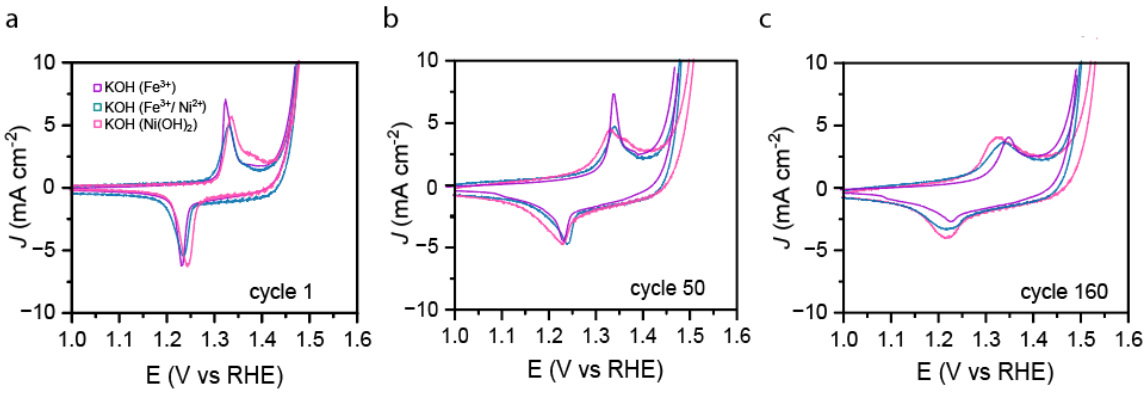


Figure B.15: Influence of cycling on the voltammetry of mesh-supported catalysts in KOH spiked with dissolved Fe, a mixture of dissolved Fe and Ni, or solid $Ni(OH)_2$. Cyclic voltammograms of thin film $Ni_xFe_{(1-x)}OOH$ coated on Pt-Ti mesh, where the electrode was charged at 400 mA cm^{-2} and discharged at a constant current of –0.1 mA cm^{-2} to 0.700 V vs RHE in a zero-gap cell with 6 ppm Fe containing 30% w/w KOH with insoluble $Ni(OH)_2$ (ν = 50 mV s^{-1}).

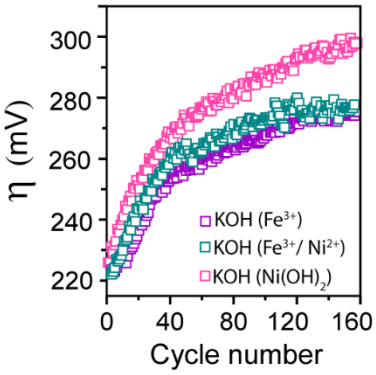


Figure B.16: Overpotential versus cycle number for mesh-supported catalysts in various electrolytes. The OER overpotential at 5 mA cm^{-2} for the thin-film $Ni_xFe_{(1-x)}OOH$ coated on Pt-Ti mesh charged at 400 mA cm^{-2} and discharged at a constant current of –0.1 mA cm^{-2} to 0.700 V vs RHE in 6 ppm Fe containing 30 w/w % KOH with insoluble $Ni(OH)_2$.

APPENDIX III

Chapter III: Supplemental Information

Table C1: Surface atomic composition of thin-film $Ni_xFe_{(1-x)}OOH$ electrode operated in aged-OER 3 h electrolyte before and after 100 charge-discharge cycles.

	Before	After
Fe	3.30	0.72
Ni	26.08	38.82
O	66.29	60.15
Cr	0.69	0.31
Mn	3.64	N/D

The electrode has been charged at 400 mA cm^{-2} and discharged at J = -0.1 mA cm^{-2} to 0.7 V vs RHE. N/D is used for not detected.

Chapter III: Supporting Figures

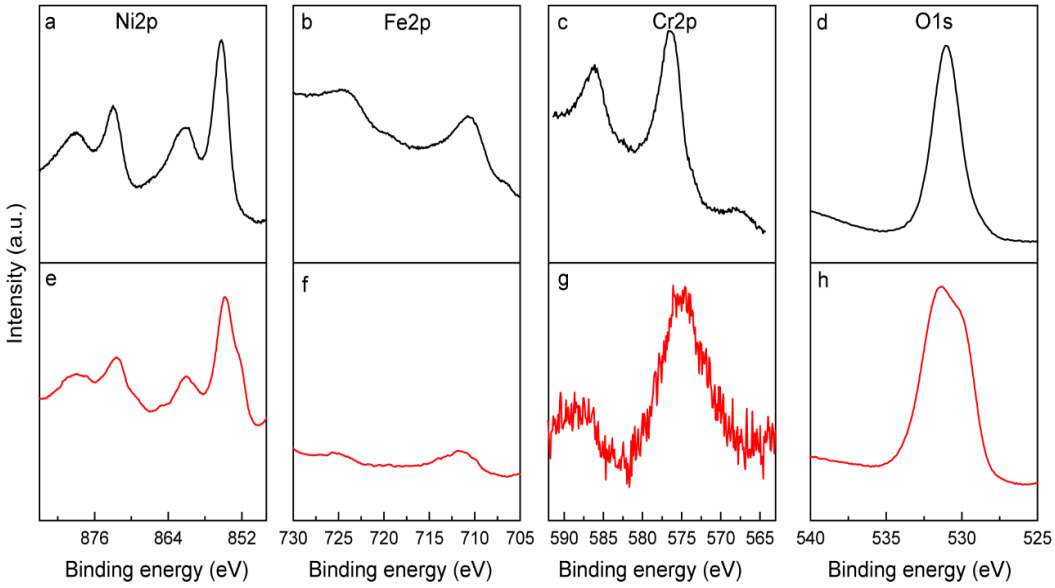


Figure C.1: X-ray photoelectron spectra of thin-film $Ni_xFe_{(1-x)}OOH$ electrode operated in aged-OER 3 h electrolyte before (top) and after (bottom) 100 charge-discharge analysis. The electrode has been charged at 400 mA cm^{-2} and discharged at J = -0.1 mA cm^{-2} to 0.7 V vs RHE. The spectra show the regions (a, e) Ni2p, (b, f) Fe2p, (c, g) Cr2p, and (d, h) O1s.

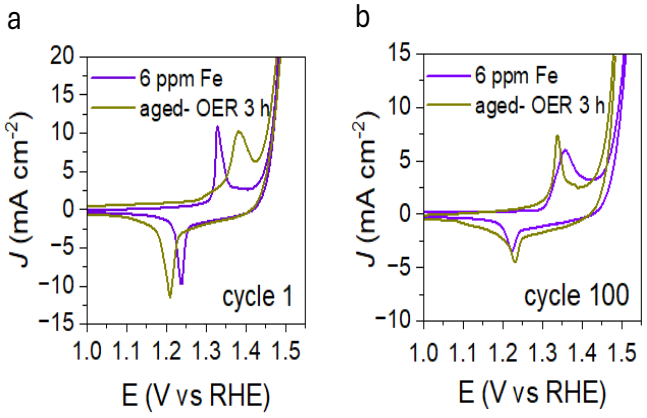


Figure C.2: Cyclic voltammetry of thin-film $Ni_xFe_{(1-x)}OOH$ electrode operated in 6 ppm Fe containing 30% w/w KOH and aged-OER 3 h electrolyte before a) and after (b) 100 charge-discharge cycles. The electrode has been charged at 400 mA cm^{-2} and discharged at J = -0.1 mA cm^{-2} to 0.7 V vs RHE. The scan rate is 50 mV/s.

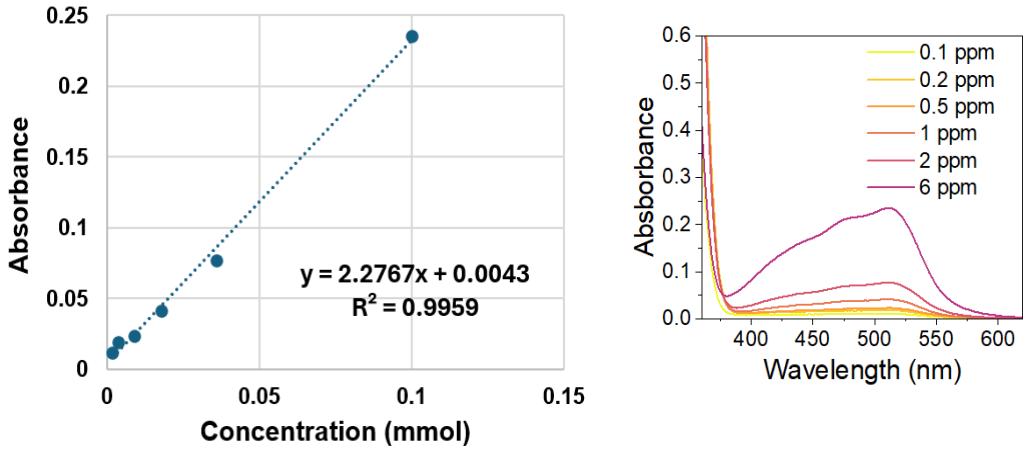


Figure C.3 a) UV-vis calibration curve for Fe quantification using the Fe^{2+}-1,10-phenanthroline complex. Fe-containing standards were acidified to pH 3- 4, reduced with hydroxylamine hydrochloride, and complexed with 1,10-phenanthroline before absorbance measurement. The dotted line represents the linear regression fit b) Change in absorbance as a function of dissolved Fe concentration for Fe-phenanthroline complex.

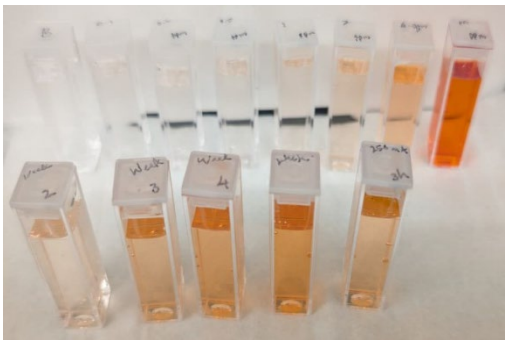


Figure C.4: Bright red colored Fe-phenanthroline complex used for UV-Vis analysis.

References

(1) Chatenet, M.; G. Pollet, B.; R. Dekel, D.; Dionigi, F.; Deseure, J.; Millet, P.; D. Braatz, R.; Z. Bazant, M.; Eikerling, M.; Staffell, I.; Balcombe, P.; Shao-Horn, Y.; Schäfer, H. Water Electrolysis: From Textbook Knowledge to the Latest Scientific Strategies and Industrial Developments. *Chem. Soc. Rev.* **2022**, *51* (11), 4583–4762. https://doi.org/10.1039/D0CS01079K.

(2) Tilak, B. V.; Lu, P. W. T.; Colman, J. E.; Srinivasan, S. Electrolytic Production of Hydrogen. In *Comprehensive Treatise of Electrochemistry: Electrochemical Processing*; Bockris, J. O., Conway, B. E., Yeager, E., White, R. E., Eds.; Comprehensive Treatise of Electrochemistry; Springer US: Boston, MA, 1981; pp 1–104. https://doi.org/10.1007/978-1-4684-3785-0_1.

(3) IRENA. *Green Hydrogen Cost Reduction*; IRENA, 2020. https://www.irena.org/Publications/2020/Dec/Green-hydrogen-cost-reduction (accessed 2023-05-24).

(4) Pletcher, D.; Li, X.; Wang, S. A Comparison of Cathodes for Zero Gap Alkaline Water Electrolysers for Hydrogen Production. *international journal of hydrogen energy* **2012**, *37* (9), 7429–7435.

(5) Trotochaud, L.; Ranney, J. K.; Williams, K. N.; Boettcher, S. W. Solution-Cast Metal Oxide Thin Film Electrocatalysts for Oxygen Evolution. *J. Am. Chem. Soc.* **2012**, *134* (41), 17253–17261. https://doi.org/10.1021/ja307507a.

(6) Hall, D. E. Alkaline Water Electrolysis Anode Materials. *Journal of The Electrochemical Society* **1985**, *132* (2), 41C.

(7) Wendt, H.; Imarisio, G. Nine Years of Research and Development on Advanced Water Electrolysis. A Review of the Research Programme of the Commission of the European Communities. *J Appl Electrochem* **1988**, *18* (1), 1–14. https://doi.org/10.1007/BF01016198.

(8) Karacan, C.; Lohmann-Richters, F. P.; Shviro, M.; Keeley, G. P.; Müller, M.; Carmo, M.; Stolten, D. Fabrication of High Performing and Durable Nickel-Based Catalyst Coated Diaphragms for Alkaline Water Electrolyzers. *J. Electrochem. Soc.* **2022**, *169* (5), 054502. https://doi.org/10.1149/1945-7111/ac697f.

(9) Mergel, J.; Carmo, M.; Fritz, D. Status on Technologies for Hydrogen Production by Water Electrolysis. In *Transition to Renewable Energy Systems*; Stolten, D., Scherer, V., Eds.; Wiley, 2013; pp 423–450. https://doi.org/10.1002/9783527673872.ch22.

(10) de Groot, M. T.; Kraakman, J.; Garcia Barros, R. L. Optimal Operating Parameters for Advanced Alkaline Water Electrolysis. *International Journal of Hydrogen Energy* **2022**, *47* (82), 34773–34783. https://doi.org/10.1016/j.ijhydene.2022.08.075.

(11) Dunnill, R., Charles W. ,. Phillips. Zero Gap Alkaline Electrolysis Cell Design for Renewable Energy Storage as Hydrogen Gas. *RSC Advances*, 2016. https://doi.org/10.1039/C6RA22242K.

(12) Kraglund, M. R.; Carmo, M.; Schiller, G.; Ansar, S. A.; Aili, D.; Christensen, E.; Jensen, J. O. Ion-Solvating Membranes as a New Approach towards High Rate

Alkaline Electrolyzers. *Energy & Environmental Science*, 2019. https://doi.org/10.1039/C9EE00832B.
(13) Goyal, A.; Louisia, S.; Moerland, P.; Koper, M. T. M. Cooperative Effect of Cations and Catalyst Structure in Tuning Alkaline Hydrogen Evolution on Pt Electrodes. *J. Am. Chem. Soc.* **2024**, *146* (11), 7305–7312. https://doi.org/10.1021/jacs.3c11866.
(14) Ringe, S. Cation Effects on Electrocatalytic Reduction Processes at the Example of the Hydrogen Evolution Reaction. *Current Opinion in Electrochemistry* **2023**, *39*, 101268. https://doi.org/10.1016/j.coelec.2023.101268.
(15) Bender, J. T.; Petersen, A. S.; Østergaard, F. C.; Wood, M. A.; Heffernan, S. M. J.; Milliron, D. J.; Rossmeisl, J.; Resasco, J. Understanding Cation Effects on the Hydrogen Evolution Reaction. *ACS Energy Lett.* **2023**, *8* (1), 657–665. https://doi.org/10.1021/acsenergylett.2c02500.
(16) Monteiro, M. C. O.; Goyal, A.; Moerland, P.; Koper, M. T. M. Understanding Cation Trends for Hydrogen Evolution on Platinum and Gold Electrodes in Alkaline Media. *ACS Catal.* **2021**, *11* (23), 14328–14335. https://doi.org/10.1021/acscatal.1c04268.
(17) Mahmood, N.; Yao, Y.; Zhang, J.; Pan, L.; Zhang, X.; Zou, J. Electrocatalysts for Hydrogen Evolution in Alkaline Electrolytes: Mechanisms, Challenges, and Prospective Solutions. *Advanced Science* **2018**, *5* (2), 1700464. https://doi.org/10.1002/advs.201700464.
(18) Xue, S.; Garlyyev, B.; Watzele, S.; Liang, Y.; Fichtner, J.; Pohl, M. D.; Bandarenka, A. S. Influence of Alkali Metal Cations on the Hydrogen Evolution Reaction Activity of Pt, Ir, Au, and Ag Electrodes in Alkaline Electrolytes. *ChemElectroChem* **2018**, *5* (17), 2326–2329. https://doi.org/10.1002/celc.201800690.
(19) Zaffran, J.; Stevens, M. B.; Trang, C. D. M.; Nagli, M.; Shehadeh, M.; Boettcher, S. W.; Caspary Toroker, M. Influence of Electrolyte Cations on Ni(Fe)OOH Catalyzed Oxygen Evolution Reaction. *Chem. Mater.* **2017**, *29* (11), 4761–4767. https://doi.org/10.1021/acs.chemmater.7b00517.
(20) Garcia, A. C.; Touzalin, T.; Nieuwland, C.; Perini, N.; Koper, M. T. M. Enhancement of Oxygen Evolution Activity of Nickel Oxyhydroxide by Electrolyte Alkali Cations. *Angewandte Chemie International Edition* **2019**, *58* (37), 12999–13003. https://doi.org/10.1002/anie.201905501.
(21) Corrigan, D. A. The Catalysis of the Oxygen Evolution Reaction by Iron Impurities in Thin Film Nickel Oxide Electrodes. *J. Electrochem. Soc.* **1987**, *134* (2), 377. https://doi.org/10.1149/1.2100463.
(22) Trotochaud, L.; Young, S. L.; Ranney, J. K.; Boettcher, S. W. Nickel–Iron Oxyhydroxide Oxygen-Evolution Electrocatalysts: The Role of Intentional and Incidental Iron Incorporation. *J. Am. Chem. Soc.* **2014**, *136* (18), 6744–6753. https://doi.org/10.1021/ja502379c.
(23) Ou, Y.; Twight, L. P.; Samanta, B.; Liu, L.; Biswas, S.; Fehrs, J. L.; Sagui, N. A.; Villalobos, J.; Morales-Santelices, J.; Antipin, D.; Risch, M.; Toroker, M. C.; Boettcher, S. W. Cooperative Fe Sites on Transition Metal (Oxy)Hydroxides Drive High Oxygen Evolution Activity in Base. *Nat Commun* **2023**, *14* (1), 7688. https://doi.org/10.1038/s41467-023-43305-z.

(24) Demnitz, M.; Lamas, Y. M.; Garcia Barros, R. L.; De Leeuw Den Bouter, A.; Van Der Schaaf, J.; Theodorus De Groot, M. Effect of Iron Addition to the Electrolyte on Alkaline Water Electrolysis Performance. *iScience* **2024**, *27* (1), 108695. https://doi.org/10.1016/j.isci.2023.108695.
(25) Xue, S.; Haid, R. W.; Kluge, R. M.; Ding, X.; Garlyyev, B.; Fichtner, J.; Watzele, S.; Hou, S.; Bandarenka, A. S. Enhancing the Hydrogen Evolution Reaction Activity of Platinum Electrodes in Alkaline Media Using Nickel–Iron Clusters. *Angewandte Chemie International Edition* **2020**, *59* (27), 10934–10938. https://doi.org/10.1002/anie.202000383.
(26) Nidola, A.; Schira, R. Poisoning Mechanisms and Structural Analyses on Metallic Contaminated Cathode Catalysts in Chlor-Alkali Membrane Cell Technology. *J. Electrochem. Soc.* **1986**, *133* (8), 1653. https://doi.org/10.1149/1.2108984.
(27) *NRG® (Hydrogen Generation Products) | De Nora*. denora. https://www.denora.com/our-brands/NRG.html (accessed 2024-06-07).
(28) Oda, K.; Kuroda, Y.; Mitsushima, S. Investigation of Charge–Discharging Behavior of Metal Oxide–Based Anode Electrocatalysts for Alkaline Water Electrolysis to Suppress Degradation Due to Reverse Current. *Electrocatalysis* **2023**, *14* (3), 499–510. https://doi.org/10.1007/s12678-023-00815-0.
(29) Abdel Haleem, A.; Huyan, J.; Nagasawa, K.; Kuroda, Y.; Nishiki, Y.; Kato, A.; Nakai, T.; Araki, T.; Mitsushima, S. Effects of Operation and Shutdown Parameters and Electrode Materials on the Reverse Current Phenomenon in Alkaline Water Analyzers. *Journal of Power Sources* **2022**, *535*, 231454. https://doi.org/10.1016/j.jpowsour.2022.231454.
(30) Burke, M. S.; Kast, M. G.; Trotochaud, L.; Smith, A. M.; Boettcher, S. W. Cobalt–Iron (Oxy)Hydroxide Oxygen Evolution Electrocatalysts: The Role of Structure and Composition on Activity, Stability, and Mechanism. *J. Am. Chem. Soc.* **2015**, *137* (10), 3638–3648. https://doi.org/10.1021/jacs.5b00281.
(31) Batchellor, A. S.; Boettcher, S. W. Pulse-Electrodeposited Ni–Fe (Oxy)Hydroxide Oxygen Evolution Electrocatalysts with High Geometric and Intrinsic Activities at Large Mass Loadings. *ACS Catal.* **2015**, *5* (11), 6680–6689. https://doi.org/10.1021/acscatal.5b01551.
(32) Dionigi, F.; Zhu, J.; Zeng, Z.; Merzdorf, T.; Sarodnik, H.; Gliech, M.; Pan, L.; Li, W.-X.; Greeley, J.; Strasser, P. Intrinsic Electrocatalytic Activity for Oxygen Evolution of Crystalline 3d-Transition Metal Layered Double Hydroxides. *Angewandte Chemie* **2021**, *133* (26), 14567–14578. https://doi.org/10.1002/ange.202100631.
(33) Klaus, S.; Cai, Y.; Louie, M. W.; Trotochaud, L.; Bell, A. T. Effects of Fe Electrolyte Impurities on Ni(OH)2/NiOOH Structure and Oxygen Evolution Activity. *J. Phys. Chem. C* **2015**, *119* (13), 7243–7254. https://doi.org/10.1021/acs.jpcc.5b00105.
(34) Allanore, A.; Lavelaine, H.; Valentin, G.; Birat, J. P.; Lapicque, F. Electrodeposition of Metal Iron from Dissolved Species in Alkaline Media. *J. Electrochem. Soc.* **2007**, *154* (12), E187. https://doi.org/10.1149/1.2790285.
(35) Huot, J.-Y. Hydrogen Evolution and Interface Phenomena on a Nickel Cathode in 30 w/o KOH : I . Kinetics Parameters and Electrode Impedance Between 303 and 363 K. *J. Electrochem. Soc.* **1989**, *136* (7), 1933. https://doi.org/10.1149/1.2097088.

(36) Brossard, L.; Huot, J.-Y. In Situ Activation of Cathodes during Alkaline Water Electrolysis by Dissolved Iron and Molybdenum Species. *J Appl Electrochem* **1991**, *21* (6), 508–515. https://doi.org/10.1007/BF01018603.
(37) Twight, L.; Tonsberg, A.; Samira, S.; Velinkar, K.; Dumpert, K.; Ou, Y.; Wang, L.; Nikolla, E.; Boettcher, S. Trace Fe in Alkaline Electrolyte Governs the OER Activity of Perovskite LaNiO3 and La2NiO4 via Interaction with Redox-Active Surface NiOxHy Formed by Applied Bias. October 4, 2023. https://doi.org/10.26434/chemrxiv-2023-0rd31.
(38) Krivina, R. A.; Ou, Y.; Xu, Q.; Twight, L. P.; Stovall, T. N.; Boettcher, S. W. Oxygen Electrocatalysis on Mixed-Metal Oxides/Oxyhydroxides: From Fundamentals to Membrane Electrolyzer Technology. *Acc. Mater. Res.* **2021**, *2* (7), 548–558. https://doi.org/10.1021/accountsmr.1c00087.
(39) Beverskog, B.; Puigdomenech, I. Revised Pourbaix Diagrams for Iron at 25–300 C. *Corrosion Science* **1996**, *38* (12), 2121–2135.
(40) Batchellor, A.; Kwon, G.; Laskowski, F.; Tiede, D.; Boettcher, S. Domain Structures of Ni and NiFe (Oxy)Hydroxide Oxygen-Evolution Catalysts from X-Ray Pair Distribution Function Analysis. *The Journal of Physical Chemistry C* **2017**, *121*. https://doi.org/10.1021/acs.jpcc.7b10306.
(41) de Faria, D. L. A.; Venâncio Silva, S.; de Oliveira, M. T. Raman microspectroscopy of some iron oxides and oxyhydroxides. *Journal of Raman Spectroscopy* **1997**, *28* (11), 873–878. https://doi.org/10.1002/(SICI)1097-4555(199711)28:11%3C873::AID-JRS177%3E3.0.CO;2-B.
(42) Chen, Z.; Cai, L.; Yang, X.; Kronawitter, C.; Guo, L.; Shen, S.; Koel, B. E. Reversible Structural Evolution of $NiCoO_xH_y$ during the Oxygen Evolution Reaction and Identification of the Catalytically Active Phase. *ACS Catal.* **2018**, *8* (2), 1238–1247. https://doi.org/10.1021/acscatal.7b03191.
(43) Liu, Y.; Smith, R. D. L. Identifying Protons Trapped in Hematite Photoanodes through Structure–Property Analysis. *Chem. Sci.* **2020**, *11* (4), 1085–1096. https://doi.org/10.1039/C9SC04853G.
(44) Subbaraman, R.; Tripkovic, D.; Chang, K.-C.; Strmcnik, D.; Paulikas, A. P.; Hirunsit, P.; Chan, M.; Greeley, J.; Stamenkovic, V.; Markovic, N. M. Trends in Activity for the Water Electrolyser Reactions on 3d M(Ni,Co,Fe,Mn) Hydr(Oxy)Oxide Catalysts. *Nature Mater* **2012**, *11* (6), 550–557. https://doi.org/10.1038/nmat3313.
(45) Pletcher, D.; Li, X. Prospects for Alkaline Zero Gap Water Electrolysers for Hydrogen Production. *International Journal of Hydrogen Energy* **2011**, *36* (23), 15089–15104. https://doi.org/10.1016/j.ijhydene.2011.08.080.
(46) Boettcher, S. W. Introduction to Green Hydrogen. *Chem. Rev.* **2024**, *124* (23), 13095–13098. https://doi.org/10.1021/acs.chemrev.4c00787.
(47) Fischer, J.; Hofmann, H.; Luft, G.; Wendt, H. Fundamental Investigations and Electrochemical Engineering Aspects Concerning an Advanced Concept for Alkaline Water Electrolysis. *AIChE Journal*, 1980, *26*, 794–802.
(48) de Groot, M. T.; Kraakman, J.; Garcia Barros, R. L. Optimal Operating Parameters for Advanced Alkaline Water Electrolysis. *International Journal of Hydrogen Energy* **2022**, *47* (82), 34773–34783. https://doi.org/10.1016/j.ijhydene.2022.08.075.

(49) Marquez, R. A.; Bender, J. T.; Aleman, A. M.; Kalokowski, E.; Vy Le, T.; Williamson, C. L.; Frederiksen, M. L.; Kawashima, K.; Chukwuneke, C. E.; Dolocan, A.; Milliron, D. J.; Resasco, J.; Jaramillo, T. F.; Buddie Mullins, C. Insights into Catalyst Degradation during Alkaline Water Electrolysis under Variable Operation. *Energy Environ. Sci.* **2025**, *18* (14), 7170–7187. https://doi.org/10.1039/D5EE02194D.
(50) Samu, A. A.; Kormányos, A.; Kecsenovity, E.; Szilágyi, N.; Endrődi, B.; Janáky, C. Intermittent Operation of CO_2 Electrolyzers at Industrially Relevant Current Densities. *ACS Energy Lett.* **2022**, *7* (5), 1859–1861. https://doi.org/10.1021/acsenergylett.2c00923.
(51) Han, S.; Kim, S.; Cho, H. J.; Lee, J. Y.; Ryu, J.; Yoon, J. Dynamic Polarization Control of Ni Electrodes for Sustainable and Scalable Water Electrolysis under Alkaline Conditions. *Nat Commun* **2025**, *16* (1), 4803. https://doi.org/10.1038/s41467-025-60201-w.
(52) Oda, K.; Kuroda, Y.; Mitsushima, S. Investigation of Charge–Discharging Behavior of Metal Oxide–Based Anode Electrocatalysts for Alkaline Water Electrolysis to Suppress Degradation Due to Reverse Current. *Electrocatalysis* **2023**, *14* (3), 499–510. https://doi.org/10.1007/s12678-023-00815-0.
(53) Rasten, E. (Invited) Shunt-Currents in Alkaline Water-Electrolyzers and Renewable Energy. *ECS Trans.* **2024**, *113* (9), 25–41. https://doi.org/10.1149/11309.0025ecst.
(54) Ehlers, J. C.; Larrazábal, G. O.; Egelund, S. D.; Chatzichristodoulou, C. Nickel Anode Evolution and Mass Loss during Intermittent Alkaline Water Electrolysis. *Chemical Engineering Journal* **2025**, *525*, 169990. https://doi.org/10.1016/j.cej.2025.169990.
(55) Uchino, Y.; Kobayashi, T.; Hasegawa, S.; Nagashima, I.; Sunada, Y.; Manabe, A.; Nishiki, Y.; Mitsushima, S. Dependence of the Reverse Current on the Surface of Electrode Placed on a Bipolar Plate in an Alkaline Water Electrolyzer. *Electrochemistry* **2018**, *86* (3), 138–144. https://doi.org/10.5796/electrochemistry.17-00102.
(56) Etzi Coller Pascuzzi, M.; Man, A. J. W.; Goryachev, A.; Hofmann, J. P.; Hensen, E. J. M. Investigation of the Stability of NiFe-(Oxy)Hydroxide Anodes in Alkaline Water Electrolysis under Industrially Relevant Conditions. *Catal. Sci. Technol.* **2020**, *10* (16), 5593–5601. https://doi.org/10.1039/D0CY01179G.
(57) Ehlers, J. C.; Larrazábal, G. O.; Egelund, S. D.; Chatzichristodoulou, C. Nickel Anode Evolution and Mass Loss during Intermittent Alkaline Water Electrolysis. SSRN 2025. https://doi.org/10.2139/ssrn.5412738.
(58) *Boosting the Oxygen Evolution Reaction Performance of Ni-Fe-Electrodes by Tailored Conditioning - Gohlke - 2024 - ChemElectroChem - Wiley Online Library*. https://chemistry-europe.onlinelibrary.wiley.com/doi/10.1002/celc.202400318 (accessed 2026-07-02).
(59) Moreno Fernández, H.; Alkemper, A.; Wang, K.; Mempin, C. Jr.; Gallenberger, J.; Hofmann, J. P. Kinetic Analysis of the Self-Discharge of the NiOOH OER Active Phase in KOH Electrolyte: Insights from in-Situ Raman and UV–Vis Reflectance Spectroscopies. *Journal of Catalysis* **2024**, *440*, 115823. https://doi.org/10.1016/j.jcat.2024.115823.

(60) Friebel, D.; Louie, M. W.; Bajdich, M.; Sanwald, K. E.; Cai, Y.; Wise, A. M.; Cheng, M.-J.; Sokaras, D.; Weng, T.-C.; Alonso-Mori, R.; Davis, R. C.; Bargar, J. R.; Nørskov, J. K.; Nilsson, A.; Bell, A. T. Identification of Highly Active Fe Sites in (Ni,Fe)OOH for Electrocatalytic Water Splitting. *J. Am. Chem. Soc.* **2015**, *137* (3), 1305–1313. https://doi.org/10.1021/ja511559d.
(61) Volk, E. K.; Kreider, M. E.; Gibson Colón, D. M.; Müller, M.; Sunde, S.; Alia, S. M.; Kwon, S. Electrochemical Activation of Ni–Fe Oxides for the Oxygen Evolution Reaction in Alkaline Media. *ACS Catal.* **2025**, *15* (13), 11475–11486. https://doi.org/10.1021/acscatal.5c02405.
(62) Kostecki, R.; McLarnon, F. Electrochemical and In Situ Raman Spectroscopic Characterization of Nickel Hydroxide Electrodes: I. Pure Nickel Hydroxide. *J. Electrochem. Soc.* **1997**, *144* (2), 485. https://doi.org/10.1149/1.1837437.
(63) Hall, D. S.; Lockwood, D. J.; Bock, C.; MacDougall, B. R. Nickel Hydroxides and Related Materials: A Review of Their Structures, Synthesis and Properties. *Proc. R. Soc. A.* **2015**, *471* (2174), 20140792. https://doi.org/10.1098/rspa.2014.0792.
(64) Bode, H.; Dehmelt, K.; Witte, J. Zur Kenntnis Der Nickelhydroxidelektrode—I.Über Das Nickel (II)-Hydroxidhydrat. *Electrochimica Acta* **1966**, *11* (8), 1079–1087. https://doi.org/10.1016/0013-4686(66)80045-2.
(65) Stevens, M. B.; Enman, L. J.; Batchellor, A. S.; Cosby, M. R.; Vise, A. E.; Trang, C. D. M.; Boettcher, S. W. Measurement Techniques for the Study of Thin Film Heterogeneous Water Oxidation Electrocatalysts. *Chem. Mater.* **2017**, *29* (1), 120–140. https://doi.org/10.1021/acs.chemmater.6b02796.
(66) Rajeev, M.; Jerome-Saboori, A.; Shekhar, R.; Boettcher, S. W.; Kempler, P. A. Impacts of Dissolved Iron on Alkaline Water Electrolysis Cells. *ACS Catal.* **2025**, *15* (4), 2847–2856. https://doi.org/10.1021/acscatal.4c07439.
(67) Huang, Y.; Kong, F.; Yu, X.; Yang, T.; Wu, P.; Shen, R.; Zhuo, S.; Cui, X.; Shi, J. Stabilizing the Fe Species of Nickel-Iron Double Hydroxide via Chelating Asymmetric Aldehyde-Containing THB Ligand for Long-Lasting Water Oxidation. *Advanced Materials* **2025**, *37* (7), 2419887. https://doi.org/10.1002/adma.202419887.
(68) Ali-Löytty, H.; Louie, M. W.; Singh, M. R.; Li, L.; Sanchez Casalongue, H. G.; Ogasawara, H.; Crumlin, E. J.; Liu, Z.; Bell, A. T.; Nilsson, A.; Friebel, D. Ambient-Pressure XPS Study of a Ni–Fe Electrocatalyst for the Oxygen Evolution Reaction. *J. Phys. Chem. C* **2016**, *120* (4), 2247–2253. https://doi.org/10.1021/acs.jpcc.5b10931.
(69) Grosvenor, A. P.; Biesinger, M. C.; Smart, R. St. C.; McIntyre, N. S. New Interpretations of XPS Spectra of Nickel Metal and Oxides. *Surface Science* **2006**, *600* (9), 1771–1779. https://doi.org/10.1016/j.susc.2006.01.041.
(70) Chung, D. Y.; Lopes, P. P.; Farinazzo Bergamo Dias Martins, P.; He, H.; Kawaguchi, T.; Zapol, P.; You, H.; Tripkovic, D.; Strmcnik, D.; Zhu, Y.; Seifert, S.; Lee, S.; Stamenkovic, V. R.; Markovic, N. M. Dynamic Stability of Active Sites in Hydr(Oxy)Oxides for the Oxygen Evolution Reaction. *Nat Energy* **2020**, *5* (3), 222–230. https://doi.org/10.1038/s41560-020-0576-y.
(71) Thissen, N.; Deo, Y.; Fernández, H. M.; Seidl, V.; Hofmann, J. P.; Mechler, A. K. Iron as a Key Contributor in Stability Investigations of Alkaline Water Electrolysis

Electrodes. Cell Reports Physical Science **2026**, 7 (3). https://doi.org/10.1016/j.xcrp.2026.103138.
(72) Poli, S.; Poleunis, C.; Miola, M.; Gerlach, D.; Rudolf, P.; Delcorte, A.; Lammers, H.; Groot, M. T. de; M. Morales, D.; P. Pescarmona, P. Regeneration of Iron Species for High and Stable Activity of Nickel Electrodes in the Oxygen Evolution Reaction. *Green Chemistry* **2025**, *27* (28), 8505–8516. https://doi.org/10.1039/D5GC00114E.
(73) Stevens, M. B.; Trang, C. D. M.; Enman, L. J.; Deng, J.; Boettcher, S. W. Reactive Fe-Sites in Ni/Fe (Oxy)Hydroxide Are Responsible for Exceptional Oxygen Electrocatalysis Activity. *J. Am. Chem. Soc.* **2017**, *139* (33), 11361–11364. https://doi.org/10.1021/jacs.7b07117.
(74) Nikoloski, A. N.; Nicol, M. J. Effect of Cobalt Ions on the Performance of Lead Anodes Used for the Electrowinning of Copper—a Literature Review. *Mineral Processing and Extractive Metallurgy Review* **2007**, *29* (2), 143–172. https://doi.org/10.1080/08827500701421870.
(75) Surendranath, Y.; Lutterman, D. A.; Liu, Y.; Nocera, D. G. Nucleation, Growth, and Repair of a Cobalt-Based Oxygen Evolving Catalyst. *J. Am. Chem. Soc.* **2012**, *134* (14), 6326–6336. https://doi.org/10.1021/ja3000084.
(76) Kim, Y.; Jung, S.-M.; Kim, K.-S.; Kim, H.-Y.; Kwon, J.; Lee, J.; Cho, H.-S.; Kim, Y.-T. Cathodic Protection System against a Reverse-Current after Shut-Down in Zero-Gap Alkaline Water Electrolysis. *JACS Au* **2022**, *2* (11), 2491–2500. https://doi.org/10.1021/jacsau.2c00314.
(77) Abdel Haleem, A.; Huyan, J.; Nagasawa, K.; Kuroda, Y.; Nishiki, Y.; Kato, A.; Nakai, T.; Araki, T.; Mitsushima, S. Effects of Operation and Shutdown Parameters and Electrode Materials on the Reverse Current Phenomenon in Alkaline Water Analyzers. *Journal of Power Sources* **2022**, *535*, 231454. https://doi.org/10.1016/j.jpowsour.2022.231454.
(78) Gras, J.; Spiteri, P. Corrosion of Stainless Steels and Nickel-Based Alloys for Alkaline Water Electrolysis. *International Journal of Hydrogen Energy* **1993**. https://doi.org/10.1016/0360-3199(93)90175-a.
(79) Sarfraz, B.; Gupta, K. K.; Ambat, R. Designing Durable Alkaline Electrolyzer Systems: A Comprehensive Review on Corrosion of Materials and Its Impact. *Corrosion Communications* **2026**. https://doi.org/10.1016/j.corcom.2026.03.030.
(80) Matošec, M. *Duplex stainless steel as a material of construction in alkaline electrolyzers*. Hydrogen Tech World.com. https://hydrogentechworld.com/duplex-stainless-steel-as-a-material-of-construction-in-alkaline-electrolyzers (accessed 2026-07-22).
(81) Zagoraiou, E.; Krishan, S.; Siriwardana, A.; Moschovi, A. M.; Yakoumis, I. Performance of Stainless-Steel Bipolar Plates (SS-BPPs) in Polymer Electrolyte Membrane Water Electrolyser (PEMWE): A Comprehensive Review. *Compounds* **2024**, *4* (2), 252–267. https://doi.org/10.3390/compounds4020013.
(82) Jiao, H.; Tian, H.; Wang, C.; Chen, J.-Y.; Zhang, Z.-Y.; Na, P.; Wang, Z.-L. Chromium Oxidation-Dissolution Promotes the Transformation of Alloy Films to Active Oxyhydroxides for Enhanced Water Oxidation. *Applied Catalysis B: Environment and Energy* **2026**, *382*, 125973. https://doi.org/10.1016/j.apcatb.2025.125973.

(83) Rajeev, M.; Boettcher, S. W.; Kempler, P. A. Electrolyte Engineering Stabilizes Thin-Film NixFe(1-x)OOH Catalysts during Reverse Current Conditions. *Meet. Abstr.* **2026**, *MA2026-01* (36), 1780. https://doi.org/10.1149/MA2026-01361780mtgabs.
(84) Kuai, C.; Zhang, Y.; Wu, D.; Sokaras, D.; Et., A. Fully Oxidized Ni–Fe Layered Double Hydroxide with 100% Exposed Active Sites for Catalyzing Oxygen Evolution Reaction. *ACS Catalysis* **2019**. https://doi.org/10.1021/acscatal.9b01935.
(85) Kuai, C.; Xu, Z.; Xi, C.; Hu, A.; Et., A. Phase Segregation Reversibility in Mixed-Metal Hydroxide Water Oxidation Catalysts. *Nature Catalysis* **2020**. https://doi.org/10.1038/s41929-020-0496-z.
(86) Todoroki, N.; Wadayama, T. Dissolution of Constituent Elements from Various Austenitic Stainless Steel Oxygen Evolution Electrodes under Potential Cycle Loadings. *International Journal of Hydrogen Energy* **2022**, *47* (77), 32753–32762. https://doi.org/10.1016/j.ijhydene.2022.07.175.
(87) Huang, X.; Zhang, W.; Xiao, L.; Han, C.; Liu, Y.; Zhang, J.; Tan, H.; Yin, P.; Zhang, R.; Dong, C.; Liu, H.; Du, X.; Yang, J. Electron Modulation in Cr-Doped NiFeOOH Enhances Oxygen Evolution Reaction Activity and Stabilizes Cr Dopant. *Trans. Tianjin Univ.* **2025**, *31* (3), 292–305. https://doi.org/10.1007/s12209-025-00434-4.
(88) Vendrame, D.; Boudjelida, S.; Negro, E.; Dolcet, P.; Di Noto, V.; Gross, S. Boosting the OER Performance of NiFe2O4 through Cr and Mn Doping via Hydrothermal Synthesis. *Front. Chem.* **2026**, *14*. https://doi.org/10.3389/fchem.2026.1778233.
(89) Nikolaidis, P.; Poullikkas, A. A Comparative Overview of Hydrogen Production Processes. *Renewable and Sustainable Energy Reviews* **2017**, *67*, 597–611. https://doi.org/10.1016/j.rser.2016.09.044.
(90) Abdel Haleem, A.; Nagasawa, K.; Kuroda, Y.; Nishiki, Y.; Zaenal, A.; Mitsushima, S. A New Accelerated Durability Test Protocol for Water Oxidation Electrocatalysts of Renewable Energy Powered Alkaline Water Electrolyzers. *Electrochemistry* **2021**, *89* (2), 186–191. https://doi.org/10.5796/electrochemistry.20-00156.
(91) Kuroda, Y.; Nishimoto, T.; Mitsushima, S. Self-Repairing Hybrid Nanosheet Anode Catalysts for Alkaline Water Electrolysis Connected with Fluctuating Renewable Energy. *Electrochimica Acta* **2019**, *323*, 134812. https://doi.org/10.1016/j.electacta.2019.134812.
(92) Gohlke, C.; Gallenberger, J.; Niederprüm, N.; Ingendae, H.; Kautz, J.; Hofmann, J. P.; Mechler, A. K. Boosting the Oxygen Evolution Reaction Performance of Ni-Fe-Electrodes by Tailored Conditioning. *ChemElectroChem* **2024**, *11* (18), e202400318. https://doi.org/10.1002/celc.202400318.